INAUGURAL - DISSERTATION

zur
Erlangung der Doktorwürde
der
Naturwissenschaftlich-Mathematischen Gesamtfakultät
der
Ruprecht-Karls-Universität
Heidelberg

vorgelegt von

Diplom-Physiker Florian Lamprecht

aus Hamburg

Tag der mündlichen Prüfung: .....

Kinetic design of the JAK-STAT1 pathway
and
MYCN impact on cell cycle decisions in neuroblastoma

Gutachter: Prof. Dr. Thomas Höfer
Priv. Doz. Dr. Karsten Rippe

Contents

Zusammenfassung

In der vorliegenden Arbeit werden mathematische Modelle angewendet, um Erkenntnisse über die Aktivierung des JAK/STAT1 Signalweges und über die Regulation von Zellzyklusentscheidungen im Neuroblastom zu gewinnen.

Die Familie der STAT Transkriptionsfaktoren spielt eine wichtige Rolle in der antiviralen Antwort der Zelle. In mehreren Tumoren findet man eine Dysregulation des JAK/STAT1 Signalübertragungsweges. Um die Funktionsweise und die Architektur dieses Signalweges weitreichender zu verstehen, wird ein auf Ratengleichungen basierendes, mathematisches Modell aufgestellt und an experimentelle Daten angepasst. Die Simulationen zeigen, dass die Aktivierung des Signalweges zeitlich eng an den Rezeptorstimulus gekoppelt ist und durch eine Kombination von schnellem intrazellulären Transport und kurzen Aufenthaltszeiten der STAT1 Moleküle im Nukleus aufrechterhalten wird. Die Affinität der STAT1-Dimerisierung hat einen signifikanten Einfluss auf die Effizienz und die Antwortcharakteristik des Signalweges. Dies deutet darauf hin, dass die Protein Wechselwirkungen im Laufe der Evolution stets so eingeschränkt waren, dass die Funktionalität des Signalweges sichergestellt war. Ferner wird gezeigt, dass die Aktivierung des Signalweges robust unter Änderung des nuklearen Exports von STAT1 ist. Die spezifische Architektur des JAK/STAT1 Signalweges unterdrückt kleine Stimuli und erlaubt sowohl effiziente Aktivierung, als auch ein schnelles Abschalten des Signalweges.

Das Neuroblastom ist der häufigste extrakranielle, solide Tumor im Kindesalter. Der Krankheitsverlauf reicht von spontaner Tumorrückbildung bis hin zur Entwicklung von aggressiven, therapieresistenten Tumoren. Eine Amplifikation des *MYCN* Onkogen ist mit einer schlechten klinischen Prognose assoziiert und bewirkt sowohl starke Proliferation, als auch verminderte Reaktion auf DNS-Schaden in Neuroblastomzellen. Mittels mathematischer Modelle der regulatorischen Netzwerke von p53-MDM2 und E2F1-pRB wird die Wirkungsweise von MYCN auf die Zellzyklusentscheidungen untersucht. Aufgrund der Vernetzung des p53-MDM2 Modules zeigt der p53-MDM2 Gleichgewichtszustand ein universelles Verhalten, welches mehrere qualitativ unterschiedliche Kinetiken beschreiben kann. Es zeigt sich, dass es plausibel ist, dass alleine die MYCN-Deregulation für den gestörten G1-S Übergang verantwortlich ist. Sowohl in Simulationen, als auch im Experiment, kann das Bifurkationsdiagramm des G1-S Überganges genutzt werden, um Eigenschaften dieses Überganges abzulesen. In Zellen mit erhöhten MYCN und CDK4 Konzentrationen wird eine Verschiebung des G1-S Überganges zu niedrigen Stimuli beobachtet und das Modell verbleibt auch nach DNS-Schaden in einem aktivierten, proliferativen Zustand. Weiterhin wird gezeigt, dass mittels des Konzeptes von Steady-Age-Verteilungen FACS-Daten von Zellzyklusverteilungen in Neuroblastomzellen analysiert werden können. Diese Analyse ergibt, dass die Überexpression von *MYCN* in SH-EP Zellen eine Verkürzung der G1-Phase bewirkt. Das vorgestellte Konzept kann in Zukunft als Standardmethode der Auswertung solcher Daten dienen.

Summary

We utilized the framework of mathematical modeling to gain insights into two distinct biological systems, the JAK/STAT1 signal transduction pathway and the regulation of cell cycle decisions in neuroblastoma.

The family of JAK/STAT signaling pathways plays a key role in immunity. In several tumors dysregulation of the JAK/STAT1 pathways is observed. To investigate the functionality of this signal transduction pathway and eventually understand basic building principles, we establish a databased mathematical model of the JAK/STAT1 pathway by means of kinetic rate equations. We showed that pathway activation is coupled tightly to the receptor stimulus at the cost of signal strength. The nuclear signal is sustained by a combination of fast translocation rates and short nuclear residence times of activated STAT1 protein molecules. Model simulations reveal that STAT1 dimerization kinetics have a strong impact on both efficiency of signaling and response kinetics, implying that protein-protein interactions are evolutionary constrained to ensure network functionality. Measurements of STAT1 transport mutants validated the mathematical model and showed that STAT1 activation is robust against enhanced nuclear export. By the kinetic design of the pathway input noise is suppressed, the pathway can be efficiently activated and rapid relaxation after stimulus withdrawal is ensured.

Neuroblastoma is the most common extracranial solid tumor of infants and children. Its course of illness varies between spontaneous regression and malignant, aggressive progression. Amplification of the *MYCN* oncogene is predictive for poor clinical outcome in neuroblastoma. *MYCN*-amplified cells proliferate strongly and exhibit impaired cell cycle arrest. To rationalize the impact of MYCN on the regulatory networks, governing cell cycle progression and DNA damage response, we established mathematical models of the regulatory modules, p53-MDM2 and E2F1-pRB, by means of mass action kinetics. The inherent regulation in the p53-MDM2 module leads to an universal form of the p53-MDM2 steady state and can account for several qualitatively different behaviors upon p53 activation. We show that it is plausible that the weak G1 arrest in the *MYCN*-overexpressing cells is due to a MYCN-induced protein level imbalance in the p53-MDM2 module. Furthermore we argue that the bifurcation diagram of the G1-S transition model can both theoretically as well as experimentally be used as an output to analyze the restriction point behavior in neuroblastoma. It shows that for cells with relatively high MYCN level and an enhanced CDK4 signal the bistable region is shifted to low stimuli and the model stays in an activated state even under DNA damage. A mathematical framework is provided, which potentially can serve as a future standard method to extract underlying cell cycle parameters from combined FACS-measured cell cycle phase distributions and cell growth rate measurements. Analysis of measurements in the SH-EP neuroblastoma cell line showed that conditionally upregulated MYCN mainly changes the length of the G1 phase.

1 Materials and Methods

In this chapter the used algorithms are introduced and the experimental procedures are given. For numerical calculations mostly the software MathWorks MATLAB and Mathematica from Wolfram Research were used.

1.1 Fitting with Levenberg Marquard algorithm and simulated annealing

Dependent on the problem appropriate fitting algorithms were implemented to determine the underlying parameter sets. The mathematical model of the JAK/STAT1 pathway was quite well defined by measurements of relevant parameters. There were just six remaining parameters to be determined by fitting and already the local Levenberg Marquard algorithm [74, 86] gave good results. To verify the global minimum and to get confidence intervals for the parameters a Markov chain Monte Carlo method is used additionally (see next section). The relevant parameters for the mathematical models in the second part of the work are mostly unknown. Thus, the amount of data is quite low for the number of free parameters. So that the fitting was carried out by either manual qualitative fitting or by a simulated annealing algorithm [62].

1.1.1 Markov chain Monte Carlo

To calculate confidence intervals we used a Markov chain Monte Carlo method [93] implementing the Metropolis-Hastings algorithm [92, 52, 109] with a normal proposal distribution. It is tuned such, that the acceptance rate for every step is around one third which is empirical a good value to get a fast convergence. We let the chain run for at least $2 \cdot 10^6$ steps to account for the burn-in time. The actual chain consisted of $4.5 \cdot 10^6$ steps from which for the statistics every tenth point was taken to eliminate correlations. The convergence could be seen by eye and at the fact that the mean χ^2 of the points in the chain did not get smaller.

1.2 Gillespie simulation

A stochastic simulation of the model was performed by implementing the Gillespie algorithm [43] in C++ to test for stochastic effects and keep track of the times the molecules took for various processes. For example we were interested in how long it takes until an imported phospho-STAT1 molecule is dephophorylated in the nucleus. For every state s in the nucleus we defined at every time step t_i in the algorithm a matrix M_i^s with a row for every molecule in the state. For bookkeeping we needed one entry for the time at which the molecule was imported into the nucleus and one entry for the time it entered the state. At every transition leaving the state s a molecule was drawn randomly from M_i^s and the time in the state could be read out. From this we got statistics over the times spent in the states. For example we could deduce for every STAT1 getting dephosphorylated in the nucleus the time spent in the nucleus before. By also keeping track of the history of every molecule it was possible to access the time a STAT1 protein took from time point of import as phospho dimer to the time getting back into the cytoplasm. As time step for the Gillespie algorithm 0.1 minute was taken.

1.3 Bifurcation analysis

The bifurcation analysis was carried out by using AUTO-07p a fortran based software to numerically calculate bifurcation diagrams and continuations for ordinary differential equation systems. To plot the results, the visualization tool XPPaut was used. After export from XPPaut and import into mathematica for the noncomplex model of E2F1-pRB interaction a comparison to the semi-analytical solution was possible.

1.4 Experimental setup JAK/STAT1 pathway

As far as not stated otherwise all experiments investigating the JAK/STAT1 pathway were performed by our collaborator Thomas Meyer, *Universität Göttingen*.

1.4.1 Cell culture

HeLa and U3A cells were cultured at 37 °C in a humidified 5% CO2 atmosphere in D-MEM supplemented with 10% fetal calf serum (Gibco), 1% penicillin/streptavidin and 1% amphotericin. Cells grown on poly-L-lysine-coated glass coverslips were transiently transfected with Lipofectamine plus (Gibco) and twenty-four hours later

stimulated with 5 ng/ml human IFN-γ (Biomol). In some experiments cells were additionally incubated with 500 nM staurosporine (Sigma), 10 ng/ml leptomycin B (LMB, Sigma), or a combination of 0.8 mM sodium vanadate and 0.2 mM H_2O_2.

1.4.2 Generating the wNLS, sNLS and NES cell line

A STAT1 import mutant with substitutions of two lysines in position 410 and 413 to glutamic acids was used as a exclusively cytoplasmic STAT1 mutant, ΔNLS [94]. The STAT1-NES mutant was cloned by ligating a PCR fragment amplified from pGST-STAT1367-427-GFP [94] into the BamHI-NotI restriction sites of pSTAT1-GFP. The resulting plasmid pSTAT1-NES-GFP coded for a transferable NES activity containing amino acids 367-427 of STAT1 situated between the cDNAs for wild-type STAT1 and GFP. Upon stimulation with IFN-γ, the total amount of nuclear STAT1-NES remained much below the accumulation achieved in the wild-type. This is not due to a phosphorylation defect, as STAT1-NES becomes strongly tyrosine-phosphorylated. Nuclear accumulation upon IFN-γ stimulation was restored in the STAT1-NES mutant when nuclear export was blocked by the simultaneous addition of LMB. These findings showed that although phosphorylated STAT1-NES was imported into the nucleus, the presence of the heterotopic export signal prevented sufficient nuclear buildup. To demonstrate that the lack of nuclear accumulation of total STAT1-NES in the absence of LMB is due to rapid export of the mutant protein, we stimulated the cells with IFN-γ and at the same time blocked dephosphorylation by adding vanadate. Under this condition, phospho-STAT1-NES again did not accumulate in the nucleus whereas STAT1-WT did. The additional inhibition of nuclear export by LMB rescued the defective nuclear accumulation of STAT1-NES. Taken together, these data demonstrate that phospho-STAT1-NES enters the nucleus, but cannot be retained there due to its rapid export as a phosphoprotein. Plasmids coding for STAT1 import mutants (STAT1-wNLS, STAT1-sNLS and STAT1-LSN) were generated by phosphorylating annealed oligonucleotides in a T4 polynucleotide kinase reaction and subsequently cloning them into the BamHI site of pSTAT1-GFP, which is situated between the cDNAs for STAT1 and GFP. pSTAT1-wNLS coded for a mutated NLS derived from the large T antigen of SV40 virus (PKKKAKVE; mutation underlined) and pSTAT1-sNLS for a tandem arrangement of the wild-type SV40 NLS (PKKKRKVE), while in pSTAT1-LSN the sequence was permuted (PKEAKVKK). wNLS and sNLS were chosen by assaying the subcellular STAT1 distribution using fluorescence microscopy.

1.4.3 Fluorescence microscopy

For direct microscopical examination the cells were fixed in 3.7% paraformaldehyde in phosphate-buffered saline (PBS) and subsequently, the nuclei were stained with

5 mg/ml Hoechst 33258 (Sigma). Fluorescence microscopy was performed using a Zeiss Axioplan microscope (Zeiss) equipped with appropriated fluorescence filters.

1.4.4 Western blotting

Phospho-STAT1 was detected in cell lysates by means of immunoblotting using a polyclonal antibody specific for phospho-STAT1-Tyr701 (New England Biolabs) followed by incubation with a horseradish peroxidase-conjugated secondary antibody. After stripping off bound antibodies, the blots were reexposed to the polyclonal STAT1-specific antibody C-24 (Santa Cruz), as described in [94]. The intensities of the band signals were densitometrically measured using the enhanced chemiluminescence reaction and specific phosphorylation levels were calculated by determining the ratio of phospho-STAT1 to STAT1.

1.4.5 Reverse transcriptase-PCR

The transcriptional activities were assessed by means of reverse transcriptase (rt)-PCR. Similar cell numbers of transfected U3A cells expressing either wild-type or mutant STAT1 were stimulated with IFN-γ for the indicated times. Gene-specific primers for six endogenous STAT1 target genes as well as for stat1 and gapdh were used to amplify the generated cDNAs, as has been described [94]. The relative expression of a transcript was normalized to the expression of gapdh as determined for each sample.

1.5 Experimental setup Neuroblastoma

The experiments with the neuroblastoma cells were either performed by the author, the master student Elena Cristiano or members of the Frank Westermann lab (department tumor genetics, *DKFZ Heidelberg*).

1.5.1 Cell culture

Cell lines were cultivated in D-MEM supplemented with 100 U/ml Penicillin/Streptomycin, 0,2% Amphotericin B, and 10% FCS at 37 °C, in 5% CO_2 atmosphere in a humidified cell culture incubator. Cell culture medium was substituted every 3-4 days, and cells were split at ratio 1:5 when they reached subconfluent density. Adherent cells were removed from the substratum by versenization. Visual observation of cell morphology was conducted under the Zeiss Axiovert microscope, equipped

with phase contrast and bright field optics. The SH-EP T21N cell line conditionally expressing a MYCN transgene under the control of a tetracycline-repressible element [80] and the IMR5-75 C2 cell line [141] conditionally expressing MYCN siRNA also under the control of tetracycline [157] were incubated at least 24 hours before treatment either with tetracyclin (1 mg/ml) solved in ethanol or with just ethanol to induce or knock down MYCN. Treatment to induce DNA damage was done with doxorubicin 0.1 μg/ml. Treatment to target MDM2 and CDK4 was done with Nutlin-3 and/or CDK4 inhibitors [15] at concentrations of 0.1, 1 or 10 μM in culture medium.

1.5.2 Colony formation in soft agar

Cells were suspended in 3 ml of RPMI-1640 medium 10% PCS containing 0.35% agar and layered above a 3-ml base layer of 0.5% agar in the same medium in 5-cm tissue culture dishes. Cells were fed once a week with 0.5% agar in medium, and visible colonies (>0.2 mm) were counted after incubation for several days.

1.5.3 Quantitaive real time RT-PCR

All quantitaive real time RT-PCRs (qRT-PCR) were performed on an ABI PRISM 7700 Sequence Detection System (Applied Biosystems) using the standard curve method for quantification (user bulletin no. 2, ABI PRISM 7700 SDS). To determine mRNA expression of genes, SYBRgreen based qRT-PCR was performed using cDNA as template. To prevent amplification from contaminating genomic DNA, primer sequences were selected allowing intron spanning amplification. PCR reactions were run as duplicates for each sample and as triplicates for determination of standard curves. For normalization, the expression level of the target gene was divided by the geometric mean of expression levels of the house keeping genes [56].

1.5.4 Western blot

For preparation of total protein samples, cells were harvested by versenization (for analysis of cells induced with cytotoxic agent, both floating and adherent cells were collected), washed with ice cold PBS buffer supplemented with 1mM PMSF, and resuspended in ice-cold protein extraction buffer. To digest high molecular weight genomic DNA, samples were treated with benzonase for 30 minutes at 37 °C. Insoluble proteins and membranes were removed from the samples by centrifugation at 8000x for 5 minutes. Total amount of protein in the resulting samples was determined by the method of Bradford [9] using protein assay kit. Prior to loading onto a gel, the samples were mixed with 2x Laemmli sample buffer and boiled for

5 minutes. Routine SDS-PAGE was peformed in reducing conditions (samples were treated with 2-ME or DTT) on 10-20% gradient mini gels in Tris-glycine buffer system (by Laemmli). Gradient gels were prepared with the Multi Cast Unit and the Gradient former (BioRad), according to the suppliers' protocol. To prepare eight separating gels, 25 ml of the light (10% PAA) and heavy (20% PAA) gel solutions were made. The light gel solution was filled in the mixing chamber of the gradient former, and the heavy gel solution was poured into the reservoir chamber. First, the bottom valve of the multi cast chamber was opened, allowing the 10% PAA to fill the glass sandwiches to approximately 5 mm heights. Then the gradient former interconnecting valve was opened, allowing the heavy gel solution to flow into the mixing chamber. Resulting discontinues PAA gradient was filled in the glass sandwiches under the layer of 10% PAA. Resulting 10-20% PAA gradient gels were overlaid with H_2O-saturated isobutyl alcohol and allowed to polymerize for 2 hours. Approximately 20-40 μg of total protein in 1x Laemmli sample buffer were loaded into each slot. For monitoring of the separation and determination of protein size, the Prestained BenchMark and the biotinylated protein ladders were used. Protein separation was performed at 45 mA per gel with constant current for approximately 1 hour. Proteins, separated by SDS-PAGE, were electro transferred onto retentive membranes using the tank method. Proteins were transferred onto 0.2 μm nitrocellulose membranes. Electro transfer was performed at 4 °C in 1x transfer buffer for 3 hours at 150V/450 mA or overnight at lower current. After the transfer, the efficiency of the transfer and equal loading were verified, if necessary, by reversible staining of the membranes with Ponceau S. The membranes were incubated with 1x Ponceau S for 5 minutes at RT with slight agitation, then rinsed several times with 5% acetic acid, until desirable contrast of stained protein bands was achieved. Prior to immunodetection, the stain was removed by several washings in H_2O. In standard immunodetection of proteins blotted onto nitrocellulose membranes, the membranes were first blocked for 1 hour with unspecific proteins (5% fat-free milk powder) to prevent antibody binding to the membrane. The primary antibody was added in a concentration of 1-10 μg/ml in an aqueous solution containing 5% fat-free milk powder and incubation was performed at 4 °C over night. After rinsing with PBS (3 times for 5 minutes), the membranes were incubated for 30 minutes with a secondary HRP-conjugated antibody, diluted 1:5000 in 5% fat free milk powder solution. After final washing with PBS (3 times for 5 minutes), protein bands were detected by chemiluminescence, using the BM Chemiluminescence kit.

1.5.5 Generating the SH-EP T21N p21mCherrry cells

We used a plasmid containing the p21 promoter fused to the fluorophore mCherry, a nuclear localization signal (NLS) and a PEST sequence to shorten the mCherry half live (received from Alexander Löwer, *The Berlin Institute for Medical Systems Biology*, plasmid map see appendix A.5) to generate a clone of the conditionally *MYCN* expressing SH-EP T21N cell line for single cell live microscopy. SH-EP

T21N cells were transfected at 30% confluency with 3.5 μg of DNA (Qiagen effectene transfection kit). The polyclonal positive population was selected with 7.5 μg/ml blasticidin and seeded in 96 well plates at the concentration of 0.5 cells, 1 cell and 2 cells per well. After one week, the wells containing colonies from single clones were selected and the cells were expanded. The clones expressing the mCherry construct were preselected by eye (inverted fluorescent microscope Olympus CKX41). The second round of selection was based on: growth rate and responsiveness to DNA damage. Only the clones that showed the same growth rate as SH-EP T21N cells and showed inducible fluorescence upon DNA damage (performed with 0.1 μg/ml of doxorubicin) were selected.

1.5.6 Fluorescent single cell live microscopy

SH-EP T21N p21mCherry cells were grown in μ-ibidi plates (35 mm) up to $\sim$ 20% confluency. The expression of mCherry at the single cell level was measured with a Nikon BioStation IM at constant temperature of 37 °C with 5% of CO2. Cells were monitored for 72 hours and the images were analyzed manually with ImageJ in combination with an automated tracking algorithm [50]. MATLAB was used to calculate statistics of the division time distribution and for visualization.

1.5.7 FACS

Cells were collected for cell cycle analysis in 2.1% citric acid/0.5% Tween 20 and stained with 50 μg/ml DAPI dissolved in phosphate buffer (0.4 M Na_2HPO_4, pH 8.0). Approximately 50,000-100,000 cells were analyzed per run on a Galaxy Pro Flow Cytometer (Partec) using the Multicycle software (Phoenix Flow Systems). To evaluate apoptosis, cells were labeled with Nicoletti stain [105], and approximately 5,000-10,000 cells were analyzed on a FACS Calibur (Becton Dickinson) using the Cell Quest software (Becton Dickinson). Measurements were acquired in Fl-2 in logarithmic mode. The number of apoptotic cells was calculated by setting the gate to over the first three decades (100 to 103).

Part I

Mathematical Modeling of the JAK/STAT1 Pathway

2 Introduction JAK-STAT1 pathway

For nearly every cell it is of utmost importance to react appropriately to their environment ranging from environmental factors like nutrition levels to intercellular communication via cytokines. Often the appropriate reaction of the cell includes activation of genes. This function is carried out by several signal transduction pathways that transport the information into the nucleus.

2.1 The JAK/STAT pathway

The JAK/STAT pathway is a highly conserved signaling pathway mediated by cytosolic tyrosine kinases, the Janus kinases (JAK), and signal transducers and activators of transcription (STAT) proteins. The Interferon/STAT pathway is a major player in antiviral defense; moreover aberration in STAT pathways have been implicated in many types of cancer [13, 70, 131, 14]. The STAT family consist of seven members with heterogeneous functions [24, 75, 107] (STAT1, STAT2, STAT3, STAT4, STAT5A, STAT5B, STAT6). Despite many similarities within the STAT family members, STAT1 is best characterized with respect to the molecular events triggered by the activation of the pathway and can serve as a model system for canonical STAT signal transduction.

2.2 Activation of the STAT1 pathway

In an unstimulated cell STAT1 is both present in the cytoplasm and can enter the nucleus by shuttling through nuclear pores and CRM1-mediated energy dependent nuclear export [84, 88, 150]. The activation of the STAT1 pathway from receptor binding of the ligand to activation of transcription comprises many steps. Upon binding of IFN-γ to its associated receptor the receptor chains dimerize leading to autophosphorylation of the receptor chain-bound JAKs. This encompasses the JAK-mediated tyrosine phosphorylation of STAT1 binding sites at the receptor chain enabling the binding of the src homology 2 domain (SH2) of the STAT1 protein [126]. The bound STAT1 is targeted by another JAK-mediated tyrosine phosphorylation at residue Thr 701. The phosphorylated STAT1 (phospho-STAT1) can (after dissociation from the receptor chain) bind to another phospho-STAT1 protein and form a

homodimer via the cross interaction of the phosphorylated Tyr701 from one STAT1 with the SH2 domain of the other STAT1 (SH2 dimer). There is a second conformational different STAT1 homodimer which is bound by N-terminal interactions (N-terminal dimer). The formation of the N-terminal dimer seems to be independent of STAT1 phosphorylation. Interestingly, the phospho-STAT1 is not able to shuttle via the nuclear pore complex or CRM1-mediated between cytoplasm and nucleus [95]. However the SH2-dimer are imported into the nucleus in association with importin-α5 and importin-β [124, 35, 102]. In the nucleus the SH2-dimers can bind to cognate regulatory DNA sequences, IFN-gamma-activated sites (GAS) [28]) and unspecifically to DNA [120, 126, 163] and activate transcription. The DNA binding is enhanced by interaction between DNA-bound STAT1 dimers. Both in the cytoplasm and in the nucleus phospho-STAT1 is targeted by yet unknown phosphatases [51, 140, 139, 97]. By binding to the SH2 domain, the Tyr 701 phosphorylation is saved from dephosphorylation.

2.3 STAT1 interactions

In addition to the activation of STAT1 by JAK there are several additional regulations modulating the activation of the STAT1 pathway. STAT1 protein is targeted by several further posttranslational modifications such as serine phosphorylation [27, 65, 148] and sumotylation [29, 143, 127, 168]. STAT1 not only forms homodimers but also heterodimerizes with STAT2, which activate different target genes as compared to STAT1 homodimers. Furthermore STAT1 is involved in NFκB signaling (having a proapoptotic effect) [66]. By stimulation of the JAK/STAT1 pathway also a negative feedback is activated. STAT1 mediates SOCS1 gene expression (member of suppressor of cytokine signaling proteins) [25, 46] which suppresses STAT1 activation. SOCS1 inhibits the catalytic activity of JAK by direct interaction and by targeting proteins (e.g. receptor and JAKs) for proteosomal degradation [33]. Further inhibitors of STAT1 activity have been identified including PIAS (protein inhibitor of activated STAT) and SLIM (STAT interacting LIM protein). Both PIAS1 and PIASy interact with activated STAT1 upon cytokine treatment. PIAS1 binds to tyrosine phosphorylated dimeric STAT1 and it has been proposed that it is suppressing the DNA-binding activity of STAT1 [77]. SLIM (STAT interacting LIM protein) was identified as a ubiquitin E3 ligase for STAT1 [137].

3 Mathematical model of the JAK/STAT1 pathway

In this chapter the mathematical model of the JAK-STAT1 pathway and the corresponding biochemical reactions involved in the model are introduced. The differential equations are given and the model parameters are estimated. Many of the relevant parameters were already directly or indirectly measured. The remaining six parameters were determined by fitting the model to a data set containing STAT1 phosphorylation kinetics and intracellular STAT1 distributions.

3.1 Network model and comprised reactions

We established a mathematical model of the JAK/STAT1 pathway accounting for the processes involved in the subcellular localization, the activation and deactivation of the STAT1 protein including receptor binding and DNA binding (figure 3.1). The total number of STAT1 molecules per cell were estimated from Western blot-measured pancellular STAT1 concentration $c_{\mathrm{tot}} = 40$ nM. An approximate cell diameter of 20 μm and assuming spherical shape of the cells yield $\sim 10^5$ STAT1 protein molecules per cell. Due to the high number of proteins, the reactions involved could be simulated deterministically. This was indeed shown by a comparison of the deterministic solution with the solution of a stochastic simulation (see section 4.2).

The processes depicted in figure 3.1 were formulated in terms of dynamical equation using mass action kinetics. The investigated processes were simulated by ordinary differential equations, assuming the intracellular diffusion to be much faster than the timescale of the reactions [76]. The resulting 19 kinetic rate equations are given in the appendix (section A.1).

3.1.1 Compartment volumes and STAT1 nucleo-cytoplasmic shuttling

In an unstimulated cell, both the nucleus and the cytoplasm are accessible for the latent STAT1 through the nuclear pore. Additionally STAT1 is actively transported into the cytoplasm by the CRM1 protein [36, 37]. Differences in compartment volumes play an important role modeling transport processes. Clearly the resulting

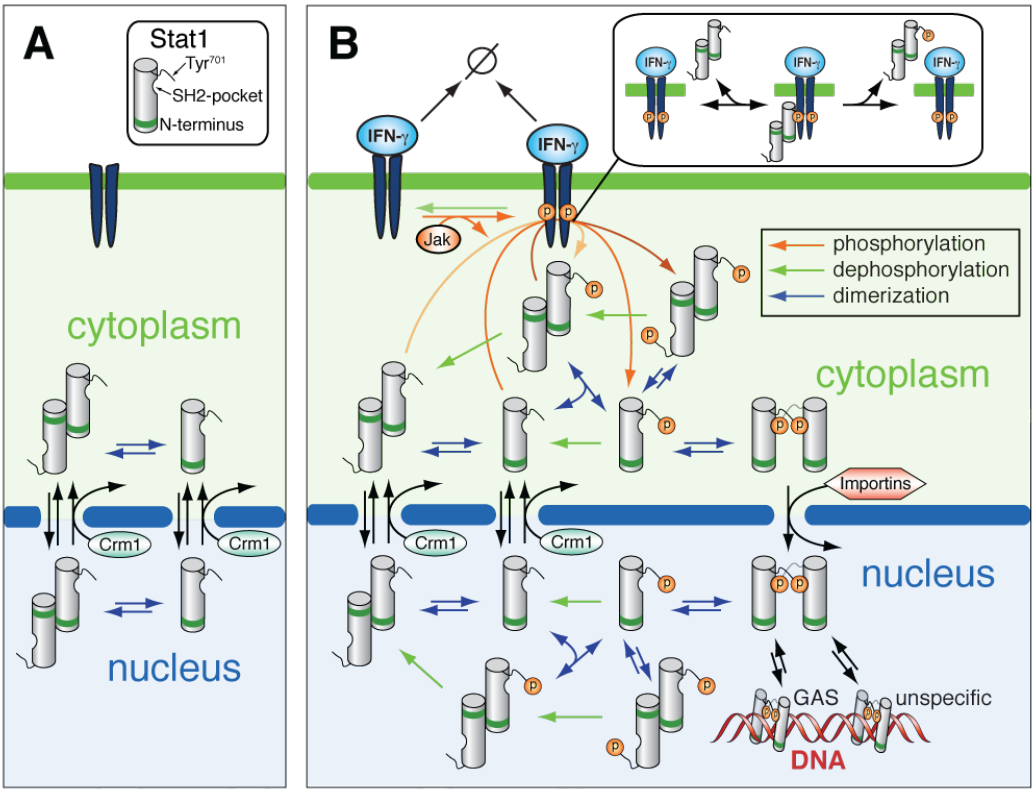

Figure 3.1: Pathway design of the JAK/STAT1 pathway. (**A**) Network model for STAT1 translocation in unstimulated cells. Latent STAT1 can shuttle in between nucleus and cytoplasm both as monomer and N-terminal dimer. The N-terminal dimer is formed with the two STAT1 in an antiparallel alignment. CRM1 denotes energy-dependent nuclear export via CRM1. (**B**) Network model for interferon-γ (IFN-γ) stimulated STAT1 signal transduction depicting nuclear import and export of latent STAT1, activation of IFN-γ receptor/JAK complexes, STAT1 binding to activated IFN-γ receptor/JAK complexes, tyrosine phosphorylation (red arrows), dimerization of STAT1 via phosphotyrosine/SH2 interactions (STAT1 aligns parallel in the SH2 dimer) and N-terminal interactions (blue arrows), nuclear import of phospho-STAT1 via importins, specific (GAS) and unspecific binding of phospho-STAT1 dimers to DNA and cytoplasmic and nuclear dephosphorylation (green arrows).

concentration change due to the flow of a particular protein entering or leaving a certain compartment, depends on the compartment volume. Consequently, the compartment volumes enter the rate equations for the transport processes. As the number of STAT1 molecules is assumed to be conserved on the relevant time scales it follows

$$
\begin{aligned}
V_{\text{nuc}}\, S_{\text{nuc}} + V_{\text{cyt}}\, S_{\text{yt}} &= N_{\text{tot}} = \text{const.} \\
\Rightarrow V_{\text{nuc}}\, \partial_t\, S_{\text{nuc}} + V_{\text{cyt}}\, \partial_t\, S_{\text{cyt}} &= 0 \\
\Leftrightarrow \partial_t\, S_{\text{nuc}} - \rho\, \partial_t\, S_{\text{cyt}} &= 0 \text{ with } \rho = \frac{V_{\text{cyt}}}{V_{\text{nuc}}},
\end{aligned}
$$

where V_{nuc} and V_{cyt} are the volume of the compartments (nucleus and cytoplasm) and S_{nuc}, S_{cyt} are the corresponding STAT1 concentrations. The differential equations for the nucleo-cytoplasmic transport with rates k_{12} and k_{13} then reads

$$
\begin{aligned}
\partial_t\, S_{\text{nuc}} &= \rho\,(k_{13} S_{\text{cyt}} - k_{12} S_{\text{nuc}}) \\
\partial_t\, S_{\text{cyt}} &= -k_{13} S_{\text{cyt}} + k_{12} S_{\text{nuc}},
\end{aligned}
$$

where ρ enters, as the concentration is not a conserved quantity in the sense that $S_{\text{cyt}} + S_{\text{nuc}} \neq$ const. and the concentration flow is dependent on the reference volume. By analyzing z-stacks of microscopy images of U3A cells the ratio of cytoplasmic to nuclear volume ρ was estimated to $\rho = 3$. This is in line with recently published data [101]. Measuring the ratio X of STAT1 concentration in the compartments at steady state

$$
X = \frac{S_{\text{nuc}}}{S_{\text{cyt}}}
$$

and the half-time $t_{1/2}$ for nucleo-cytoplasmic shuttling

$$
t_{1/2} = \frac{\ln(2)}{\rho\, k_{12} + k_{13}}
$$

yields the transport rates and the concentrations in the respective compartments at steady state

$$
\begin{aligned}
S_{\text{cyt}} &= \frac{1+\rho}{(X+\rho)} c_{\text{tot}} & k_{12} &= \frac{\ln(2)}{t_{1/2}\,(X+\rho)} \\
S_{\text{nuc}} &= X S_{\text{cyt}} & k_{13} &= X k_{12},
\end{aligned} \tag{3.1}
$$

with c_{tot} the pancellular STAT1 concentration. We estimated the half-time from microinjection measurements , where fluorescent STAT1 was microinjected into the different cell compartments and the corresponding dynamics of redistribution could be monitored with the help of specific antibodies [83]. The time course of redistribution and its half-time could be estimated to $t_{1/2} \sim 0.4$ min (Thomas Meyer, private correspondence). Western blot measurements of fractionated resting cells showed a ratio of nuclear to cytoplasmic STAT1 of $X = 3/7$. Inserting this into equation 3.1 gives the rate for energy independent nuclear import $k_{13} = 0.2\ \text{min}^{-1}$ and the sum of the rate for energy independent nuclear export and the rate for CRM1 mediated nuclear export $k_{12} = k_{12\text{a}} + k_{12\text{b}} = 0.5\ \text{min}^{-1}$. The rates of tyrosine phosphorylation and dephosphorylation were assessed by means of Western blotting, demonstrating a maximal phospho-STAT1 fraction of 30-35% in both HeLa cells and STAT1-reconstituted U3A cells under standard stimulation with 5 ng/ml interferon-γ (IFN-γ) [156].

3.1.2 Receptor kinetics and STAT1 phosphorylation

The activation of the IFN-γ bound receptors by JAK mediated phosphorylation is incorporated in the model as one reversible reaction with rate constants k_1 and k_2, where the concentration of JAK is assumed to be constant. Also receptor deactivating processes like internalization are included by a receptor degradation reaction (rate constant k_3). We used an estimate for the total number of IFN-γ bound receptors (10^4 receptors) and fitted the rate constants (section 3.2). The JAK phosphorylated tyrosine residues at the receptor are binding sites for the STAT1 protein and we modeled the STAT1 phosphorylation at the receptor via reversible binding of STAT1 to the receptor and a one step, unidirectional phosphorylation reaction of the bound STAT1 which was also fitted (k_5). The binding rates of STAT1 to the activated IFN receptor/JAK complex (k_4, k_{-4}) have been measured by surface plasmon resonance [47]. However, to correctly reproduce the phosphorylation kinetics, we had to use a two-fold higher on-rate $k_4 = 1.6 \cdot 10^{-2}\ \text{min}^{-1}\ \text{nM}^{-1}$. This maybe due to experimental errors or STAT1 dimerization.

3.1.3 Dimerization

STAT1 forms two conformationally different homo dimers either via SH2 domain interaction or by N-terminal binding. Using sedimentation experiments with ultra speed centrifuges the affinity as well as the rates of dimer formation were measured *in vitro* [156]. The result for the dissociation constant of SH2 binding was the same as the result for the dissociation constant of N-terminal binding (both 50 nM). Unfortunately implementing the measured binding rates it was not possible to reproduce the observed kinetics. Due to the proposed network, dimerization is

a prerequisite for nuclear import and dissociation of the dimer is necessary before dephosphorylation in the nucleus. Thus, the dimerization dynamics are limiting the pathway activation and deactivation times. To fit the measured phosphorylation and dephosphorylation kinetics, we had to increase both dimerization rate constants k_6 and k_{14}; and dimer dissociation rate constants k_{-6} and k_{-14} by a factor of 20, leaving the dissociation constant fixed. This yielded a mean half-life for the dimers of approximately one minute. There are several possible explanation for this discrepancy. On one hand the rates were measured *in vitro* and might well differ from the *in vivo* rates. Furthermore, the range of the measured rates are at the border of the measuring range of the method which might result in an inaccuracy in the values. In addition it might indicate a different network topology (see section 4.6).

3.1.4 STAT1 dephosphorylation

The tyrosine phosphorylation of STAT1 at residue Tyr 701 is targeted by yet unknown phosphatases both in the nucleus and in the cytoplasm. The phosphorylation of the STAT1 in the SH2-dimer conformation seems to be stable and not prone to dephosphorylation [91] whereas the N-terminal dimer probably can be targeted [156]. The rate constants of the dephosphorylation in the cytoplasm (k_7) and in the nucleus (k_{11}) are not known and determined by the fitting procedure (section 3.2).

3.1.5 DNA binding

STAT1 binds DNA both specifically at gamma interferon activation sites (GAS) and unspecifically. The strength of specific binding to the GAS sites with rate constants k_9 and k_{-9} has been determined previously [151, 163]. Therefore the rate constants were set to $k_9 = 0.06\ \text{min}^{-1}\text{nM}^{-1}$ and $k_{-9} = 0.05\ \text{min}^{-1}$. The exact number of GAS sites is not known and we estimated it to be 3000 which is around 1/30 of the total amount of STAT1. However, an exact definition and estimate of the number of GAS sites is not available. The unspecific binding to DNA (rate constants k_{10} and k_{-10}) was estimated by FRAP measurements ([95] and [5]) to be very unstable $k_{10} = 2\ \text{min}^{-1}$ and $k_{-10} = 5\ \text{min}^{-1}$. Due to the high number of unspecific binding sites the concentration of unspecific binding sites is relatively independent of bound STAT1 and we included the concentration in the rate constant k_{10}. We did not account for the possibility of the STAT1 dimers to form tetramers [151, 156]. The tetramerization stabilizes binding of STAT1 to DNA and is included in the DNA binding parameters.

3.2 Fitting of the remaining parameters

There were no estimates for the following rates: receptor activation/ inactivation/ internalization, STAT1 phosphorylation at the receptor, STAT1 dephosphorylation in the cytoplasm and STAT1 dephosphorylation in the nucleus (k_1, k_2, k_3, k_5, k_7 and k_{11}). To determine these remaining parameters the model was fit using the Levenberg-Marquardt Algorithm (section 3.2) simultaneously to time course measurements of phosphorylation and dephosphorylation (figure 3.2); and intracellular distributions of STAT1 under resting and stimulated conditions (figure 3.3). The time courses were measured both in STAT wild-type (STAT-WT) cells and in cells expressing mutated STAT1 which is bound to the cytoplasm, STAT-ΔNLS, (see section 1.4).

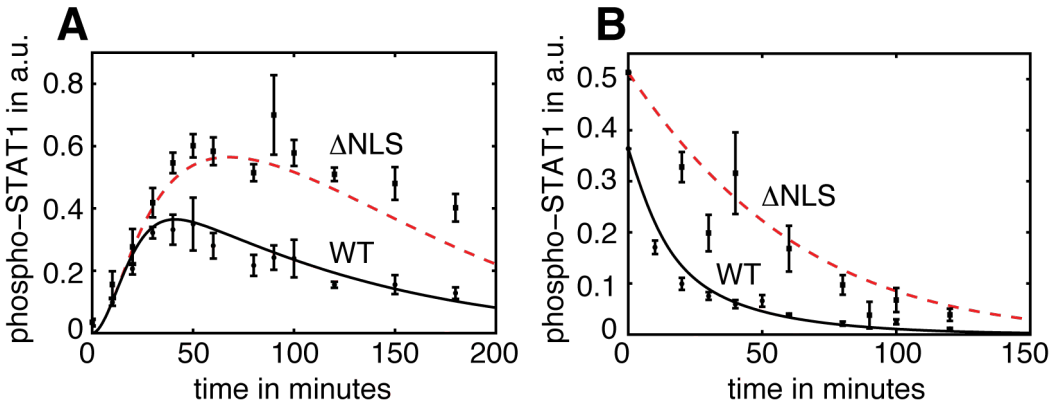

Figure 3.2: (**A**) The phosphorylation kinetics both for STAT1-WT and STAT1-ΔNLS after IFN-γ stimulation. (**B**) The dephosphorylation kinetic for STAT1-WT and STAT1-ΔNLS. After 45 minutes of IFN-γ stimulation cells were treated with a kinase inhibitor (at 0 minutes). Time course of protein levels was determined by Western blotting and used to determine the model parameters with a fitting algorithm (simulation with the best-fit values: black curve for STAT1-WT and red dashed curve for STAT-ΔNLS).

To quantify the uncertainty of the best-fit parameter values a Markov chain Monte Carlo (see section 1.1.1) simulation was performed. The chain converged well, which is indicated by the smooth distribution of all the fitted parameters (figure 3.4). The widths of the distributions are a measure of how well the respective parameters are determined by the data (under the assumption of the model). The calculation of 95% confidence intervals showed that all parameters except one have reasonable small uncertainties and are thus well determined by the data. The STAT1 phosphorylation at the receptor and its subsequent dissociation described by the rate k_5 can not be deduced from the given data. The best-fit value of k_5 is very high (29 min^{-1}) and the exact value does not play a role for the investigated activation because the time

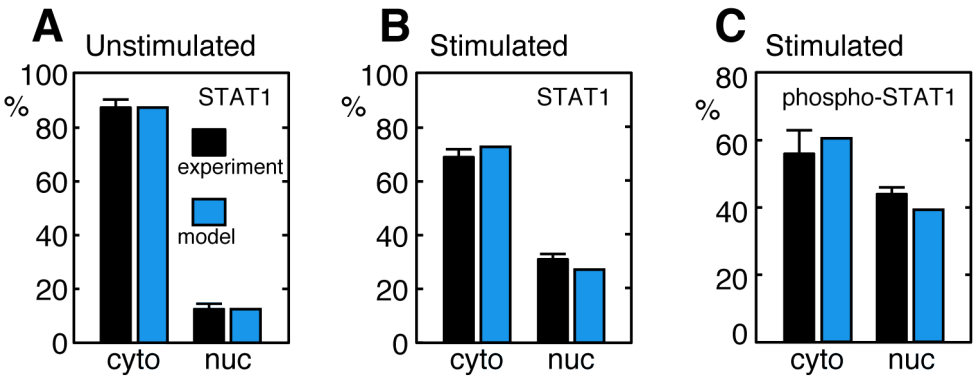

Figure 3.3: Intracellular distribution was measured (black bars) for (**A**) STAT1 in unstimulated cells, (**B**) STAT1 in stimulated cells (after 45 minutes of IFN-γ treatment) and (**C**) phospho-STAT1 in stimulated cells (after 45 min of IFN-γ treatment) and used in combination with the time course data (figure 3.2) to fit the model (best-fit result blue bars).

scale of the other involved processes is much lower. The result of the Markov chain Monte Carlo simulation shows that just a lower limit of 2 min^{-1} for the rate k_5 could be deduced from the data. The opposite is true for the deactivation rate of the IFN receptor/JAK complex k_3 which does not seem to play an important role in the activation and has to be sufficiently small. The values of the fitted parameters with confidence intervals are given in table 3.1.

Reaction	**Para.**	**Value [95% confidence]**
Activation IFN receptor/JAK complex	k_1	$0.056\ [0.049; 0.069]\ \text{min}^{-1}$
Deactivation IFN receptor/JAK complex	k_2	$1.9\ [0; 17] \cdot 10^{-3}\ \text{min}^{-1}$
Receptor degradation	k_3	$0.017\ [0.015; 0.018]\ \text{min}^{-1}$
STAT1 phosphorylation & dissociation	k_5	$29\ [> 2]\ \text{min}^{-1}$
Dephosphorylation in the cytoplasm	k_7	$0.023\ [0.021; 0.025]\ \text{min}^{-1}$
Dephosphorylation in the nucleus	k_{11}	$0.29\ [0.24; 0.37]\ \text{min}^{-1}$

Table 3.1: The values of the best-fit parameters determined by simultaneously fitting the model to the STAT1 distributions, STAT1 phosphorylation kinetics and STAT1 dephosphorylation kinetics. In brackets the 95% confidence intervals determined by the Markov chain Monte Carlo simulation are given.

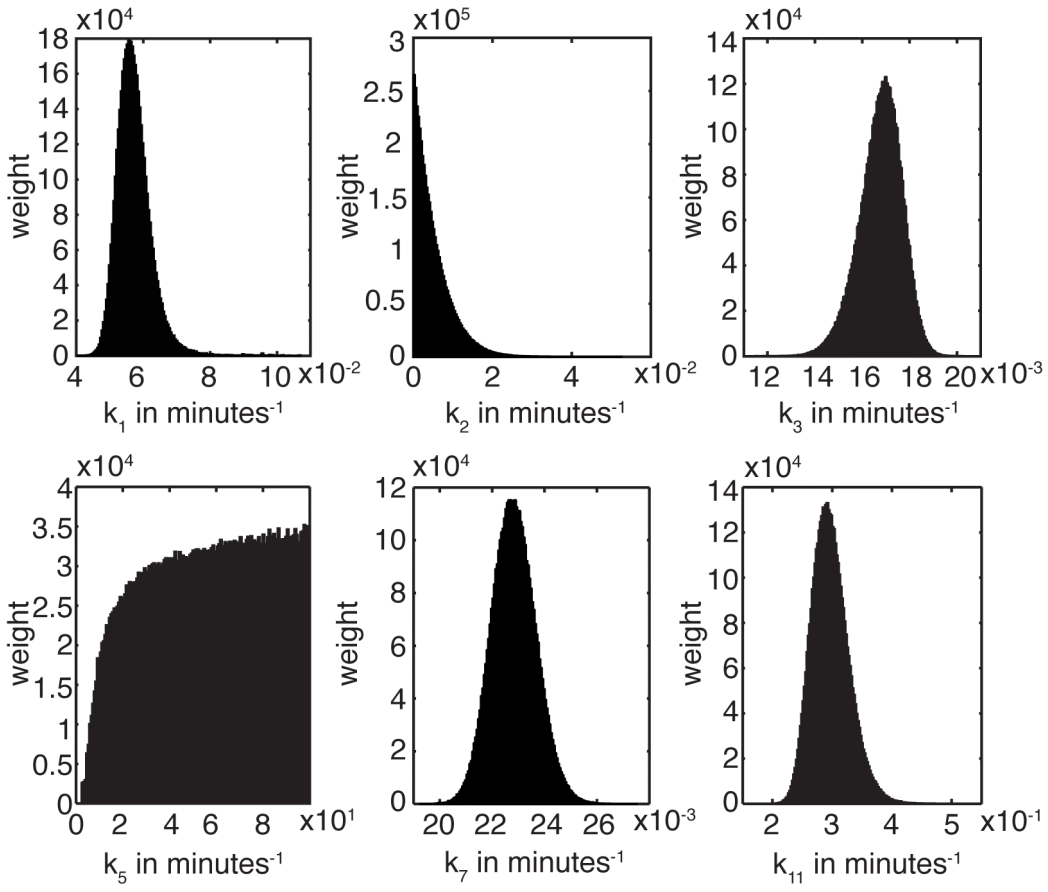

Figure 3.4: The resulting parameter value distributions from the Markov chain Monte Carlo simulation showed that the chain had converged. For the parameter k_5 just a lower limit could be determined from the data. To fit the data the rate k_2 has to be sufficiently small, indicating that the dephosphorylation of the receptor tyrosine is weak. All other parameter value distributions show reasonable small widths.

4 Design of the JAK/STAT1 pathway

In this chapter the mathematical model of the JAK/STAT1 pathway is validated by further measurements and used to extract properties of the pathway not accessible by experimental techniques.

4.1 Activation is controlled by a futile dephosphorylation cycle

For the activation of STAT1 dependent genes the SH2 dimers of phosphorylated STAT1 have to be transported into the nucleus. Interestingly, even under stimulated conditions the majority of STAT1 molecules are found in the cytoplasm. However, the concentration of phospho-STAT1 in the nucleus which determines the transcriptional response is much higher than in the cytoplasm due to the smaller nuclear volume (figure 4.1 A).

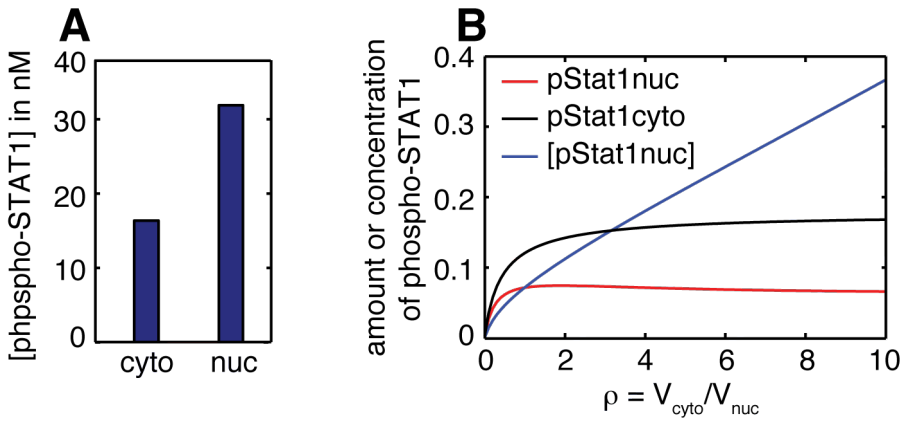

Figure 4.1: (**A**) The nuclear concentration of the phospho-STAT1 after 45 minutes of IFN-γ stimulation is much higher than the cytoplasmic phospho-STAT1 concentration due to the concentrating effect of the small nuclear volume. (**B**) For a decreasing nucleus size under constant total STAT1 concentration the concentration of phospho-STAT1 increases linearly with ρ for sufficiently high ρ.

Keeping the high ratio of cytoplasmic volume to nuclear volume $\rho = V_{\text{cyt}}/V_{\text{nuc}} = 3$ in the investigated cells in mind, we used the mathematical model to analyze the influence of ρ on the pathway activation. Assuming a fixed total STAT1 concentration in the cell and applying a constant IFN-γ stimulus the phospho-STAT1 in steady state was calculated as function of ρ (figure 4.1 B). The total amount of nuclear phospho-STAT1 becomes nearly independent of ρ for $\rho > 0.8$ and the concentration of nuclear phospho-STAT1 increases linearly with ρ in this range. The smaller nucleus is concentrating the phospho-STAT1 and thereby increasing the transcriptional response. This renders the signal transduction more efficient. The phosphorylation and dephosphorylation of the STAT1 molecules combined with the nucleo-cytoplasmic shuttling introduces a cycling process. The STAT1 pathway activation consists of two signaling cycles. Phosphorylation and dephosphorylation in the cytoplasmic compartment form an apparently futile cycle. Whereas subsequent phosphorylation, nuclear import, DNA binding, nuclear dephosphorylation and export form the functional cycle of gene activation (figure 4.2). The entry of

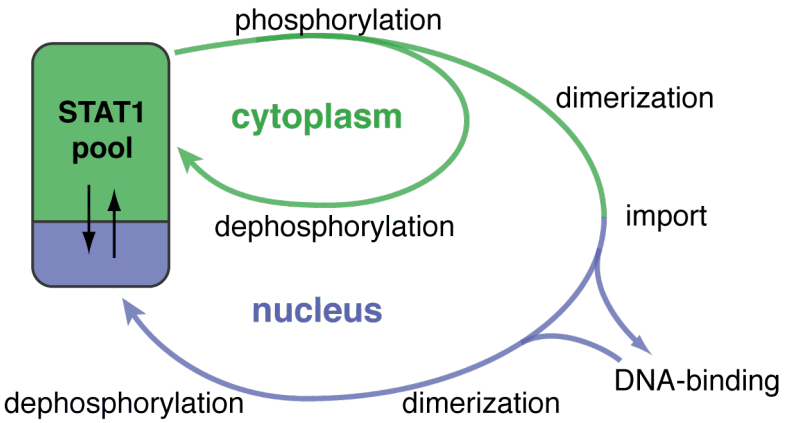

Figure 4.2: The topology of the STAT1 activation pathway is build of two cycles. One 'futile' cycle of STAT1 phosphorylation and subsequent cytoplasmic dephosphorylation and of a 'functional' cycle including STAT1 nuclear import and nuclear gene activation. The 'futile' cycle controls the STAT1 flow and can suppress low stimuli activation by the competition of cytoplasmic dephosphorylation with STAT1 homodimerization.

phospho-STAT1 into the functional cycle is dependent on the cytoplasmic-nuclear volume ratio. The cytoplasmic 'futile' cycle controls the signal amplitude for already moderate $\rho > 1.5$. The pathway activation is determined by the balance of cytoplasmic dephosphorylation ('futile' cycle) and dimerization with nuclear import. Consequently, because dephosphorylation competes with the dimerization for the phospho-STAT1 a signal is just transmitted into the nucleus if it is strong enough that the dimerization of the phospho-STAT1 overcomes the cytoplasmic dephosphorylation signal.

4.2 Pathway activation is sustained by fast phosphorylation and translocation rate constants and tightly follows the receptor signal

We define the response time $t_{\mathrm{a}}(s)$ to a stimulus s as the expectation time that the nuclear phospho-STAT1 bound to GAS sites $D_{\mathrm{S}}(s)$ reaches its maximum $D_{\mathrm{S}}^{\max}(s)$

$$t_{\mathrm{a}}(s) = \frac{1}{\mathcal{N}} \int (D_{\mathrm{S}}^{\max}(s) - D_{\mathrm{S}}(s,t)) \cdot t \; dt. \tag{4.1}$$

Accordingly the relaxation time t_{d} is defined as the expectation time to reach the resting state ($D_{\mathrm{S}} = 0$) after withdrawal of the stimulus

$$t_{\mathrm{d}}(s) = \frac{1}{\mathcal{N}} \int D_{\mathrm{S}}(s,t) \cdot t \; dt. \tag{4.2}$$

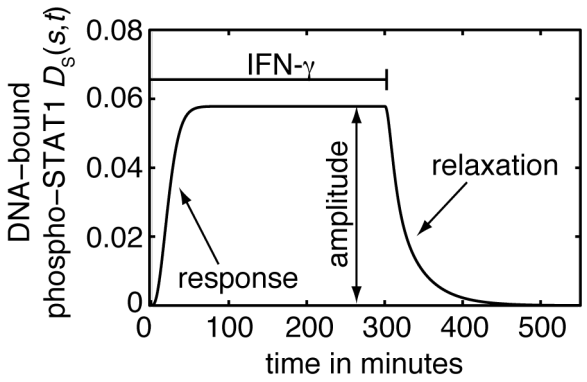

Figure 4.3: To quantify the pathway behavior we used the response time to a stimulus, the resulting amplitude and the relaxation time after stimulus withdrawal of phospho-STAT1 bound to GAS sites as characteristics.

For a simulation with a standard stimulus of 5 ng/ml IFN-γ (see section 1.4) the response time and the relaxation time are 7 minutes and 35 minutes respectively, showing that the signal in the nucleus is tightly coupled to the receptor activation. Especially the information of receptor activation is translated fast into a transcriptional signal indicated by the fast response time. To understand in more detail the mechanisms of signal progression and persistence, we were interested in the residence time of the STAT1 molecules in the different activated states. Especially we wanted

to know, how long the activated STAT1 stays in the nucleus before its dephosphorylation and subsequent reimport into the cytoplasm. Experimentally this is difficult to address, so we used the mathematical model and the given parameter set to calculate the residence times. One possibility is to deduce the mean residence time of phospho-STAT1 in the nucleus from the deterministic solution. Due to the nonlinear equations, this is not an exact estimation but serves as a good approximation (see appendix A.2). To get more exact residence times, we performed a stochastic simulation of the differential equation system using the Gillespie algorithm (see section 1.2) and the given parameters. One side result of this calculation is, that the system did not show any stochastic effects (figure 4.4), justifying the use of the deterministic solution of the ordinary differential equation system. Furthermore,

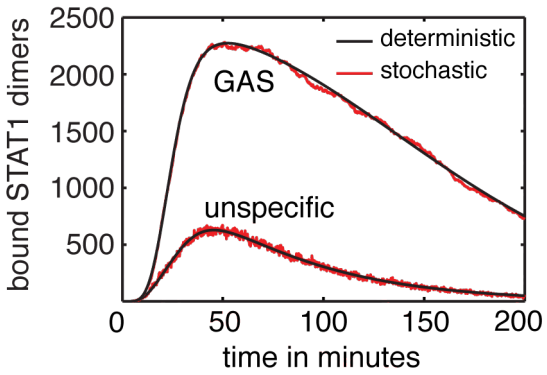

Figure 4.4: The resulting protein kinetics from the stochastic simulation of the pathway activation are very close to the result of the simulation of the deterministic solution even for the relatively low occupied states of DNA bound STAT1.

by bookkeeping of the single molecules throughout the simulation we can access the residence times of STAT1 molecules in the cellular compartments in the active (phosphorylated) and inactive (dephosphorylated) state and calculate the mean as well as its statistics. The mean time after phospho-STAT1 gets dephosphorylated in the nucleus after import was 12.3 min with 5 and 95 percentile 1.1 minutes and 14.7 minutes, respectively. The mean residence time of phospho-STAT1 in the nucleus until its reimport into the cytoplasm was 13.1 minutes with 5 and 95 percentiles 1.6 minutes and 48.4 minutes, respectively. This shows that the duration of STAT1 pathway activation, which is in the range of 3 hours, is achieved by a combination of short nuclear residence times of phospho-STAT1 and dynamic STAT1 translocation.

4.3 STAT1 dimerization suppresses noise and increases pathway activation at the cost of responsiveness

In this section we investigate the role of STAT1 dimerization for the signal transduction pathway. The necessity of STAT1 dimerization for pathway activation (phosphorylated monomeric STAT1 is restricted to the cytoplasm) is an conspicuous property of the JAK/STAT1. The formation of transcriptionally active STAT1 SH2-dimers which can be imported into the nucleus is quadratically dependent on available monomeric phospho-STAT1 concentration. To investigate the impact of this nonlinearity in the system, we construct a hypothetical linear model by omitting the quadratic term in the dimer formation and compare the behavior of the hypotheical linear model to the model incorporating the correct dimerization term. Due to the linear dependence of the STAT1 dimer formation on the phospho-STAT1 monomers, the dose response curve of this hypothetical model (figure 4.5) shows an increased sensitivity for low stimulus activation. In contrast the original model

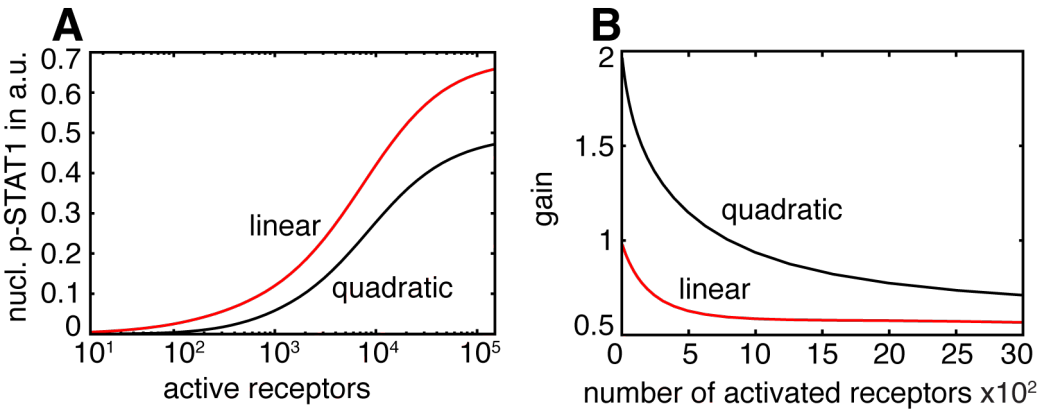

Figure 4.5: (**A**) The response curve to a stimulus of the model with the correct dimerization term (quadratic) is more sigmoidal and suppresses activation at lower stimuli than the response curve of a model with a hypothetical linear term (linear). (**B**) The relative amplification gain is increased by the quadratic dimerization term, because the probability of homo dimerization growth quadratically with the concentration of monomeric, cytoplasmic phospho-STAT1.

shows a more sigmoidal curve. To test this property experimentally, the pathway response at 40 minutes after stimulation was measured for several IFNγ concentrations. Though the fitting of the model was performed with data just at one IFN-γ concentration the simulated dose response curve for different IFN-γ concentrations agrees quantitatively with the data (figure 4.6). However, the data point at the highest IFN-γ concentration of 50 ng/ml disagrees with the modeled curve and indicates a decrease or at least a flattening of phospho-STAT1 for higher stimuli. Conclusively, the quadratic dependence of pathway activation on the signal input, functions as a

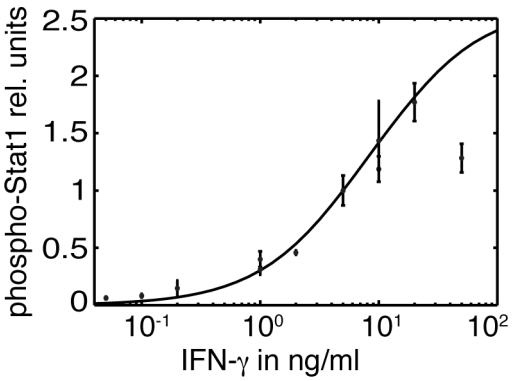

Figure 4.6: The mathematical model predicts quantitatively the response for stimuli with different IFN-γ concentrations. The data point for the highest IFN-γ concentration indicates some yet not known effect.

noise suppressing mechanism. Furthermore, the quadratic dependence of pathway activation on the concentration of phospho-monomers increases the ability of the pathway to amplify relative changes in the stimulus. This can be quantified by calculating the gain (relative sensitivity) Λ

$$\Lambda = \frac{\Delta\text{output}}{\text{output}} \cdot \frac{\text{input}}{\Delta\text{input}}.$$

The gain of the original model is higher than the gain of the hypothetical linear model (figure 4.5). We conjecture that stronger dimer formation, being necessary both for STAT1 nuclear import and DNA binding, would be beneficial for pathway activation. Varying the measured dissociation constant $K_\mathrm{d} = 50$ nM for dimer formation [156] over a range of 0-150 nM indeed shows, that the amplitude is increasing with stronger binding of the STAT1 monomers (figure 4.7 A). However, simulating pathway activation and subsequent stimulus removal shows that with stronger dimerization the relaxation rate (inverse of the relaxation time in equation 4.2) increases (figure 4.7 B) meaning that the pathway activation persists without signal input. Thus, strong dimerization both enhances efficient pathway activation and reduces pathway responsiveness. Therefore, the affinity must be such that a trade-off between both is achieved. There is no obvious function of the N-terminal STAT1 dimers but changing the affinity of N-terminal dimerization shows its influence on pathway activation and responsiveness. Either omitting N-terminal binding or increasing its affinity shows, that the N-terminal dimer formation also suppresses low signal activation by buffering the phospho-STAT1. On the other hand, a very high affinity would clearly decrease the activation amplitude strongly (figure 4.8).

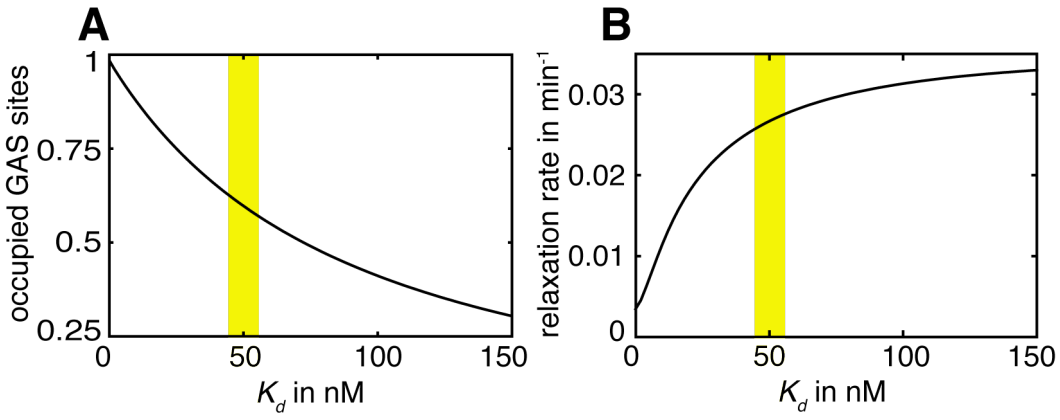

Figure 4.7: (**A**) The strength of pathway activation is increased with stronger dimer binding (lower dissociation constant K_d) whereas (**B**) the pathway responsiveness is reduced (indicated by a lower relaxation rate). The measured dissociation constant (yellow region) realizes a trade-off between this two effects.

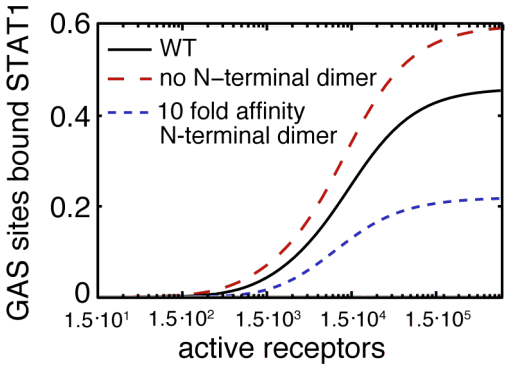

Figure 4.8: The formation of the transcriptional nonactive N-terminal dimers buffers low stimulus activation at the cost of reduced amplitude.

4.4 Sensitivity analysis shows that in the model network topology a trade off between efficiency and sensitivity must be realized

In section 4.3 we show, that the dissociation constant of the dimer formation exerts a big influence on both the amplitude and the response kinetics of the pathway. To systematically analyze the effect of all the network parameters on the pathway response, we calculated control coefficients by means of a sensitivity analysis. The control coefficient c of a measure x with respect to a parameter p is

$$c_p^x = \frac{p}{x}\partial_p x.$$

We are interested in the impact of the different parameters on the effectiveness and the timing of the pathway response. Therefore the signal strength and the time the pathway takes to respond to a change in signal input were taken as measures of interest x_i. To quantify the signal strength we chose the concentration of GAS site bound phospho-STAT1 $D_S(t)$ at steady state for a constant stimulation. To measure the timing of the pathway activation the time for the signal pathway to respond to a stimulus (response time) and the time to go back into the resting state after the stimulus is withdrawn (relaxation time) were calculated as defined in equations 4.2 and 4.1 (see also figure 4.3). Both the phosphorylation of STAT1 at the plasma membrane (determined by the number of active IFN receptors and the association rate constant) and its binding to GAS sites (determined by the number of accessible sites as well as the respective binding and dissociation rate constant) exert strong control on the response amplitude (figure 4.9). However, amplitude

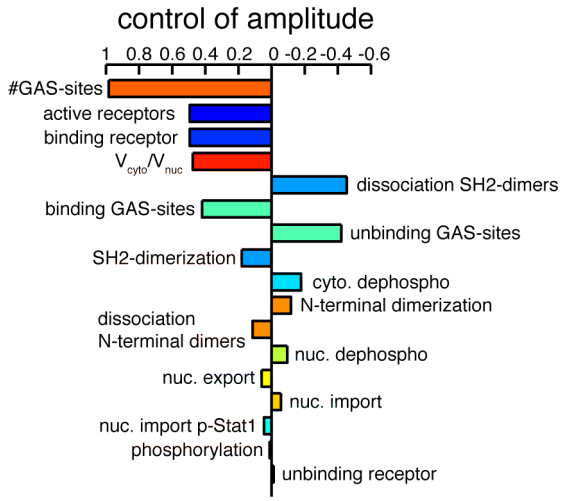

Figure 4.9: Control on the signal amplitude.

control is distributed over many processes in the network. In particular, we note that the stability of the phospho-dimers, the dephosphorylation rate constant in the cytoplasm and the cytoplasmic to nuclear volume ratio all have an appreciable impact on the response amplitude. A qualitatively similar picture is obtained for the response time to an IFN-γ stimulus (figure 4.10). The relaxation time after withdrawal of the stimulus is strongly controlled by the parameters of specific DNA binding (number of accessible GAS sites, binding and dissociation rate constant of STAT1 to the GAS sites) and the dissociation rate constant of the phospho-dimers (figure 4.10). The dephosphorylation in the cytoplasm has moderate control,

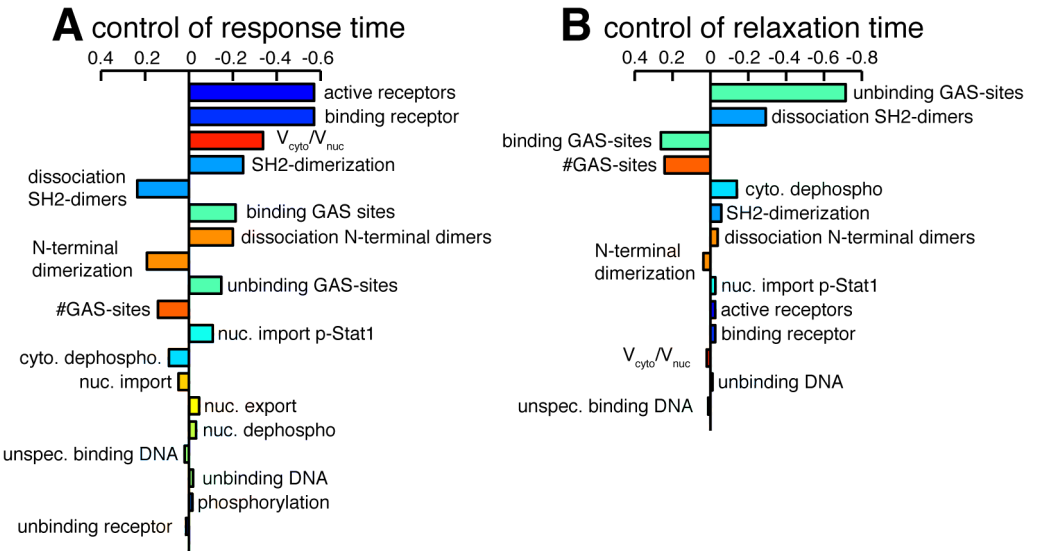

Figure 4.10: (**A**) Control on the response time (**B**) on and the relaxation time.

while the contribution of all other steps is considerably smaller. Thus, the rate of inactivation of the STAT1 pathway is mainly determined by the dissociation rate constant of the phospho-STAT1 dimers from the DNA and the dissociation rate constant of the phospho-dimers themselves. These two processes limit the access of the phosphatases to the activated STAT1. Many parameters exerting a strong control on the relaxation time also have a major impact on the signal strength, leading to a positive correlation between changes in signal duration and amplitude. It appears as if the pathway has to operate remote from an optimal signal transmission to account for a reasonable short deactivation time after stimulus withdrawal.

4.5 Perturbing STAT1 transport leads to suboptimal signal transduction

To rationalize, how the STAT1 transport influences the pathway characteristics, we investigated how the pathway behavior is changed under perturbed STAT1 transport. Both in the mathematical model and experimentally we investigated the impact of STAT1 transport alterations. For this, several STAT1 mutants with changed transport properties were cloned and experimentally tested. The mutants were designed by our collaborators (according to section 1.4).

4.5.1 Enhanced nuclear import: wNLS and sNLS mutant

By adding a nuclear localization sequence (NLS) to the STAT1 protein, the pathway could be tested with an enhanced nuclear STAT1 import. We investigated two mutants, one with a weak nuclear localization enhancement (wNLS) and one with a strong enhancement (sNLS). In contrast to the wild-type STAT1, displaying a nearly pan-cellular resting distribution, STAT1-wNLS and STAT1-sNLS showed a preferentially nuclear localization. As a control, a mutant with an added permuted, nonfunctional NLS sequence was tested, which exhibited the same resting distribution as wild-type STAT1. To simulate the STAT1-wNLS and the STAT1-sNLS in the model 0.2 min^{-1} and 2 min^{-1} were added to the import rate constant (k_8, k_{13}). Upon stimulation with IFN-γ, both in the model simulation as well as in the

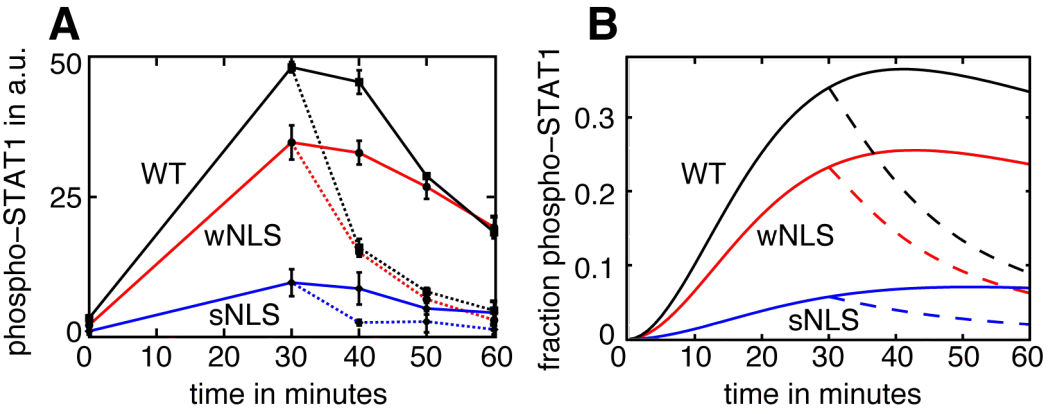

Figure 4.11: (**A**) With increasing strength of the nuclear localization sequence of the STAT1 mutant the measured amplitude of STAT1 phosphorylation after stimulation is decreasing due to the missing latent STAT1 in the cytoplasm. Blocking STAT1 phosphorylation by the kinase inhibitor staurosporine shows a direct drop of the phosphorylation level (dotted lines). (**B**) The model simulations reproduce the measured behavior and can be used to quantify the influence of the added NLS as the kinetics can be reproduced by enhancing the nuclear import of the latent STAT1 alone.

experiments the wNLS and LSN mutants (added mutated, nonfunctional NLS sequence) accumulate in the nucleus to the same degree as wild-type STAT1, while the already strong nuclear accumulation of the sNLS mutant is not further augmented by IFN-γ treatment. However, the phosphorylation level is decreased in the wNLS and sNLS mutants with enhanced nuclear import according to the strength of the additional NLS (figure 4.11 A). The model reproduces the measured behavior well (figure 4.11 B). Even the sNLS mutant, which appears to be fully nuclear already in resting cells, became phosphorylated. This observation implies that, like the wild-type, both NLS mutant proteins cycle between the cytoplasm and the nucleus and thus have access to the IFN-γ receptor/JAK complex at the plasma membrane. Application of the kinase inhibitor staurosporine caused a rapid decline of STAT1

phosphorylation, showing that the maintenance of phosphorylation requires continuous JAK activity. To test whether the phenotype of the STAT1-NLS mutants is due to enhanced import of latent STAT1 and/or the phospho-protein, we simulated separate increments of the import rate constants of the two subspecies. Accelerated import of latent STAT1 alone yields the same behavior (figure 4.11 A & B), whereas the wild-type behavior is fully retained when just the import of phospho-STAT1 is accelerated. Taken together, this shows that the phosphorylation rate can be strongly regulated by the velocity of nuclear import of latent STAT1. This is the case because the rapid nuclear import of latent STAT1 competes with its activation by the JAK.

4.5.2 Enhanced nuclear export: NES mutant

To enhance nuclear export, a STAT1 mutant (STAT1-NES) was generated by adding the STAT1-specific nuclear export signal (NES) sequence and tested thoroughly (section 1.4). This mutant shows a cytoplasmic localization in the unstimulated state. To model this mutant we added a nuclear export term with rate constant k_{NES} for all nuclear STAT1 species not bound to DNA. It seemed unlikely that the added NES is regulated by phosphorylation and/or dimerization. The strength of the added nuclear export can be calculated from the measured cytoplasmic to nuclear distribution of STAT1-NES in resting cells $X_{\mathrm{NES}} = 1/4$ and the latent nuclear export rate constant and nuclear import rate constant (k_{12} and k_13). This yields

$$k_{\mathrm{NES}} = X_{\mathrm{NES}}^{-1} \cdot k_{13} - k_{12} = 0.32 \ \mathrm{min}^{-1}.$$

Note that with our definitions of the rate constants ρ enters the differential equations for the nuclear concentration change. So for all nuclear species we can write

$$\partial_t S_{\mathrm{nuc}} \sim -\rho \ k_{\mathrm{NES}} \ S_{\mathrm{nuc}}.$$

Simulation with the given parameter set and the added NES reaction gave a prediction for the activation kinetics (phospho-STAT1 after IFN-γ treatment) and the dephosphorylation kinetics (staurosporin treatment after 45 minutes of IFN-γ stimulation) of the NES mutant. The predicted curves agree quantitatively with the measured time courses (figure 4.12). The time course showed that STAT1-NES had a higher and more prolonged phosphorylation in response to an IFN-γ stimulus (40-50 % of total STAT1 is phosphorylated) than the wild-type protein (30-40 % of total STAT1 is phosphorylated). A similarly enhanced phosphorylation was also observed for the STAT1-NLS mutant. Indicating, that the high STAT1 concentration

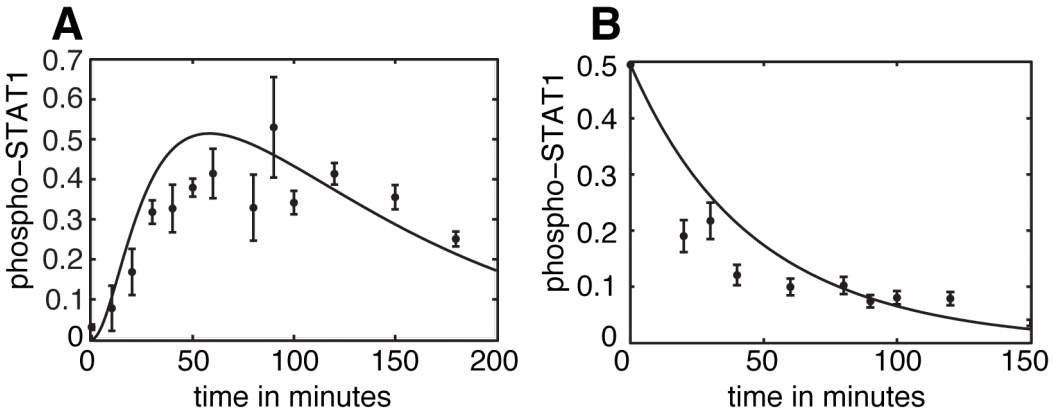

Figure 4.12: (**A**) The measured phosphorylation kinetics of STAT1-NES under IFN-γ stimulation. (**B**) The measured dephosphorylation kinetics of STAT1-NES. To measure the dephosphorylation, after 45 minutes of IFN-γ stimulation cells were treated with a kinase inhibitor (at 0 minutes). Both, phosphorylation and dephosphorylation kinetics of STAT1-NES are quantitatively predicted by the mathematical model simulation (black lines).

in the cytoplasm and with that a strong JAK activity combined with comparatively weak phosphatase activity, is the main cause for the observed hyperphosphorylation. Interestingly, the model predicts that the concentration of phospho-STAT1 in the nucleus after IFN-γ stimulation in the STAT1-NES mutant is very similar to the STAT1-WT (figure 4.13). Assuming, that the level of phospho-STAT1 is directly

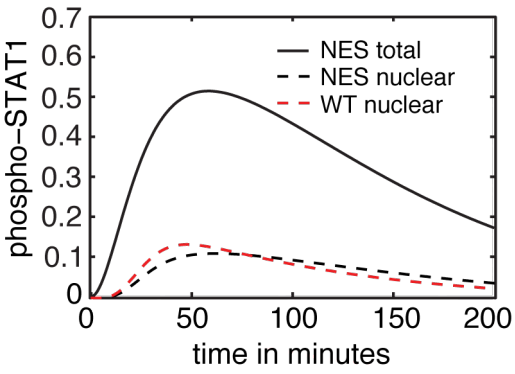

Figure 4.13: The simulation shows a very similar concentration of nuclear phospho-STAT1 for the wild-type STAT1 (dashed red curve) and the STAT1-NES mutant (dashed black curve).

related to transciptional activity we tested this prediction by comparing expression kinetics of six STAT1 target genes after IFN-γ stimulation in STAT1-NES cells to STAT1-WT cells. Indeed we did not find any significant differences (figure 4.14,

rt-PCR carried out by Andreas Begitt, *Queen's Medical Centre Nottingham*). The

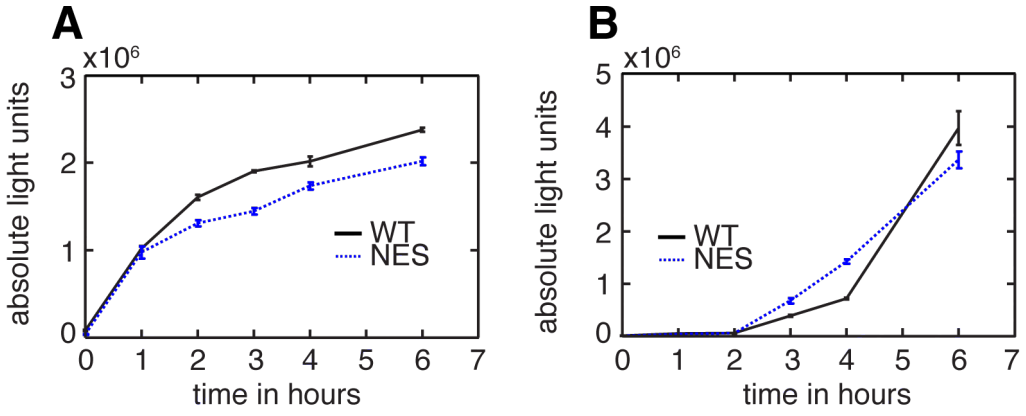

Figure 4.14: The transcriptional activation of two genes ((**A**) LMP-2 and (**B**) MIG-1) in the wild-type STAT1 cells (black curve) and in the cells with STAT1-NES (dotted blue curve) is very similar. Four further genes show the same result (see appendix A.3).

concentration flow of STAT1 after IFN-γ stimulation is bigger for the STAT1-NES compared to the STAT1-WT. The wild-type like nuclear phospho-STAT1 concentration in the STAT1-NES mutant can be explained by a compensation of the additional nuclear export of phospho-STAT1 decreasing the nuclear phospho-STAT1 concentration due to the NES and the hyperphosphorylation increasing the nuclear phospho-STAT1 concentration. Moreover, the model of the NES mutant also reproduces the weaker phosphorylation observed in the presence of LMB (Leptomycin B a nuclear export blocker), which blocks active nuclear export (figure 4.15). The

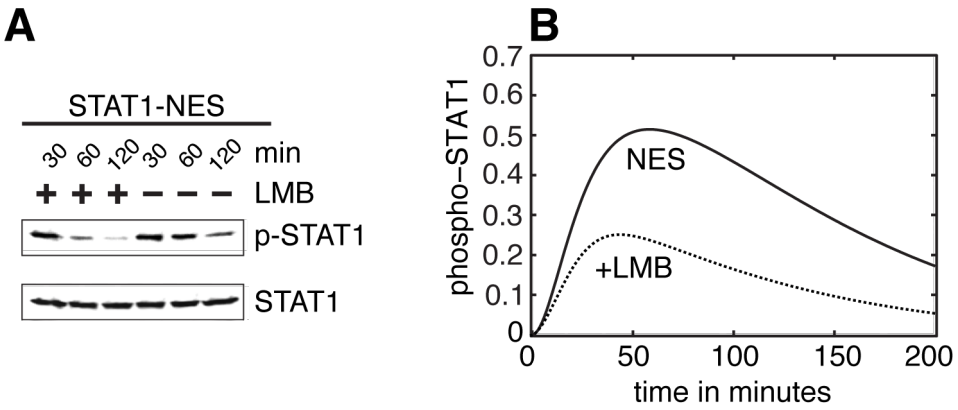

Figure 4.15: Phosphorylation of the STAT1-NES is reduced upon treatment with the export blocker LMB (**A**) measured and (**B**) simulated.

model indicates that LMB reduces STAT1-NES phosphorylation through two effects: first the nuclear retention subjects the phospho-dimer to the nuclear phosphatases

rather than the lower-activity cytoplasmic phosphatases; and second the decreased export rate of unphosphorylated STAT1-NES retards its rephosphorylation. Thus, the mathematical model reproduces the phenotype of the STAT1-NES quantitatively simply by implementing a rate for the added nuclear export of STAT1 with strength determined by the measurements of the cytoplasmic to nuclear STAT1 distribution in unstimulated cells. Remarkably, the transcriptional response of the STAT1 pathway is robust against an enhancement of the STAT1 nuclear export rate, including the unphysiological export of the phospho-protein.

4.6 Dimer transitions

It is still unclear whether changing from an N-terminal bound to a SH2 bound STAT1 dimer requires the dissociation of the two STAT1 monomers [156] or if alternatively there exists a direct transition between the two dimer states [91] (figure 4.16). Regarding the proposed mechanism for a direct transition, we implemented an alternative model allowing a change of dimer conformers without dissociation into monomers (nondissociation model from here on) , which was compared to the mathematical model we established lacking the direct transition (dissociation model from here on). For the nondissociation model, we additionally included two free

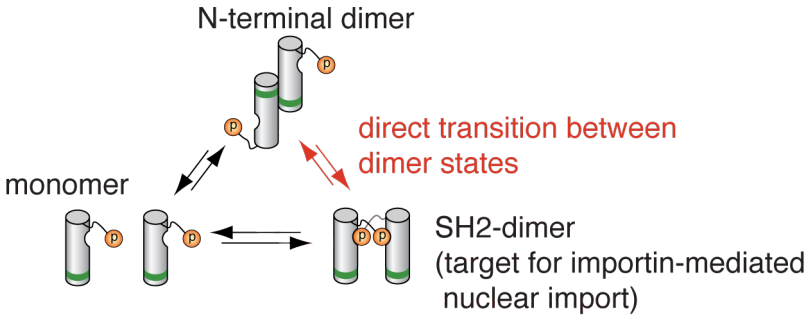

Figure 4.16: It is a ongoing debate if there exists a direct transition from the N-terminal dimer to the SH2 dimer (indicated by red arrows).

parameters (on- and off-rate constant for the direct transition between dimer conformations). With this additional parameters we fitted the nondissociation model to the data (section 3.2). Table 4.1 shows the best-fit parameter values. The model yielded a very similar fitting performance compared to the dissociation model (minor change in the Akaike information criterion [3], meaning a better description of

Reaction	value
Activation IFN receptor/Jak complex	0.06 min^{-1}
Deactivation IFN receptor/Jak complex	0.02 min^{-1}
Receptor degradation	0.01 min^{-1}
Stat1 phosphorylation & dissociation	120 min^{-1}
Dephosphorylation in the cytoplasm	0.024 min^{-1}
Dephosphorylation in the nucleus	4.5 min^{-1}
Transition N-terminal dimer to phospho-tyrosine/SH2 dimer	0.6 min^{-1}
Transition phospho-tyrosine/SH2 dimer to N-terminal dimer	0.08 min^{-1}

Table 4.1: Best-fit parameters for the nondissociation model

the data on the cost of more free parameters). Thus, it is not possible to deduce the existence or nonexistence of the direct dimer transition step by a comparison of the model performance from the presented data. In the dissociation model the direct transition between the dimer conformations is on the same timescale as the dissociation of the dimers into monomers (red and black arrows, figure 4.16). The direct transition shifts the equilibrium to the parallel dimer, which is subjected to importin-mediated nuclear import. In the dissociation model the rate-limiting process for nuclear import of phospho-STAT1 is the formation of the parallel dimer. We experienced that the measured pathway dynamics could only be simulated in this model by using enhanced dimerization rate constants. Because the direct transition in the nondissociation model allows the formation of parallel dimers from phosphorylated N-terminal dimers, the nondissociation model is capable of reproducing the data also with the *in vitro* measured on and off rates for STAT1 dimer formation (half-life for dimers $\sim$ 30 minutes as compared to $\sim$ 1 minute with enhanced rate constants). Note that this is only achieved with a high transition rate between the two dimer states ($\sim 10^3$ min^{-1}) and a strong nuclear phosphatase activity (30 min^{-1}). Comparing the dose response curves of the STAT1 mutants for different IFN-γ concentrations of the dissociation and the nondissociation model with the measured responses the nondissociation model performs better in explaining the STAT1-ΔNLS dose response curve (figure 4.17).

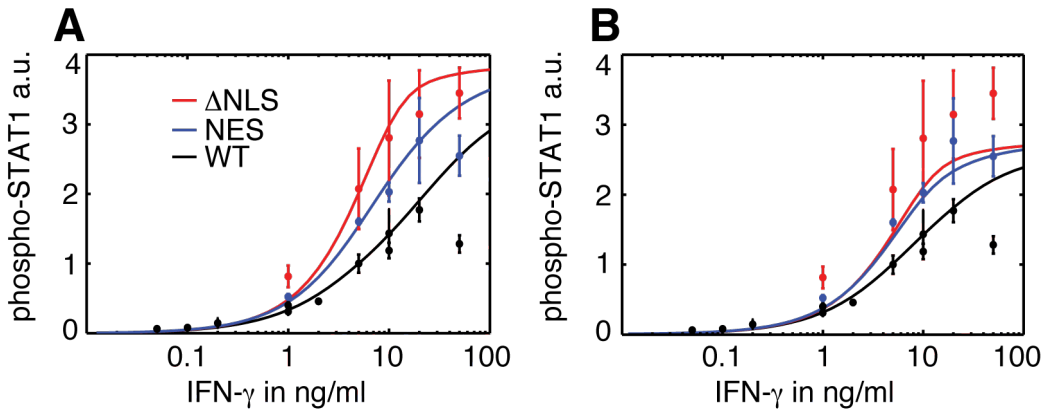

Figure 4.17: (**A**) The prediction of the nondissociation model of the dose response curves of STAT1-WT,-ΔNLS and -NES is slightly better than (**B**) the prediction of the original, dissociation model. Especially, this is evident for the dose response cureve of the STAT1-ΔNLS.

5 Conclusions and discussion JAK/STAT1 pathway

We established a mathematical model of the JAK/STAT1 pathway based on mass action kinetics. With adequate kinetic measurement and quantifications of nucleocytoplasmic STAT1 distributions all unknown model parameters could be well determined, which is shown by small confidence intervals. We utilized the mathematical model to predict both, dose response curves as well as the behavior of STAT1 transport mutants correctly. Furthermore in contrast to many previous models [135, 130, 64] we could infer design principles of the network topology.

Just $\sim$ 30% of the STAT1 molecules are found to be phosphorylated at maximal pathway stimulation for a standard IFN-γ stimulus. The nuclear concentration of the phospho-STAT1 under stimulating condition is quite high, though. It was necessary to include the ratio of compartment volumes, which is significantly different from one, into the pathway description to correctly reproduce the observed behavior and to quantitatively estimate the model parameters. These considerations should be made for every model, where transport processes play an important role and was repeatedly omitted in previous models [135, 121]. A small nuclear volume is concentrating the inflowing phospho-STAT1. Thereby the nuclear phospho-STAT1 is dependent on the cytoplasmic to nuclear volume ratio ρ. To experimentally investigate if the JAK/STAT1 pathway functions similarly in other cell lines, or if a modification of the model or the model parameter has to be made might give further insights into the design of the JAK/STAT1 pathway. Is the pathway tuned differently in cells with another ratio of cytoplasmic to nuclear volume? For examples in t-lymphocytes with ρ equal or even less than one, the JAK/STAT pathway plays an important role [114]. It would be interesting if the missing concentrating effect of the nucleus is somehow compensated. This could be realized by increased number of receptors, increased sensitivity of the target gene promoters or various other mechanisms.

We show that the homo dimerization of STAT1 via SH2 Tyr701 interaction is a key element of the JAK/STAT1 pathway activation in matters of shaping the response. By its nonlinear nature, dimerization suppresses noise and low stimuli activation. Furthermore the dimerization increases the relative signal amplification of the pathway. In general these two effects can be a benefit for all self interacting proteins (e.g. clustering of receptors [10, 167, 133] or p53 protein oligomerization [115, 60]).

By exploiting the mathematical description of the pathway we were able to deduce the mean time a phospho-STAT1 molecule resides in the nucleus until it is reimported into the cytoplasm (after preceding dephosphorylation) and available for reactivation. This time turned out to be rather short ($\sim$ 10 min) compared to the duration of pathway activation ($\sim$ 200 min). Conclusively, the pathway activation is sustained by a combination of short nuclear residence times of phospho-STAT1 and fast dynamic STAT1 translocation. A network sensitivity analysis showed, that for many parameter values a trade off between signal strength and pathway responsiveness must be realized. This is especially evident in the dimerization affinity. On one hand a strong bound SH2 dimer increases the signal amplitude, but on the other hand it takes a long time to dissociate and thereby prolongs pathway activation despite signal removal. The model indicates that the measured dimer dissociation constant lies in an optimal range, where the amplitude is reasonably high and the responsiveness is fast. This trade off is an inherent property of all biologic binding reactions, simply because stable binding goes with long half-lifes. This can just be circumvented by energy dependent enzymatic reactions. In summary the nuclear residence time of phospho-STAT1, the response time and the relaxation time show that the network is tuned such that the level of nuclear activated STAT1 is tightly coupled to the receptor activation time course. The design of the pathway seems to be optimized in respect to fast signal transduction without too much loss of signal strength.

The model was fitted with data of the pathway response at an IFN-γ concentration of 5 ng/ml. Nevertheless, the model is able to predict quantitatively measured dose response curves for IFN-γ concentrations. Only for the highest concentration of 50 ng/ml IFN- γ the experiment showed a decrease in the pathway activation. The decline of phospho-STAT1 with increasing stimulus could not be explained by the model. If this is not an experimental artifact it might indicate a reaction or a player, not included into the network model, which becomes important for the pathway response at high IFN-γ. There are many possibilities for such a player like PIAS, SOCS and cross talk with other pathways.

The underlying mechanism of STAT1 dimerization is mostly understood, but there is an ongoing debate of the timescale of this process and if a direct transition between the conformational different dimers (N-terminal dimer and SH2 dimer) is possible [91, 156]. In line with our collaborators we did not include a direct transition into the model. The mathematical model indicates, that the dimer formation is rather fast (half-life in the order of one minute). It was also possible to fit the data with a model allowing for a direct transition of the dimer states and a slower dimerization with a similar AIC. Thus, it is not possible to deduce the existence or non existence of the reaction by the fitted data. Interestingly, the dose response curves of the STAT1 mutants were predicted best by the model which incorporates fast dimerization and a direct transition.

The model could be verified by testing several predictions with additional measurements. Besides the dose response curve for different stimuli the simulation of the STAT1 transport mutants (wNLS, sNLS, LSN) qualitatively agreed with the measurements. The STAT1 phosphorylation kinetics of the STAT1 NES mutant are predicted correctly. Furthermore, the model predicted a compensation of the hyper phosphorylation due to more available latent STAT1 in the cytoplasm and the additional nuclear export of phospho-STAT1. This compensation results in the same concentration of phospho-STAT1 in the nucleus in the simulations for STAT1-WT and STAT1-NES. Indeed mRNA measurements of six STAT1 target genes after stimulation did not show any differences between STAT1-WT and STAT1-NES. This findings are in line with the prediction. However, the response of the target genes is modulated by the detailed mechanism of their gene activation, thus a separate measurement of nuclear phospho-STAT1, in both the wild-type cells and in the cells with STAT1-NES, would be necessary to clearly verify the prediction. The nuclear retention of STAT1 is a special property of the STAT1 molecule. The phospho-STAT1-NES is not any longer confined in the nucleus and the pathway response of the STAT1-NES mutant shows that function of the pathway is not dependent on nuclear retention of STAT1. However, this comes at the cost of higher STAT1 phosphorylation level and a slightly slower pathway response time. Arguably the nuclear retention of STAT1 increases the efficiency of the pathway activation.

In the future it would be of interest to extent the modeled network to the effect of PIAS and SOCS and interaction with other STAT members such as STAT2 to increase the scope of the model. In many of our measured phosphorylation time courses a small dip (decrease and then again increase) is observed after the maximum. This effect is also observed in the data presented in [135, 82]. This might hint to a more complex regulation of receptor activation or another protein involved in STAT1 activation.

Part II

Mathematical Modeling of DNA damage response and G1-S transition in neuroblastoma

6 Introduction Neuroblastoma

Cancer is beyond the most frequent and severe diseases of modern society. Due to its complex and heterogeneous nature much is still unknown. Because of the young age of the patients, embryonic tumors show a relatively low number of mutations. One hope is to use the low complexity of these embryonic tumors, to learn more about the mechanisms of cancer development and possible therapies.

6.1 Neuroblastoma

Neuroblastoma is a pediatric tumor of the sympathetic nervous system and responsible for 8-10% of all childhood malignancies [20]. It is the most common extra cranial solid tumor occurring in childhood. The primary tumor often arises in the adrenal gland from neural progenitor cells but also with occurrence in the whole sympathetic nervous system [160].

What is special about neuroblastoma is that the progression of the disease is very diverse. On one hand the rate of spontaneous regression, where the tumor vanishes even without treatment is 10-100 fold higher compared to other known similar events in human tumors [111]. On the other hand there are patients were the neuroblastoma is of a highly aggressive type and does not response to several treatment options, with relapse after treatment, resistance to chemotherapy and low survival rate [87]. To improve treatment by adapting the patients care according to the type of neuroblastoma and to increase therapy success, it is important to understand better the differences of this two types of neuroblastoma and how they arise.

To classify patients and tumor spread an international neuroblastoma staging system was established [11] dividing the patients into stages from I to IV with the special stage IVs. IVs is unique in neuroblastoma and consists of neuroblastoma diagnosed in patients younger than one year with limited dissemination of the tumor cells to skin liver or bone marrow and shows a high rate of spontaneous regression. Several known markers, such as age at diagnosis, DNA index, histology and structural chromosomal alterations are associated with the patients outcome in neuroblastoma. One of the prognostic factors which is related closely to the cellular mechanism of the disease is the copy number of the oncogene *MYCN* found in the neuroblastoma cells [123, 12]. Patients with *MYCN*-amplified neuroblastoma (incidence rate $\sim$ 20%)

show a very low survival rate despite multiple treatment [96].

6.2 The MYCN oncogene

MYCN belongs to the MYC family of proto-oncogenes, which encode for transcription factors of the basic-helix-loop-helix-zipper (bHLHZ) class. The observed effect of MYC ranges from enhanced proliferation, suppressed differentiation, angiogenesis and genomic instability [1, 112] to enhanced apoptosis sensitivity in *MYCN*-amplified cells [38, 159]. One of the major goal of this work is to rationalize the impact of aberrant MYCN protein levels in neuroblastoma on the cell guarding regulatory network of p53 and on the E2F1-pRB cell cycle control axis.

6.3 Neuroblastoma and the p53 pathway

The p53 protein, encoded by the *TP53* gene, is a key protein for the cell to secure genetic integrity. Overcoming these save mechanisms of the p53 pathway is a hallmark of cancer and with mutated p53 found in roughly 50% of all human tumor cells [152] it is the most commonly mutated tumor suppressor gene. p53 has a major role in regulating many important cell decisions as apoptosis, differentiation, inhibition of angiogenisis and metastasis as well as DNA repair and cell cycle arrest [78]. p53 regulation gets input from many different pathways and has been studied extensively. The main regulation of p53 itself happens via posttranslation modifications [67]. As in unstressed cells p53 has a short half life of 20 minutes, so the p53 protein level is relatively low. In response to stress signals p53 is stabilized and forms transcriptional active tetramers [132]. There are many p53 target genes ranging from proteins inducing cell cylce arrest (e.g. p21) to apoptosis inducing genes (e.g. PUMA, BAX1) and its own antagonist MDM2 [90].

Surprisingly, the frequency of p53 mutation in neuroblastoma is very low (2%) [142]. However, in tumor samples taken after relapse of the tumor the mutation rate is significantly higher [16, 18]. The mechanisms which renders the p53 pathway in the wild type p53 neuroblastoma cells disfunctional and what role MYCN might play are unknown. It was reported that besides many target genes, MYCN activates transcription of both p53 and MDM2 in neuroblastoma [129, 21].

6.4 Cell cycle regulation and the pRB-E2F1 axis in neuroblastoma

The cell cycle consists of several distinct phases (G1, S, G2 and M phase). To monitor its environmental condition and also to control if every step in the division process is correctly finished, the cell has evolved several check points. At the end of the G1 phase there is a check point where the cell decides if it commits to cell division dependent on several parameters including growth factor signaling. If the cell crosses this so called restriction point (R-point) cell division becomes independent of growth factor level and subsequent removal of growth factors does not disrupt the execution of cell division [108, 166]. It was shown that this switch-like passage of the R-point coincide with upregulation of the E2F1 protein, which shows bistable behavior in embryonic fibroblasts[161, 164].

Entry into the cell cycle is regulated by the transcription factors E2F1, -2 and -3a and its repressors the pocket proteins pRB (the retinoblastoma tumor suppressor), p107 and p130. The pRB-E2F pathway is associated with the regulation of DNA replication initiation and plays a critical role in cell proliferation [103, 154, 4]. The importance of the pRB-E2F pathway is further evidenced by the finding that it is deregulated in almost all cancer cells [104]. E2F1 is a key component of the pRB pathway and can activate cell cycle progression and passage from G1 phase to S phase. In a hypophosphorylated state pRB can bind to E2F1 and represses its transcriptional activity. Upon phosphorylation of pRB by CDKs (cyclin dependent kinases), which are active in complex with D- and E-type cyclins, E2F1 is released and activates target genes associated with cell cycle progression.

It is observed, that several neuroblastoma cell lines have a fraction of cells in G1 phase which after DNA damage induction do not arrest. Especially in *MYCN*-amplified cell lines an impaired G1 arrest is observed [17]. This cells do not arresting in G1 after chemotherapy and potentially accumulate further genomic instabilities by committing to cell division despite DNA damage giving rise to additional malignant transformations. This might be a possible reason for the enrichment of p53 mutations in relapsed neuroblastoma [16, 18]. Consequently, to understand and eventually target this impaired G1 arrest might be highly valuable.

7 Modeling of the p53-MDM2 core module in neuroblastoma

In this chapter we investigate the MYCN related dysfunction of the DNA damage response in neuroblastoma cells. A noncomplex model of the p53-MDM2 core module is established which shows an universal steady state change under p53 activation governing the DNA damage response. The model is capable of reproducing protein level differences in several neuroblastoma cell lines. Interestingly, the model can also qualitatively reproduce measured responses to DNA damage and MDM2 inhibition in two subclones of the conditionally *MYCN* expressing neuroblastoma SH-EP T21N cells. Data from the *MYCN*-amplified cell line, IMR5-75, indicates, that for high MYCN levels the perturbation of the pRB-E2F1 axis becomes relevant.

7.1 A simple model of the p53-MDM2 core module shows a universal steady state in phase space and can produce various p53 responses

We investigated the MYCN-dependent p53 response in the neuroblastoma cells. Upon DNA damage p53, one prominent factor in determining the cell response, is activated. This is thought to be conducted by stabilizing p53 via post-translational modifications and subsequent forming of transcriptional active p53 tetramers [67]. p53 activates its own antagonist MDM2, a E3 ligase, that targets p53 for proteosomal degradation [54]. This forms a negative feedback loop on p53 (figure 7.1 A). The possible behavior of such a negative feedback loop can be very diverse and vary from oscillations to homeostatic behavior. We establish a simple model with the most important interactions to analyze the possible responses of this p53-MDM2 core module. We include two states of p53 in the model, one is inactive as a transcription factor (concentration of inactive p53 $x_{\mathrm{i}}(t)$) and one is active (concentration of active p53 $x_{\mathrm{a}}(t)$). The rate constants of activation and inactivation are k_{on} and k_{off}, respectively. The induction of MDM2 $y(t)$ by p53 is modeled by introducing a hill function with hill coefficient of 4 to account for the postranslational modifications, the tetramerization and the DNA binding. Furthermore we allowed for basal production and degradation of p53 (rate constant v_{x} and δ_{x}) and MDM2 (rate constant v_{y} and δ_{y}). We assumed that the activation of p53 stabilizes the protein

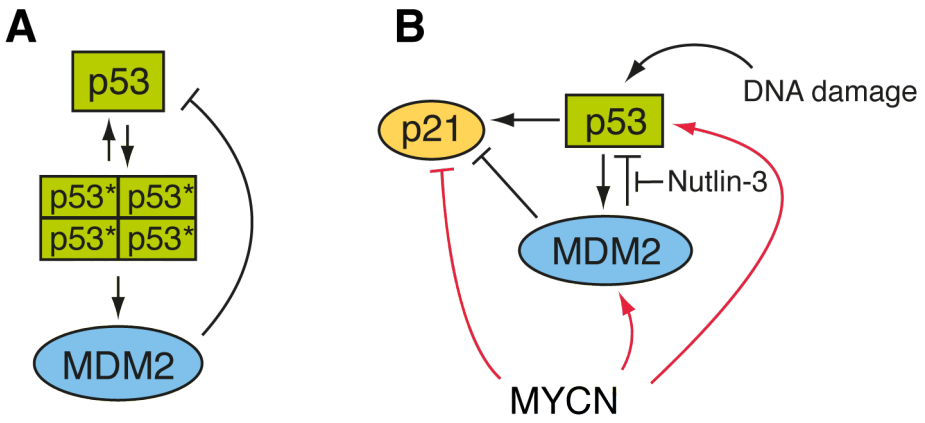

Figure 7.1: (**A**) The negative feedback loop of p53. By posttranslational modifications p53 is activated and can form transcriptional active tetramers. One target gene of p53 is *MDM2*. The E3 ligase MDM2 tags p53 for proteosomal degradation. (**B**) The p53-MDM2 core module. MYCN induces both p53 and MDM2 and inhibits the p53-mediated transcriptional activation of p21. Additionally the interactions of p53-activating DNA damage and Nutlin-3, which inhibits the binding of MDM2 and p53, are depicted.

and with that prevents its degradation. The resulting system of ordinary differential equations then reads

$$\begin{aligned}
\partial_t\, x_\mathrm{i}(t) &= v_\mathrm{x} - \delta_\mathrm{yx}\, y(t)\, x_\mathrm{i}(t) - k_\mathrm{on}\, x_\mathrm{i}(t) + k_\mathrm{off}\, x_\mathrm{a}(t) - \delta_\mathrm{x}\, x_\mathrm{i}(t) \\
\partial_t\, x_\mathrm{a}(t) &= k_\mathrm{on}\, x_\mathrm{i}(t) - k_\mathrm{off}\, x_\mathrm{a}(t) \\
\partial_t\, y(t) &= v_\mathrm{y} + v_\mathrm{xy} \left[\frac{x_\mathrm{a}(t)}{K_\mathrm{xy} + x_\mathrm{a}(t)}\right]^4 - \delta_\mathrm{y}\, y(t).
\end{aligned} \tag{7.1}$$

To parametrize the change of p53 and MDM2 on a change in p53 activity (e.g. DNA damage) the fraction of active p53 λ is introduced

$$\begin{aligned}
\lambda &= \frac{x_\mathrm{a}(t)}{x_\mathrm{a}(t) + x_\mathrm{i}(t)} = \frac{x_\mathrm{a}(t)}{x(t)} \\
x_\mathrm{a}(t) &= \lambda\, x(t) \quad \wedge \quad x_\mathrm{i}(t) = (1-\lambda)\, x(t),
\end{aligned}$$

with concentration of total p53 $x(t) = x_\mathrm{a}(t) + x_\mathrm{i}(t)$.

7.1.1 The simple model of the p53-MDM2 core module does not exhibit an oscillatory regime

For the fraction of active p53 λ holds

$$\begin{aligned} x_\mathrm{a} &= \frac{k_\mathrm{on}}{k_\mathrm{off}}\, x_\mathrm{i} \\ \Rightarrow \lambda &= \frac{x_\mathrm{a}}{x_\mathrm{a}+x_\mathrm{i}} = \left(1+\frac{k_\mathrm{off}}{k_\mathrm{on}}\right)^{-1}. \end{aligned}$$

Under quasi-steady state assumption for the p53 activation the equations 7.1 becomes

$$\begin{aligned} (1-\lambda)\,\partial_t\, x(t) &= v_\mathrm{x} - \delta_\mathrm{yx}\, y(t)\,(1-\lambda)\, x(t) - \delta_\mathrm{x}\,(1-\lambda)\, x(t) \\ \partial_t\, y(t) &= v_\mathrm{y} + v_\mathrm{xy}\left[\frac{\lambda\, x(t)}{K_\mathrm{xy}+\lambda\, x(t)}\right]^4 - \delta_\mathrm{y}\, y(t). \end{aligned} \tag{7.2}$$

To analyze the steady state of the system we solve $\partial_t\, x = 0 \wedge \partial_t\, y = 0$, where the arguments are omitted to indicate the concentration of the proteins at steady state, $x := x(t \to \infty)$, $y := y(t \to \infty)$. By solving the upper equations for y we get

$$\begin{aligned} y &= \frac{v_\mathrm{x} - \delta_\mathrm{x}\,(1-\lambda)x}{\delta_\mathrm{yx}\;(1-\lambda)\;x} \\ y &= \frac{v_\mathrm{y}}{\delta_\mathrm{y}} + \frac{v_\mathrm{xy}}{\delta_\mathrm{y}}\left[\frac{\lambda\, x}{K_\mathrm{xy}+\lambda\, x}\right]^4. \end{aligned}$$

This system can be solved graphically by plotting the right hand sides against x for a chosen parameter set (figure 7.2). Then the intersection of the two curves gives the steady state of the system. The trajectories into the steady state from the initial conditions can be visualized by additionally drawing the vector $(\partial_t x(t), \partial_t y(t))$ at sample points. An oscillatory regime of the system is then indicated by closed circles of these trajectories. For this very simple model no oscillatory region in parameter space could be found but spiral shaped trajectories exist.

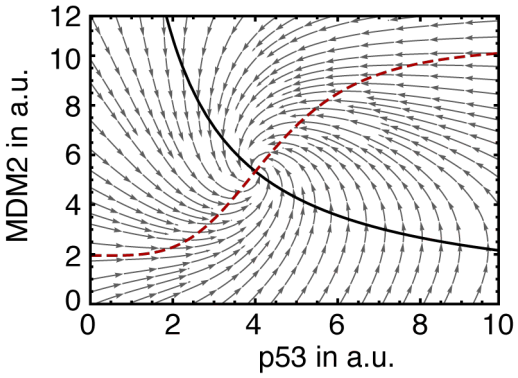

Figure 7.2: The steady state can be determined graphically (the intersection point of the two curves). The vector of the derivatives gives the direction of the trajectories in the phase space (arrows). If the arrows formed cycles this would correspond to a oscillatory regime.

7.1.2 The model shows an unique behavior in phase space and the impact on total p53 is parameter dependent

We wanted to investigate the steady states of the differential equation system 7.1 under change of active p53 fraction λ. Thus, we simulated the system for varying λ. The simulation showed that the steady state exhibits a universal behavior which can be seen plotting the λ dependence of the solutions in phase space (figure 7.3). With increasing λ there are four regions of the graph with the following regimes

1. **p53 ↑, MDM2 →**
   For small λ, the total amount of p53 increases due to its own activation, but in a regime, where MDM2 is not sensitive to activated p53. Thus, the negative feedback is not affecting the p53 concentration.

2. **p53 ↓, MDM2 ↑**
   p53 is activated and induces MDM2. This leads to an increase of MDM2 and via the negative feedback to a decrease in total p53 concentration.

3. **p53 →, MDM2 ↑**
   p53 is activated further and induces MDM2. But the p53 stabilization by activation is compensated by the increasing degradation by MDM2.

4. **p53 ↑, MDM2 →**
   For large (close to one) λ the p53-mediated MDM2 induction is saturated, and the active p53 is increasing.

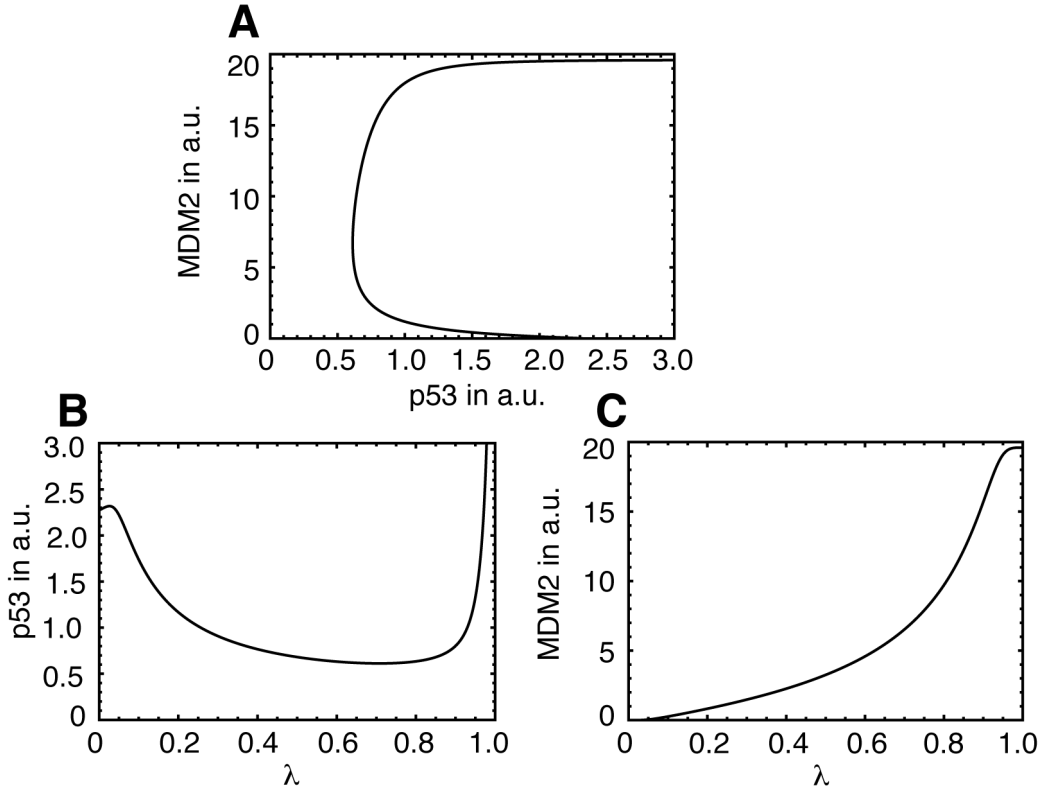

Figure 7.3: (**A**) Steady state of p53 and MDM2 as function of λ. The curve is s-shaped (the region where p53 is increasing for small λ is very small). (**B**) p53 as function of λ. The increase for small λ is here visible. (**C**) MDM2 as function of λ, which is always growing monotonically.

This gives a S-shaped curve in phase space (p53 on the x-axis and MDM2 on the y-axis) or, dependent on the parameters, any curve in between (with less inflection points). If the negative coupling of MDM2 and p53 is very weak or zero, both proteins are just growing monotonically with increasing p53 activation. It is widely believed that the activation of p53 causes a stabilization and that lead to increasing levels of p53 [155]. However, simulating trajectories under change of p53 activation λ showed that even this simple model can produce several qualitatively different p53 responses (figure 7.4). So total p53 can either increase, stay constant or even decrease after activation. MDM2 can show a sustained or a transient increase.

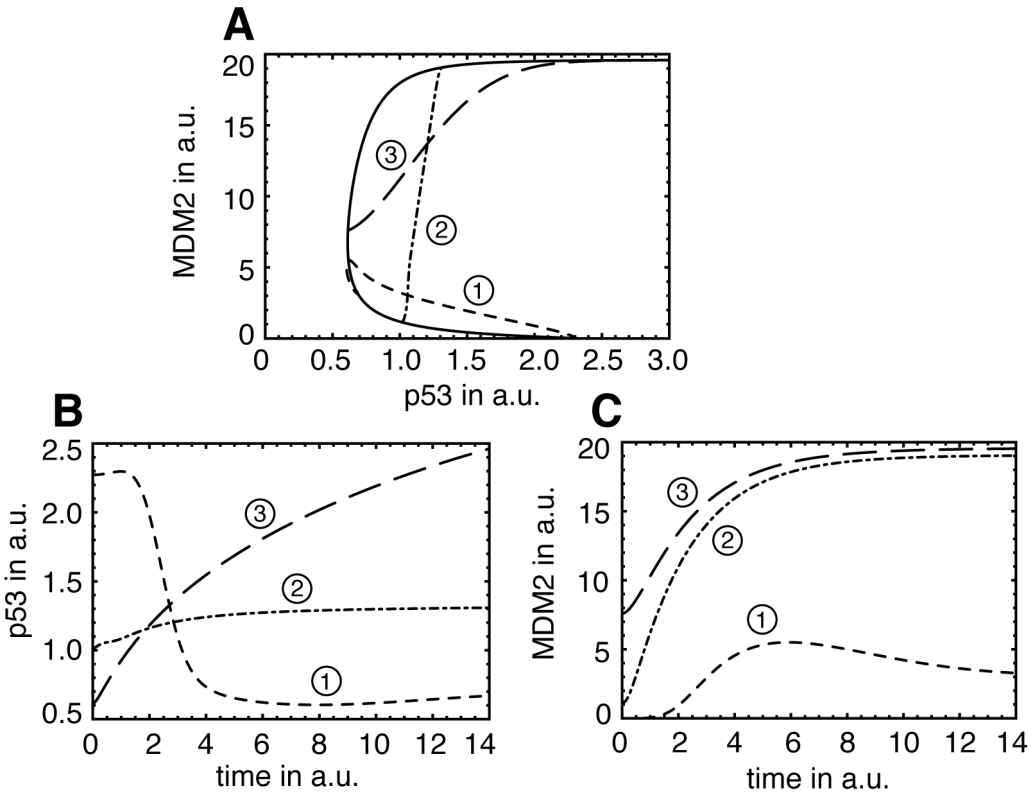

Figure 7.4: (**A**) Steady state of p53 and MDM2 as function of λ with three different trajectories (1, 2, 3). (**B**) Possible corresponding responses of total p53 as function of time can increase, stay constant or even decrease (3,2 and 1, respectively). (**C**) We found both increasing MDM2 or transiently increasing MDM2 for the three trajectories.

7.2 An extended model of the p53-MDM2 core module reproduces MYCN induced differences in protein levels between different NB cell lines

We extended the model of the p53-MDM2 core module to account for the influence of MYCN and the regulation of the p21 protein (figure 7.1 B) and compared the model simulation with measured protein levels in different cell lines. Additionally, we included a Michaelis Menten term for the p53 degradation via MDM2, because the data indicated a nonlinear dependency. The equation system 7.1 with this extension then becomes

$$
\begin{aligned}
\partial_t\, x_{\mathrm{i}}(t) &= v_{\mathrm{x}} + n_{\mathrm{x}}\, m(t) - \delta_{\mathrm{yx}}\, \frac{y(t)}{K_{\mathrm{yx}} + y(t)}\, x_{\mathrm{i}}(t) - k_{\mathrm{on}}\, x_{\mathrm{i}}(t) + k_{\mathrm{off}}\, x_{\mathrm{a}}(t) - \delta_{\mathrm{x}}\, x_{\mathrm{i}}(t) \\
\partial_t\, x_{\mathrm{a}}(t) &= k_{\mathrm{on}}\, x_{\mathrm{i}}(t) - k_{\mathrm{off}}\, x_{\mathrm{a}}(t) \\
\partial_t\, y(t) &= v_{\mathrm{y}} + n_{\mathrm{y}}\, m(t) + v_{\mathrm{xy}} \left[\frac{x_{\mathrm{a}}(t)}{K_{\mathrm{xy}} + x_{\mathrm{a}}(t)}\right]^4 - \delta_{\mathrm{y}}\, y(t) \\
\partial_t\, z(t) &= v_{\mathrm{z}} + v_{\mathrm{xz}} \left[\frac{x_{\mathrm{a}}(t)}{K_{\mathrm{xz}} + x_{\mathrm{a}}(t)}\right]^4 \frac{1}{m(t)/K_{\mathrm{nz}} + 1} - \delta_{\mathrm{yz}}\, \frac{y(t)}{K_{\mathrm{yz}} + y(t)}\, z(t) - \delta_{\mathrm{z}}\, z(t).
\end{aligned}
$$

p21 concentration is denoted by $z(t)$ and MYCN concentration by $m(t)$. We allowed for basal and p53-mediated production of p21 (rate constants v_{z} and v_{xz}, respectively) and for basal and MDM2-induced degradation of p21 (rate constants δ_{z} and δ_{yz}, respectively). MYCN $m(t)$ is inducing both inactive p53 $x_{\mathrm{i}}(t)$ and MDM2 $y(t)$ with rate constants n_1 and n_2, respectively. MYCN also inhibits the p53-mediated p21 production which is modeled by multiplying the suppressing factor

$$\frac{1}{m(t)/K_{\mathrm{nz}} + 1},$$

which goes to one for $m(t) \ll K_{\mathrm{nz}}$ and to zero for $m(t) \gg K_{\mathrm{nz}}$. We measured the protein levels of MYCN, p53, MDM2 and p21 in six neuroblastoma cell lines (three *MYCN*-amplified: SK-BE(2)C, Kelly, IMR5-75; two *MYCN*-nonamplified: SY5Y, SH-EP and one conditionally *MYCN* expressing cell line: SH-EP T21N) and asked the question whether simply the different MYCN levels and the status of p53 (mutated or wild type) can account for the observed differences. Therefore, we simulated the steady state for different cell lines with the model using the measured MYCN levels as input for $m(t)$ and setting the translation activity of p53 (rate constants v_{xy} and v_{xz}) to zero for the simulation in the SK-BE(2)C cells with mutated p53 [61, 45]. For some reason the p53 in the SH-EP cells showed a stronger activity (strong MDM2 and p21 expression). Thus, we introduced an additional factor for this cell line increasing the induction capacity of p53 (rate constants v_{xy} and v_{xz}). With this we could find a parameter set reproducing the measured protein levels for the different cell lines (figure 7.5). It remains unclear, what biological process can account for the higher activity of p53 in the SH-EP cells. The homozygous deletion of the $\mathrm{p14}^{\mathrm{ARF}}$ gene could be excluded as reason for the high MDM2 and p21 levels in the SH-EP cells, because both a clone with conditionally $\mathrm{p14}^{\mathrm{ARF}}$ knock in and model simulations with an added state for $\mathrm{p14}^{\mathrm{ARF}}$ did show a reduced MDM2 level with increasing $\mathrm{p14}^{\mathrm{ARF}}$. Note, that the level of p53 for the SK-BE(2)C cells is overestimated by the model. One possible explanation for this is a lower stability of the mutated p53. In summary, it remains plausible that the main reason for differences in protein level between this neuroblastoma cell lines is mainly attributed to their differences in MYCN protein level.

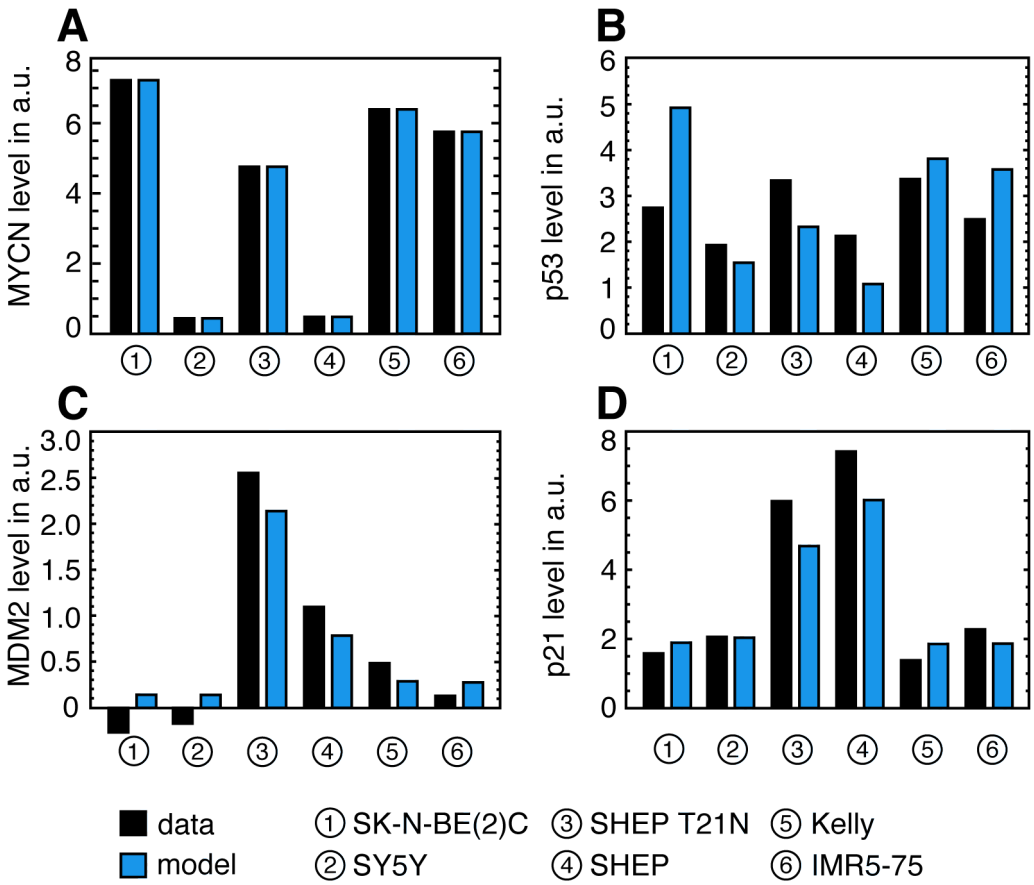

Figure 7.5: (**A**) Measurement of MYCN protein levels in six neuroblastoma cell lines (①-⑥) with *MYCN* amplification (① SK-BE(2)C, ⑤ Kelly, ⑥ IMR5-75), with wild-type *MYCN* (② SY5Y, ④ SH-EP) and with conditionally expressing *MYCN* (③ SH-EP T21N) (black bars). The MYCN level was used as input for the model (blue bars). (**B**) Measured (black bars) and simulated (blue bars) p53 level in the cell lines. (**C**) Measured (black bars) and simulated (blue bars) MDM2 level in the cell lines. p53 in the SK-BE(2)C cell line is mutated, so that the MDM2 level for ① is just determined by basal production and degradation of MDM2. The measured MDM2 and p21 level in the two SH-EP cell lines (③ and ④) is very high compared to the relatively low p53 level. To reproduce the protein levels the p53 activity in the SH-EP cells had to be increased in the simulations. (**D**) Measured (black bars) and simulated (blue bars) p21 level in the cell lines.

7.3 An extended p53-MDM2 core module qualitatively fits various measurements of responses to perturbations in neuroblastoma cell lines

To investigate the MYCN dependent response of the p53-MDM2 core module and to test our model we used time course data measured upon treatment in neurob-

lastoma cell lines. Cell culture experiments with two known chemotherapeutics affecting the p53 response were conducted. The agent doxorubicin is widely used in cancer treatment including neuroblastoma [39, 58]. It induces DNA damage by intercalating DNA and affects cell cycle arrest and apoptosis. The second agent, Nutlin-3, is a small molecule inhibitor and suppresses the binding of MDM2 to p53. It induces p53 in neuroblastoma cells and suppresses tumor growth [146, 144, 145]. Responses to Nutlin-3 and doxorubicin were measured in two different subclones of the conditionally *MYCN* expressing SH-EP T21N cell line and in the IMR5-75 cell line. In the following sections. we show, that the results in the SH-EP T21N cell lines showed a slightly different behavior and especially the p21 response varied. Notably, the mathematical model could reproduce both measurements qualitatively with different parameter sets.

7.3.1 DNA damage response of the SH-EP T21N cell line

Response to doxorubicin treatment of the SH-EP T21N cells was measured with and without MYCN induction (*MYCN*-on and *MYCN*-off, respectively) and the mathematical model including p53-MDM2 interactions, p21 and MYCN regulation was qualitatively fitted to the data (figure 7.6). Surprisingly, the measured level of p53 did not increase after DNA damage but stayed constant or decreased, whereas MDM2 was transiently upregulated. The model showed, that this behavior can be produced by a compensatory effect of increasing active p53 level and enhanced degradation of inactive p53. Measured protein levels of both p53 and MDM2 were higher in the *MYCN*-on cells compared to the *MYCN*-off cells. p21 protein levels showed a very opposing behavior. In the *MYCN*-off cells p21 was upregulated and could potentially induce cell cycle arrest. But in the cells with high *MYCN* expression, p21 was downregulated after DNA damage, indicating an impaired cell cycle arrest. The mathematical model qualitatively reproduced the kinetics for *MYCN*-off and *MYCN*-on conditions just changing the MYCN input levels. Thus, it is plausible, that the weak G1 arrest in the *MYCN*-on SH-EP cells is due to a MYCN induced protein level imbalance in the p53-MDM2 module, where the negative control of MYCN on the p53 mediated p21 activation and the increase of MDM2 is dominant over the effect of the MYCN-induced p53 protein increase.

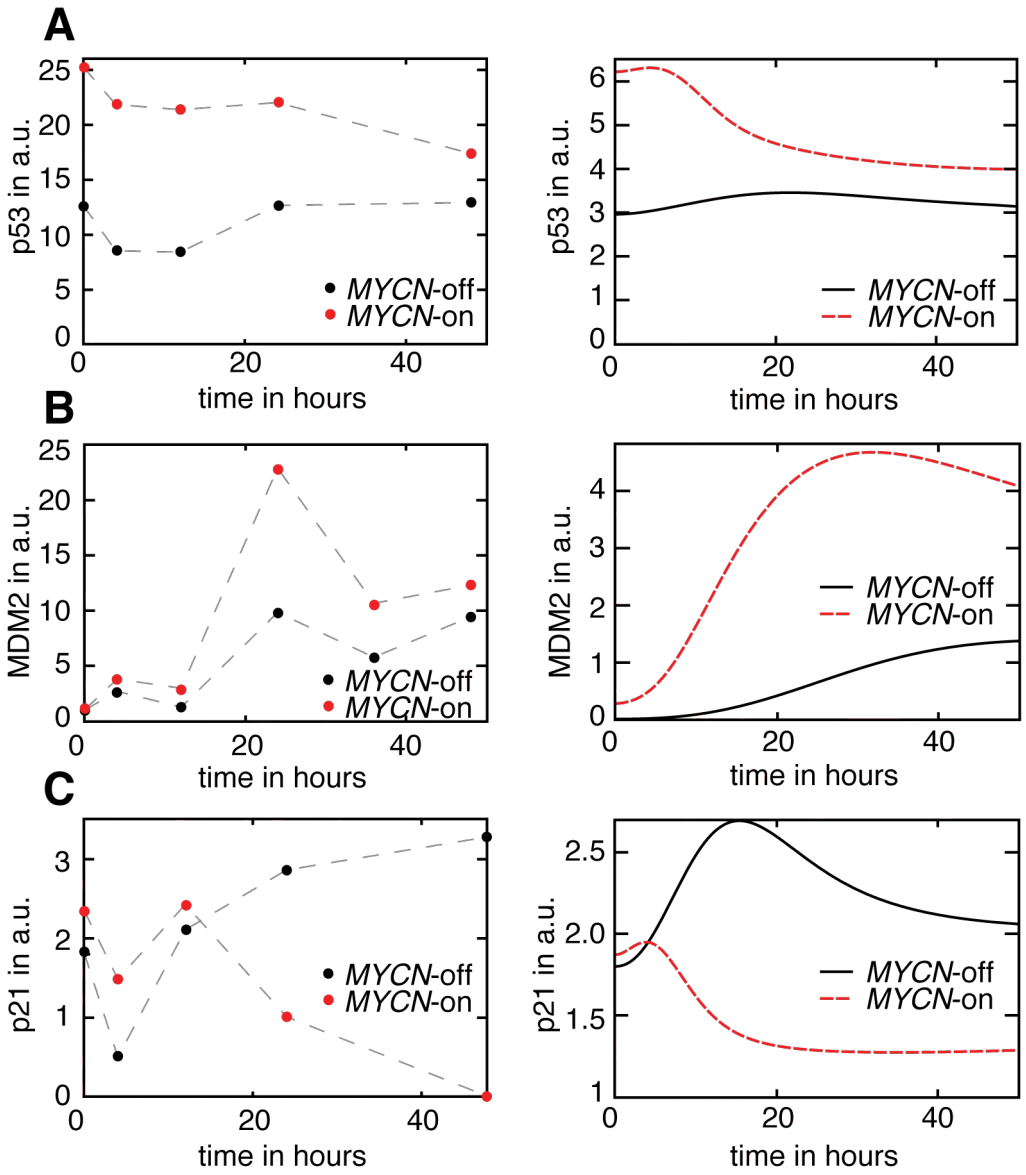

Figure 7.6: The measured proteins in the SH-EP T21N cells after doxorubicin treatment at 0 hours (left column) for *MYCN*-off (black dots) and *MYCN*-on (red dots) condition are qualitatively fitted by the corresponding model simulations (right column) with *MYCN*-off (black line) and MYCN-on (red dashed line) values. (**A**) The measured p53 level stayed constant or even decreased after doxorubicin treatment for *MYCN*-off and *MYCN*-on, respectively. The model qualitatively reproduces this behavior which can be attributed to the compensation of the increase in active p53 and the simultaneous increased degradation of inactive p53. (**B**) MDM2 measurements showed a transient increase which was much stronger if MYCN was overexpressed. The model capture the MYCN dependent differences and also showed a slight decrease at later time points, but it was not possible to generate such a strongly transient activation like the one measured. (**C**) The measured p21 levels for the *MYCN*-off cells and the *MYCN*-on cells showed opposing behavior. This could be qualitatively reproduced with the model simulations.

7.3.2 Response to DNA damage and MDM2 inhibition in the SH-EP T21N p21mCherry cell line on mRNA level

A second measurement with the SH-EP T21N p21mCherry cell line was conducted where we measured the mRNA level in *MYCN*-off cells of MDM2, p21 and of PUMA (an apoptosis related BCL-2 family protein which is a direct p53 target [165, 100]) after treatment with doxorubicin or Nutlin-3 by qRT-PCR (figure 7.7 A-C). We observed an induction of mRNA upon treatment for all three players MDM2, PUMA and p21. The measured increase of mRNA after Nutlin-3 treatment was higher than the increase after doxorubicin treatment. Remarkably, the level of MDM2 mRNA showed a decrease $\sim$ 15 hours after doxorubicin treatment which is not shared by any other measured curve. At the last time point the p21 mRNA level measured in the Nutlin-3-treated cells is the only one decreasing. To adapt the model to the measurements we added states for the mRNA concentrations of p21, p53 and MDM2 and a variable for the PUMA mRNA concentration. The PUMA mRNA concentration $w(t)$ is dependent on active p53 $x_{\mathrm{a}}(t)$ and we included basal production and degradation (rate constant v_{w} and δ_{w}, respectively)

$$\partial_t\, w(t) = v_{\mathrm{w}} + v_{\mathrm{xw}} \left[\frac{x_{\mathrm{a}}(t)}{K_{\mathrm{xw}} + x_{\mathrm{a}}(t)} \right]^4 - \delta_{\mathrm{w}}\, w(t).$$

The model equations and the best-fit parameters are given in the appendix (section A.6). The model was fitted to the mRNA data using a simulated annealing algorithm. It is capable of fitting the mRNA curves except for MDM2 for the doxorubicin treatment. The transiently downregulation of MDM2 mRNA after the first peak at $\sim$ 15 hours is not captured by the model (figure 7.7 A-C). The only process included in the model, which could account for this would be a decrease of p53 which contradicts with the increasing p21 level and the constant PUMA level. Furthermore, the model predicted correctly the measured response of p21 mRNA in the *MYCN*-on cells by enhancing the concentration of MYCN in the simulation (figure 7.7 D).

7.3.3 p53-MDM2 core module response upon DNA damage in the IMR5-75 cell line is insensitive to conditional MYCN knock down

We wanted to investigate, if the p53-MDM2 core module can also account for the DNA damage response in the IMR5-75 cell line, which harbors a *MYCN* amplification. We used a clone of the IMR5-75 cell line expressing a tetracyclin repressor-controlled MYCN siRNA to conditionally knock down MYCN. Interestingly, the response of the proteins p53 and MDM2 after doxorubicin treatment do not differ much under the two MYCN conditions (with induced siRNA and without) despite

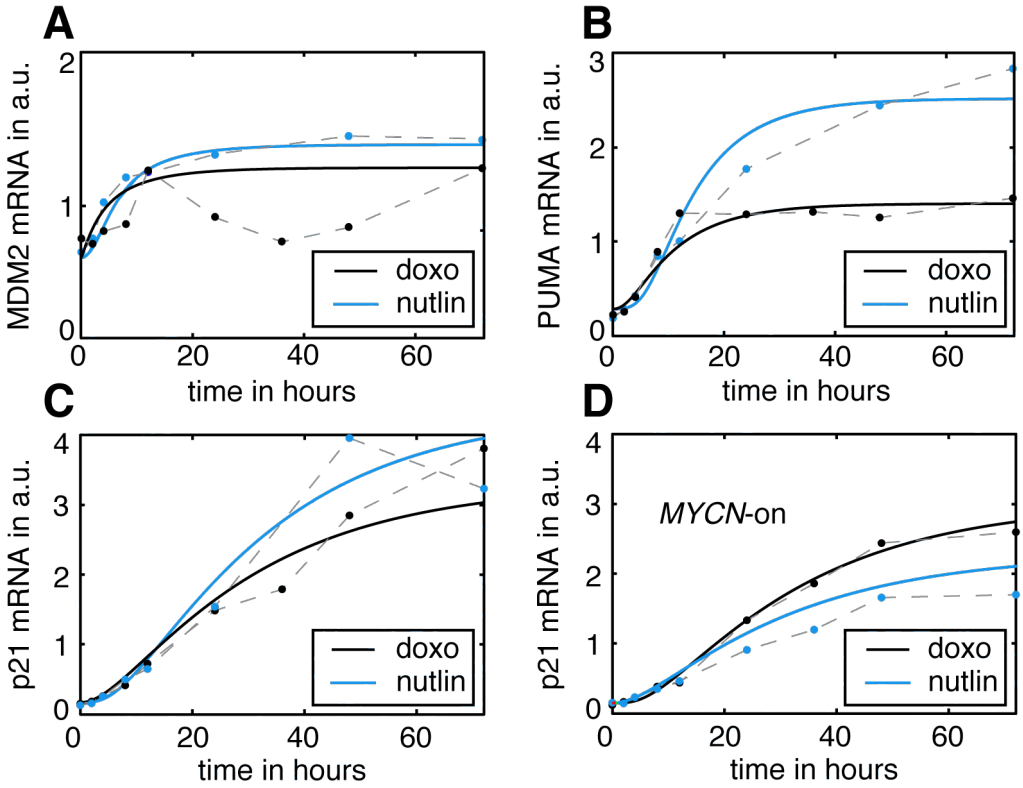

Figure 7.7: The measured mRNA levels in the SH-EP T21N p21mCherry cells after doxorubicin treatment at 0 hours (black dots) and Nutlin-3 treatment at 0 hours (blue dots) with the best-fit simulation of the mathematical model (black line for doxorubicin and blue line for Nutlin-3). For all players the induction after Nutlin-3 treatment is stronger compared to doxorubicin treatment. (**A**) It is not clear why the MDM2 level is decreasing after $\sim$ 15 hours. (**B**) PUMA mRNA level is described well by the model. (**C**) At the last timepoint p21 mRNA level for the cells treated with Nutlin-3 decreases. This is neither shared by another curve nor can the model reproduce this observation. (**D**) The model correctly predicts the response of p21 mRNA in *MYCN*-on cells to treatment with doxorubicin or Nutlin-3, which induces p21 mRNA less strongly compared to the *MYCN*-off cells in (**C**).

a MYCN knock down efficiency of $\sim$ 38% (see appendix figure A.3). Just the p21 induction changes but is unexpectedly less pronounced after MYCN knock down (figure 7.8 and Western blots appendix section A.4). The p53-MDM2 module response seems to be insensitive to a change in MYCN concentration in the IMR5-75 cell line. This may be attributed to differences in genetic and epigenetic context of the IMR5-75 and the SH-EP cell line. Another reason for the differences in cell cycle behavior might also be attributed to the high MYCN levels reached in the IMR5-75 cells under both conditions, which can result in a saturation effect of MYCN-mediated p53 and MDM2 induction. We already showed that the mathematical model of

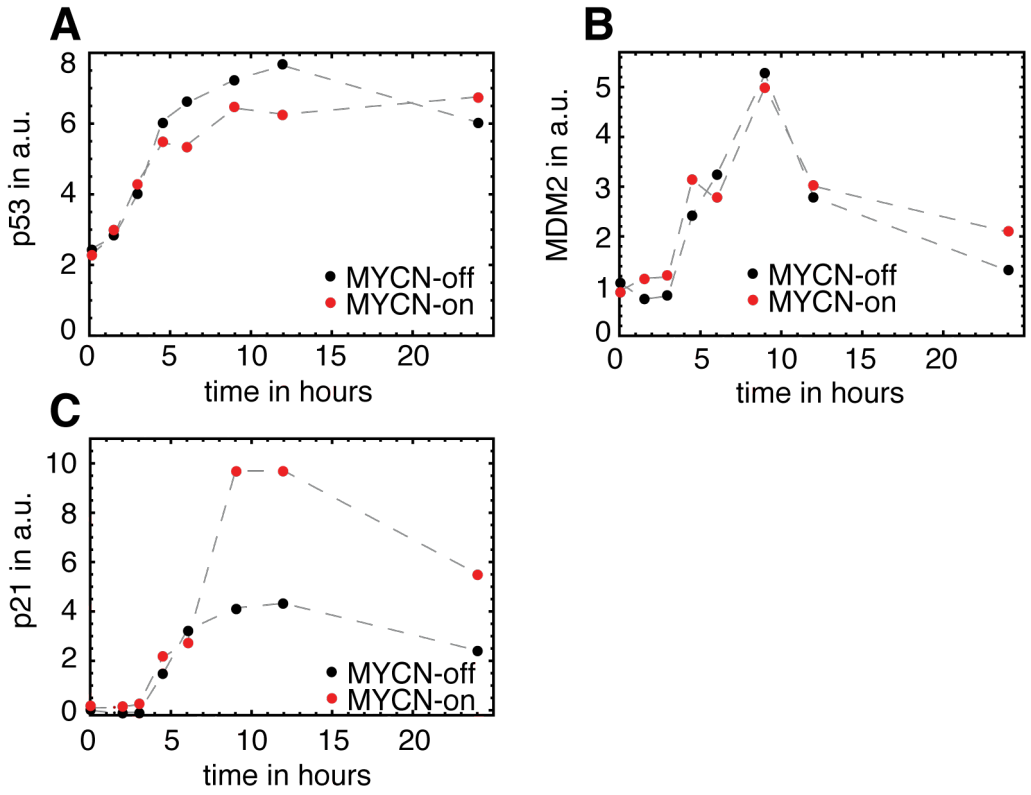

Figure 7.8: Measured protein levels in the IMR5-75 cells under MYCN-off (black dots) and MYCN-on (red dots) conditions did not show a big difference in protein levels after doxorubicin treatment at 0 hours for (**A**) p53 and (**B**) MDM2, whereas (**C**) the p21 response seemed to be decreased by MYCN knock down.

the p53-MDM2 core module is capable of reproducing the trajectories observed in the IMR5-75 cells (figure 7.4) and the increased p21 response might be due to the inhibition of the activation of the p21 promoter by MYCN. However it is found, that for high levels of MYCN the set of target genes changes and genes related to the cell cycle control become targets [122, 159, 6]. For example, the level of CDK4 decreases after knock down of MYCN in the IMR5-75 cells (Frank Westermann, private correspondence). For this reason we investigate the pRB-E2F1 axis and its interaction with MYCN in chapter 8.

8 Cell cycle model for the G1-S transition

In this chapter we introduce a mathematical model for the G1-S transition. As recent findings suggest, there is a distinct difference between the regulation of commitment to G1-S transition and the preceeding gene activation program [34]. Thus, we model the crossing of the restriction point (R-point) by investigating the regulation of the core module of E2F1-pRB regulation. The resulting bifurcation diagram can be used as a read out to analyze the effects of MYCN and protein inhibitors on the R-point theoretically and maybe in the future also experimentally. A linear model, incorporating the basic pRB-E2F1 regulation, remarkably shows bistability in spite of its noncomplexity and the absence of nonlinear terms. To account for the relevant player in neuroblastoma we extended this model and simulate the effect of network perturbations by Nutlin-3 and CDK4i treatment.

8.1 Modeling of pRB phosphorylation

Two prominent regulators of the passage from G1 to S phase (figure 8.1 A) are E2F1 and its repressor pRB (the Retinoblastoma protein) [59, 32]. The pRB-E2F1 complex recruits HDAC (histone deacetylase), where the DNA exhibits E2F1 binding sites and by histone modifications the transcription is suppressed [136]. By activity of CDKs pRB is phosphorylated and E2F1 target genes are activated [63]. pRB phosphorylation directly affects the binding affinity of E2F1 and hyperphosphorylation of pRB leads to the dissociation of the pRB-E2F1 complex [118]. The unbound E2F1 can then recruit HAT (histone acetyltransferase) proteins and activate the promoters by histone acetylation [138, 69] (figure 8.1 B). pRB is phosphorylated by the CDK4 CCN D (cyclin dependent kinase 4 and cyclin D) complex at Ser795 and the CDK2 CCNE (cyclin dependent kinase 2 and cyclin E) complex at Thr826 [23, 49, 134]. Thus, we model the inactivation of pRB as a sequential phosphorylation at two sites independent of pRB E2F1 binding, taking the time dependent concentration of pRB $R(t)$, mono-phophorylated pRB $R_{\mathrm{p}}(t)$ and double-phosphorylated pRB $R_{\mathrm{pp}}(t)$ as model states. The first phosphorylation is mediated by the CDK2 CCND complex and for the start assumed to be constant. The second phosphorylation is conducted by the CDK2-CCNE complex and modeled as linearly dependent on the CCNE concentration $C(t)$ (figure 8.2 A), starting with the assumption that CDK2 is relatively constant and present in excess. Experiments in neuroblastoma cell lines indicated that the total amount of pRB is constant on the relevant timescale $R_{\mathrm{tot}}(t) = \mathrm{const.}$

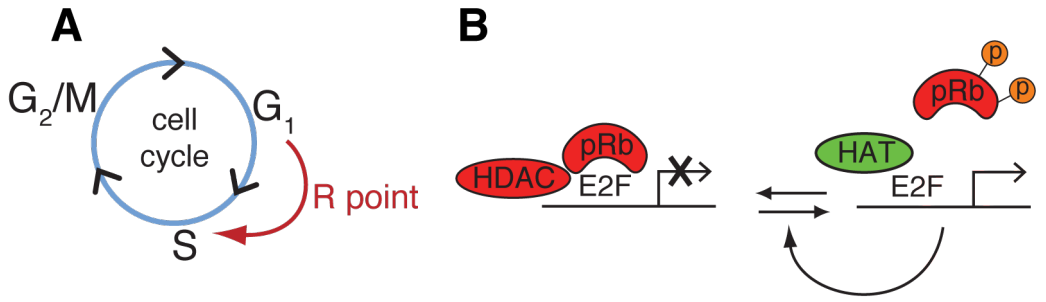

Figure 8.1: (**A**) At the G1-S transition the cell crosses the R-point and initiates cell division independently from external growth factors. The E2F1 protein is one major regulator at this point of the cell cycle and was shown to be part of a bistable switch. (**B**) The E2F1 pRB complex recruits HDAC and the E2F1 target genes are inactivated. pRB hyperphosphorylation leads to dissociation of the E2F1 pRB complex and allows HAT to bind and to activate the promoter by histon acetylation. The active E2F1 exerts a positive feedback on its own activation by several channels (e.g. autoinduction by E2F1, induction of SKP2, induction of CCNE).

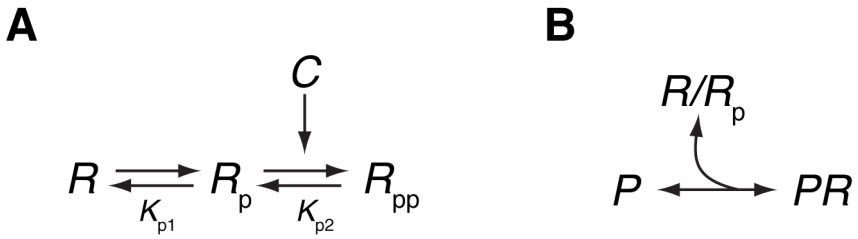

Figure 8.2: (**A**) pRB phosphorylation is modeled as two sequential steps, with the dissociation constants for mono and double phosphorylation K_{p1} and K_{p2}, respectively. The second phosphorylation is dependent on the CCNE concentration $C(t)$. (**B**) pRB binding regulates the promoter activity.

Assuming, that the pRB phosphorylation is independent of its binding to E2F1 we get for the steady states (steady state is indicated by omitting the argument $R(t \to \infty) = R$)

$$
\begin{aligned}
R_{\mathrm{p}} &= \frac{1}{K_{\mathrm{p1}}}\, R = \frac{1}{K_{\mathrm{p1}}}\,(R_{\mathrm{tot}} - R_{\mathrm{p}} - R_{\mathrm{pp}}) \\
R_{\mathrm{pp}} &= \frac{1}{K_{\mathrm{p2}}}\, C\, R_{\mathrm{p}} \\
R_{\mathrm{tot}} &= R + R_{\mathrm{p}} + R_{\mathrm{pp}},
\end{aligned}
$$

where K_{p1} and K_{p2} are the dissociation constants for the first and the second phosphorylation step, respectively. This yields the concentration of double-phosphorylated pRB R_{pp} just dependent on the CCNE concentration C and the constants R_{tot}, K_{p1} and K_{p2}

$$R_{\mathrm{pp}}(C, R_{\mathrm{tot}}, K_{\mathrm{p1}}, K_{\mathrm{p2}}) = \frac{C R_{\mathrm{tot}}}{C + K_{\mathrm{p2}} + K_{\mathrm{p1}} K_{\mathrm{p2}}}. \tag{8.1}$$

8.2 A noncomplex model of the pRB-E2F1 regulation exhibits bistability

We wanted to investigate if a model incorporating just the most prominent interactions can account for the behavior of E2F1 at the G1-S transition. To model the transcriptional activity of E2F1 at the G1-S transition we considered a simple regulatory model of promoter activation. The model consists of two states that describe the E2F1 regulated promoter activities. Promoters can be either inactive when both E2F1 and pRB ar bound $PR(t)$ or active being bound only by E2F1 P(t) (figure 8.2 B). The binding of pRB to the E2F1 promoter complex is dependent on its phosphorylation (double-phophorylated pRB cannot bind). The amount of pRB binding in steady state is given by the dissociation constant K_{R} of its binding to the E2F1 promoter complex and the amount of free (not double-phosphorylated) pRB R_{free}

$$\begin{aligned} PR &= \frac{1}{K_{\mathrm{R}}}\ P\ R_{\mathrm{free}} \\ P_{\mathrm{tot}} &= P + PR \\ R_{\mathrm{free}} &= R_{\mathrm{tot}} - PR - R_{\mathrm{pp}}, \end{aligned}$$

where the total number of promoters P_{tot} is set constant. Combining the three equations by inserting the second and the third line into the first, we get the equation for the steady state of the active promoters P

$$P_{\mathrm{tot}} - P = \frac{1}{K_{\mathrm{R}}}\ P\ \left(R_{\mathrm{tot}} - (P_{\mathrm{tot}} - P) - R_{\mathrm{pp}}\right). \tag{8.2}$$

Note that R_{pp} is dependent on the CCNE concentration (equation 8.1). So the explicit solution for P reads

$$
\begin{aligned}
2P &= -K_{\mathrm{R}} + P_{\mathrm{tot}} - R_{\mathrm{tot}} + \frac{CR_{\mathrm{tot}}}{C + K_{\mathrm{p2}} + K_{\mathrm{p1}}K_{\mathrm{p2}}} \\
&\quad + \sqrt{4K_{\mathrm{R}}P_{\mathrm{tot}} + \left(K_{\mathrm{R}} - P_{\mathrm{tot}} + \frac{(1+K_{\mathrm{p1}})K_{\mathrm{p2}}R_{\mathrm{tot}}}{C + K_{\mathrm{p2}} + K_{\mathrm{p1}}K_{\mathrm{p2}}}\right)^2}
\end{aligned} \tag{8.3}
$$

To implement the positive feedback via E2F1-induced CCNE transcription we model the CCNE concentration $C(t)$ as being dependent on the active promoters $P(t)$

$$
\partial_t C(t) = \nu P(t) - \delta C(t) \tag{8.4}
$$

where ν is the strength of CCNE induction and δ is the basal degradation rate constant of CCNE.

Interestingly, this simple model already exhibits bistability for a certain parameter space (figure 8.3). This means $\partial_t C(t)$ has two stable roots. To calculate the bistable

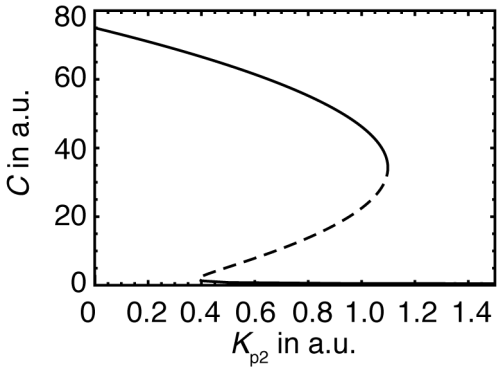

Figure 8.3: Bifurcation diagram: the non-complex model exhibits bistability. Here the bistability parameter is K_{p2} the dissociation constant of the pRB phosphorylation via cyclin E. The other parameters in arbitrary units are $P_{\mathrm{tot}} = 1$, $R_{\mathrm{tot}} = 10$ and $K_{\mathrm{R}} = 0.05$, $K_{\mathrm{p1}} = 1$; $\nu = 150$ and $\delta = 2$.

regime we can now use the expression for P from equation 8.3, inserting this into the equation for CCNE (equation 8.4) and solve for $\partial_C^2 P(C) = 0$. Unfortunately this is analytically not feasible. However, it is possible to understand qualitatively by what mechanism the bistability of the system arises. $\partial_t C$ has two stable roots, if the promoters as function of C ($P(C)$) behaves sigmoidal. $P(C)$ is the combination of the functions $P(R_{\mathrm{pp}})$ and $R_{\mathrm{pp}}(C)$ (figure 8.4 A & B). Thus, to get a sigmoidal behavior the amount of active promoters has to be sensitive to the concentration of

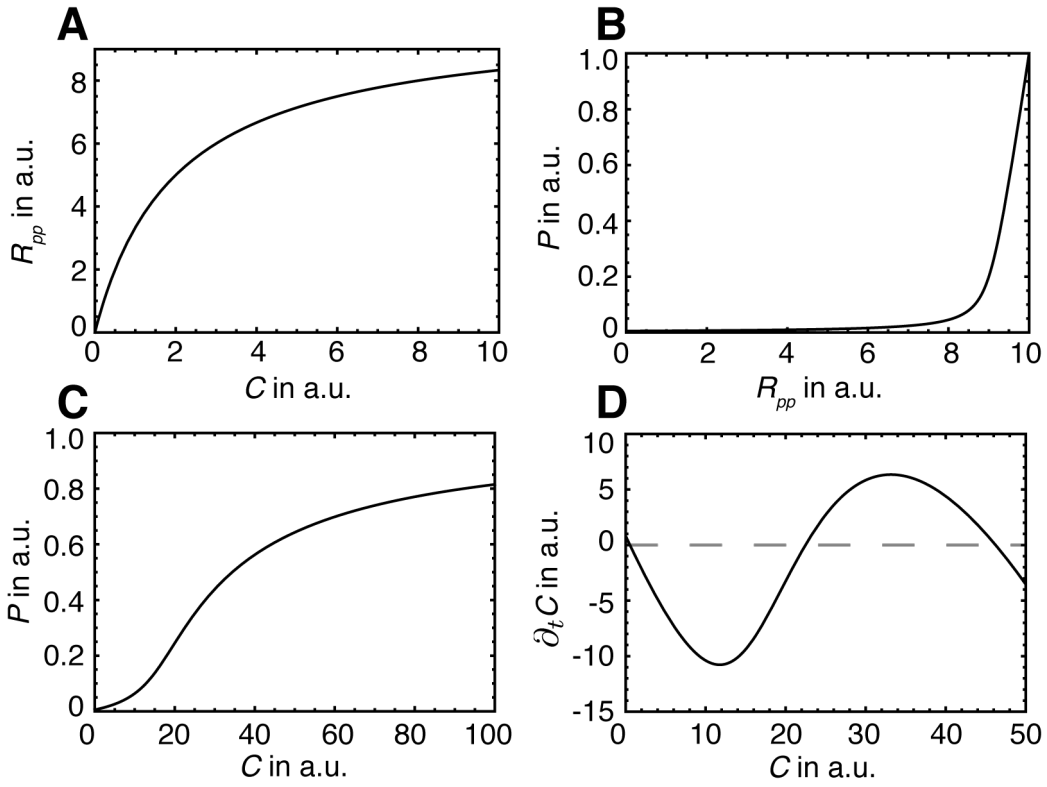

Figure 8.4: (**A**) Double-phosphorylated pRB R_{pp} as function of the CCNE concentration C combined with (**B**) the active promoters P as function on the concentration of double-phosphorylated pRB R_{pp}. Is P highly sensitive on R_{pp} and in this 'sensitivity range' also $R_{\mathrm{pp}}(C)$ not too flat (**C**) $P(C)$ can be sigmoidal. (**D**) For a sigmoidal shape of $P(C)$, there can exist two stable roots of $\partial_t C$, which means that the system is bistable. Both curves were simulated with the following parameter values in arbitrary units: total promoter concentration $P_{\mathrm{tot}} = 1$, total pRB concentration $R_{\mathrm{tot}} = 10$ and dissociation constant of pRB binding to the E2F1 promoter complex $K_{\mathrm{R}} = 0.05$; dissociation constants of pRB phosphorylation $K_{\mathrm{p1}} = K_{\mathrm{p2}} = 1$, induction rate constant of CCNE by the active promoters $\nu = 150$ and degradation rate constant of CCNE $\delta = 2$.

phophorylated pRB and with that to the CCNE concentration. If the pRB binding to the E2f1 promoter complex is very stong and the amount of pRB is higher than the number of binding sites

$$\begin{aligned} R_{\mathrm{tot}} &> P_{\mathrm{tot}} \\ K_{\mathrm{R}} &\ll R_{\mathrm{tot}} - P_{\mathrm{tot}} \end{aligned}$$

the promoters are mostly inactive (bound pRB) for a wide range of pRB phosphorylation. Just if the phosphorylation is strong enough to deplete the pRB so

strongly that the available unphosphorylated pRB is of the order of the promoters $R_{\text{free}} \sim P_{\text{tot}}$ the active promoters increase steeply with the pRB phosphorylation. If also $R_{\text{pp}}(C)$ is tuned accordingly (not too sharp) $P(R_{\text{pp}})$ becomes sigmoidal and $\partial_t C$ has two roots (figure 8.4 C & D). Conclusively, if strong binding of pRB to the E2F1 promoter complex is combined with a strong abundance of pRB this linear system can have a highly sensitive response to concentration changes, which in this case generates bistability (figure 8.3).

8.3 E2F1 regulation in the model

To rationalize the regulatory impact free E2F1 has on the system behavior we include the concentration of E2F1 $E(t)$ and its regulation into the model (figure 8.5). We show that in a certain range the model does not change and that E2F1 autoactivation enhances the bistable regime. We distinguish three promotor states: naked

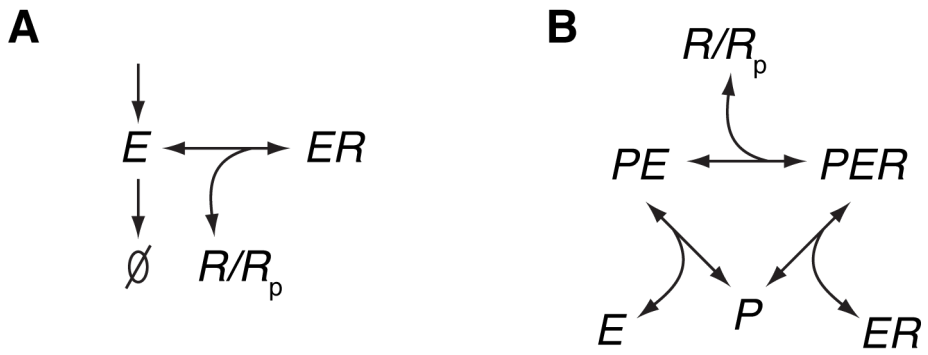

Figure 8.5: (**A**) E2F1 regulation is introduced into the mathematical model with basal production and degradation. (**B**) Additionally E2F1 can bind to the promoter P and to pRB R or mono-phosphorylated pRB R_{p} both in solution and at the promoter PER.

promoter $P(t)$, E2F1 promoter complex $PE(t)$ and pRB bound E2F1 promoter complex $PER(t)$. pRB can bind with E2F1 both at the promoter and in solution. The steady state equations are

$$
\begin{aligned}
PER &= \frac{1}{K_{\mathrm{R}}}\, PE\; R_{\mathrm{free}} \\
ER &= \frac{1}{K_{\mathrm{R}}}\, E\; R_{\mathrm{free}} \\
PE &= \frac{1}{K_{\mathrm{E}}}\, E\; P \\
R_{\mathrm{free}} &= R_{\mathrm{tot}} - PER - ER - R_{\mathrm{pp}} \\
P_{\mathrm{tot}} &= P + PE + PER, \qquad (8.5)
\end{aligned}
$$

with K_{E} the dissociation constant for E2F1 binding at the promoter ($E + P \leftrightarrow PE$). First we want to model E2F1 without regulation to investigate the effect of E2F1 binding to the promoter has on the system. Thus, we included basal E2F1 production (rate constant ν_{E}) and degradation (rate constant δ_{E})

$$\partial_t\, E(t) = \nu_{\mathrm{E}} - \delta_{\mathrm{E}}\; E(t) + \text{binding reactions to pRB and promoter.}$$

Assuming that E2F1 is not degraded while bound by either pRB or DNA we get for the steady state of unbound E2F1

$$E = \frac{\nu_{\mathrm{E}}}{\delta_{\mathrm{E}}}.$$

Inserting this into the steady state equations 8.5 we get

$$ER = \frac{1}{1 + K_{\mathrm{R}}\delta_{\mathrm{E}}/\nu_{\mathrm{E}}}\left(R_{\mathrm{tot}} - PER - R_{\mathrm{pp}}\right),$$

which yields

$$
\begin{aligned}
PER &= \frac{1}{K_{\mathrm{R}}}\,(1 - A)\, PE\,(R_{\mathrm{tot}} - PER - R_{\mathrm{pp}}) \\
PER &= P_{\mathrm{tot}} - (1 + B)\, PE,
\end{aligned}
$$

with

$$\begin{aligned} 1 - A &= \frac{1}{1 + \nu_{\mathrm{E}}/(K_{\mathrm{R}}\delta_{\mathrm{E}})} \\ B &= \frac{K_{\mathrm{E}}\ \delta_{\mathrm{E}}}{\nu_{\mathrm{E}}}. \end{aligned}$$

Combining these two equations yields an expression for the active promoters (here PE) similar to equation 8.2 for the active promoters in the model not considering E2F1 explicitly (in this case P) .

$$P_{\mathrm{tot}} - (1 + B)\, PE = \frac{1}{K_{\mathrm{R}}}\,(1 - A)\ \ P\ \ (R_{\mathrm{tot}} - (P_{\mathrm{tot}} - (1 + B)\, PE) - R_{\mathrm{pp}})\,. \quad (8.6)$$

$$\left[\text{model without E2F1 regulation}: P_{\mathrm{tot}} - P = \frac{1}{K_{\mathrm{R}}}\ P\ \ (R_{\mathrm{tot}} - (P_{\mathrm{tot}} - P) - R_{\mathrm{pp}})\right]$$

Let K_{R}^{*} be the value of the dissociation constant in the first model and P_{tot}^{*} be the concentration of the promoters. If for the dissociation constant for pRB binding K_{R} and the promoter concentration P_{tot} in equation 8.6 holds

$$\begin{aligned} K_{\mathrm{R}}^{*} &= \frac{1}{K_{\mathrm{R}}}\,(1 - A) \\ \Leftrightarrow K_{\mathrm{R}} &= K_{\mathrm{R}}^{*} - \frac{v_{\mathrm{E}}}{\delta_{\mathrm{E}}} \\ P_{\mathrm{tot}} &= P_{\mathrm{tot}}^{*}\,(1 + B)\,, \end{aligned}$$

then equation 8.6 and 8.2 become identical for $B \ll 1$. This means for excess of E2F1 $K_{\mathrm{E}} \ll E$ the model including E2F1 explicitly can be mapped to the model with just the two state E2F1 promoter complex. Consequently, for a large E2F1 pool the concentration change due to promoter or pRB binding can be neglected and the system is described by the simpler model.

Including E2F dependency on active promoters $\partial_t E(t) = \nu_{\mathrm{E}} + \nu_{\mathrm{PE}}\ PE(t) - \delta_{\mathrm{E}} E(t)$ enhances the positive feedback and enlarges the region where bifurcation occurs (figure 8.6).

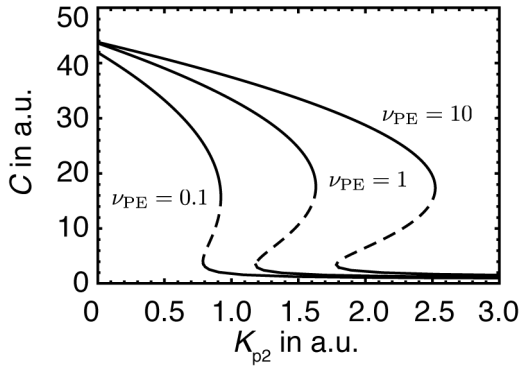

Figure 8.6: For increased autoactivation of E2F1 (rate constant v_{PE}) the region were the system is bistable is enlarged due to the additional positive feedback loop.

8.4 Additional feedback: CDK2/CCNE, SKP2 and p27 regulation increase the bistable behavior

Another positive feedback loop of E2F1 is via SKP2 which is a transcriptional target of E2F1 (figure8.7) and has been found to be upregulated in many tumors [7] and in neuroblastoma [98, 158]. SKP2 acts as a E3 ligase on phosphorylated p27 [19], which inhibits CDK2 activity by binding to the CDK2 CCNE complex. Thus, p27 degradation activates CDK2 CCNE complexes by freeing them from the inhibitory p27 binding. Activ CDK2 in turn can phosphorylate p27 which marks it as a target

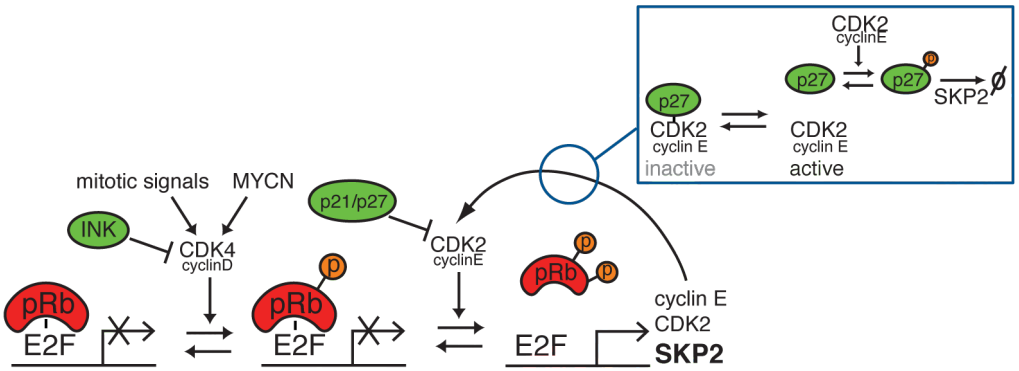

Figure 8.7: Network model of the E2F1 pRB regulation and the feedback loop via SKP2. SKP2 tags p27 for proteosomal degradation and with that activates CDK2 CCNE complex. For this previous p27 phosphorylation is necessary which is in turn mediated by CDK2.

for SKP2. By this a positive feedback loop is formed. To include the SKP2 relevant regulation we implemented the mentioned processes in our model. The differential

equation system for the additional CDK2 regulation via SKP2 $s(t)$ (figure 8.8) reads

$$\begin{aligned}
\partial_t\, w(t) &= v - k_\mathrm{c}\, w(t)\, C_\mathrm{f}(t) + l_\mathrm{c}\, C_\mathrm{b}(t) - k_\mathrm{p}\, w(t)\, C_\mathrm{f}(t) + l_\mathrm{p}\, w_\mathrm{p}(t) - \delta\, w(t) \\
\partial_t\, w_\mathrm{p}(t) &= -k_\mathrm{c}\, w_\mathrm{p}(t)\, C_\mathrm{f}(t) + l_\mathrm{c}\, C_\mathrm{b}^\mathrm{p}(t) + k_\mathrm{p}\, w(t)\, C_\mathrm{f}(t) - (l_\mathrm{p} + \delta + \delta^*\, s(t))\; w_\mathrm{p}(t) \\
\partial_t\, C_\mathrm{f}(t) &= -k_\mathrm{c}\, w(t)\, C_\mathrm{f}(t) + l_\mathrm{c}\, C_\mathrm{b}(t) - k_\mathrm{c}\, w_\mathrm{p}(t)\, C_\mathrm{f}(t) + l_\mathrm{c}\, C_\mathrm{b}^\mathrm{p}(t) \\
\partial_t\, C_\mathrm{b}(t) &= k_\mathrm{c}\, w(t)\, C_\mathrm{f}(t) - l_\mathrm{c}\, C_\mathrm{b}(t) - k_\mathrm{p}\, C_\mathrm{b}(t)\, C_\mathrm{f}(t) + l_\mathrm{p}\, C_\mathrm{b}^\mathrm{p}(t) \\
\partial_t\, C_\mathrm{b}^\mathrm{p}(t) &= k_\mathrm{c}\, w_\mathrm{p}(t)\, C_\mathrm{f}(t) - l_\mathrm{c}\, C_\mathrm{b}^\mathrm{p}(t) + k_\mathrm{p}\, C_\mathrm{b}(t)\, C_\mathrm{f}(t) - l_\mathrm{p}\, C_\mathrm{b}^\mathrm{p}(t)
\end{aligned}$$

with the concentration of unbound p27 unphosphorylated $w(t)$, phosphorylated $w_\mathrm{p}(t)$ and total $w_\mathrm{tot}(t)$; concentration of free CDK2 $C_\mathrm{f}(t)$, bound with unphosphorylated p27 $C_\mathrm{b}(t)$, bound with phosphorylated p27 $C_\mathrm{b}^\mathrm{p}(t)$ and total C_tot. The

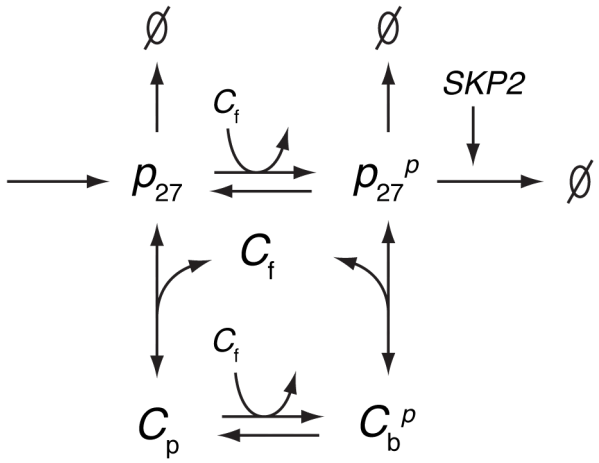

Figure 8.8: We modeled CDK2 CCNE complex-mediated p27 phosphorylation and subsequent SKP2-dependent degradation, CDK2 CCNE complex binding to p27 (both to phosphorylated and unphosphorylated) and allowed for p27 phosphorylation while bound to a CDK2 CCNE complex.

autoactivation of CDK2 via p27 phosphorylation produces a high sensitivity of the free CDK2 on the concentration of SKP2 (figure 8.9). This enhances the bistable behavior of the system by sensitizing the E2F1 response to input signals (e.g. stronger pRB phosphorylation by growth factor induced CCND) and strengthen the positive feedback of E2F1 via CDK2 and CCNE. The model is bistable in a wide parameter range and can be utilized to rationalize the effect of network perturbations.

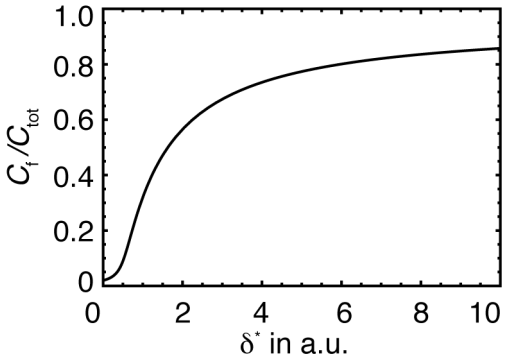

Figure 8.9: The positive feedback that the active CDK2 CCNE complex exerts on its own activation leads to a high sensitivity of the CDK2 CCNE complex to the SKP2 concentration (modeled as a change in the SKP2-mediated p27 degradation rate constant δ^*). On the one hand the SKP2 concentration is E2F1 dependent and on the other hand more active CDK2 CCNE complex increases pRB phosphorylation. Thus, this high sensitivity can potentially enforce the bistable behavior.

8.5 Cell cycle arrest induction by a combination of Nutlin-3 and CDK4i is synergistic but strongly impaired by amplified MYCN

Using the derived mathematical model we next simulated different perturbations of the network to investigate its impact on the R-point behavior. To model the specific treatments we included a term for CDK4 level and a term for p21 level in the equation for pRB phosphorylation. The full equation system with the used parameter values is given in the appendix (section A.7). The MYCN gene amplification leads to an increase in CDK4 level as MYCN is a transcription factor for CDK4 [6]. Increasing the level of CDK4 in the model shifts the bifurcation curve to the right and lessens the region of bistability (figure 8.10). Conclusively, the *MYCN*-on cells would need less or even no growth signals to commit to cell cycle progression, corresponding to strong proliferation and uncontrolled G1-S transition. This growth factor independence is in line with experiments, where cells are synchronized by growth factor starvation. In these experiments *MYCN*-amplified cells such as IMR5-75 cells do not arrest (Frank Westermann, private correspondence).

Experiments with the small molecule inhibitor Nutlin-3 and a CDK4 inhibitor (CDK4i) in conditionally MYCN expressing IMR5-75 cells showed that a treatment with both inhibitors exhibited a synergistic inhibitory effect on cell growth [157]. Here CDK4i treatment was modeled by reducing the CDK4 level to 20%. The Nutlin-3 treatment is inducing p21 protein by inhibiting the interaction of MDM2 and p53 (see section 7). CDK2-CCNE complexes are inactivated by binding to this

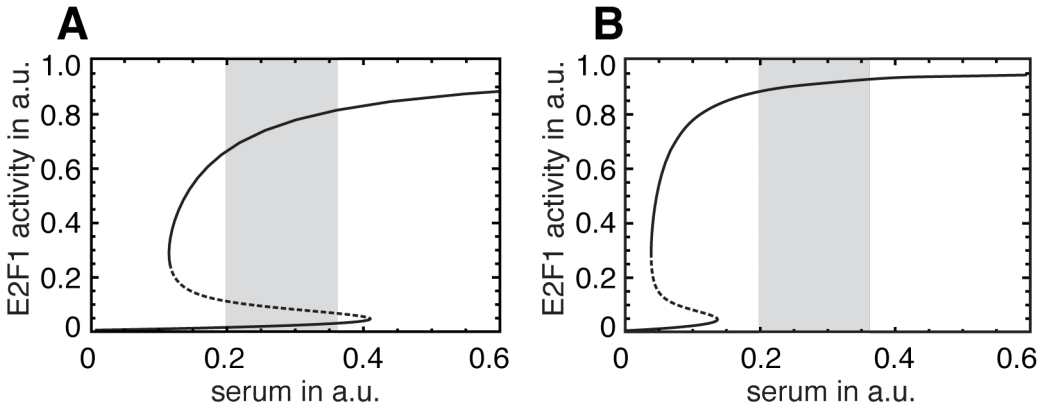

Figure 8.10: (**A**) The bifurcation diagram for a simulation with low MYCN level. The E2F1 activity is measured by the fraction of the promoter in the state where just E2F1 is bound (*PE*). (**B**) The bistable region is shifted to lower serum concentrations (corresponding to lower concentration of growth factors) for a simulation with high MYCN levels.

p21 and thereby further pRB phosphorylation is suppressed. To investigate how the system behaves under change of p21 or CDK4 levels we plotted the bifurcation points as function of p21 and CDK4 concentrations (figure 8.11 A). For high CDK4 levels and low p21 levels bistability is lost and just the high steady state exists. This would mean growth factor independent proliferation. For low MYCN levels and high p21 levels just the lower steady state exists, corresponding to G1 cell cycle arrest. In between, near the diagonal lies the bistable region. Conclusively, from a malignant state (high CDK4, low p21) it is most effective to reach the bistable region or the lower steady state by simultaneously reducing CDK4 (e.g. by CDK4i) and increasing p21 (e.g. Nutlin treatment). However, by analyzing the change of the bifurcation points under Nutlin-3 and CDK4i the simulations showed that the effect of Nutlin-3 and CDK4i in the *MYCN*-amplified cells is significantly reduced compared to the *MYCN*-nonamplified cells. Treatment of *MYCN*-off cells just with Nutlin-3 is much more effective than treatment of *MYCN*-on cells with a combination of Nutlin-3 and CDK4i. We plotted the change of the value of the first bifurcation point (the point, after which just the steady state with high E2F1 exists) for the simulations with Nutlin and CDK4i at *MYCN*-on and *MYCN*-off conditions (figure 8.11 B). Simulation of the Nutlin-3 treatment in *MYCN*-nonamplified cells strongly shifted the bifurcation point to the right corresponding to cell cycle arrest despite growth factor access. Increasing the MYCN level in the model reduces the simulated effect of both Nutlin-3 and CDK4i significantly. In an exemplary simulation the combination of both inhibitor could just compensate for the MYCN effect and restore the 'wild type' behavior without inducing additional cell cycle arrest (figure 8.11 B). In summary, the bifurcation diagram of the mathematical model could be used to rationalize MYCN-dependent treatment effects on the system. Although the

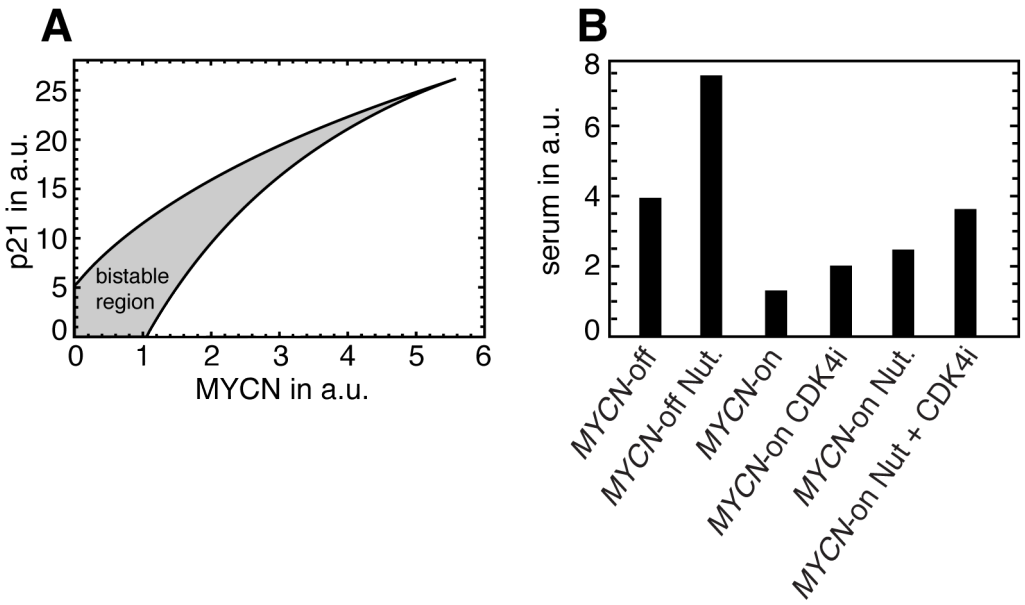

Figure 8.11: (**A**) The bistable regime as function of MYCN and p21 has a diagonal shape. Consequently combined counteracting of MYCN effect and induction of p21 is most effective. (**B**) The simulated value of the bifurcation point as function of serum shows that simulated treatment of *MYCN*-off cells just with Nutlin-3 is much more effective than treatment of *MYCN*-on cells with a combination of Nutlin-3 and CDK4i. The *MYCN*-on cells upon combined treatment just reach the simulated value for the bifurcation point of the untreated *MYCN*-off cells.

model only consists of few interactions, treatments that do not directly affect these players can be modeled by considering the downstream effects of the treatments.

9 Age structured cell cycle model

In this chapter a phenomenological model of the cell cycle is introduced. It is shown that by calculation of underlying steady age distributions, cell phase lengths and apoptosis probabilities can be deduced from DNA content FACS measurements in combination with additional information as the cell groth rate using only few assumptions.

9.1 Steady age distributions for the cell cycle

We describe a growing cell population with number of cells $n_i(a,t)$ in dependence of time t and age a in a certain phase i based on the McKendrick-van Foerster equation [89, 153]. For simplicity we start by considering just one phase (total cell cycle). $n(a,t)$ should fulfill

$$\partial_t\, n(a,t) + \partial_a\, n(a,t) = -k(a)\, n(a,t), \tag{9.1}$$

were the age dependent rate $k(a)$ accounts for cells leaving the system (e.g. mitosis, cell death, senescence). If a cell divides at age a and leaves the system, two 'new' cells enter with age zero. Let cells divide with rate $k(a)$ then one of the boundary conditions is

$$n(0,t) = 2\int_0^\infty n(a,t)\, k(a)\, da.$$

Assuming that the population is growing exponentially and that all cells divide at some time, there exist a steady age distribution $s(a)$ and a constant λ such that

$$n(a,t) = N_0\, s(a)\, e^{\lambda t}, \tag{9.2}$$

with the normalization

$$\int_0^\infty s(a)\, da = 1.$$

The second boundary condition, demanding that the population is in steady age at time zero with initial number of cells N_0 reads

$$n(a,0) = N_0\, s(a).$$

Inserting equation 9.2 into equation 9.1 gives a differential equation for the steady age distribution

$$\partial_a\, s(a) = -\left(k(a) + \lambda\right) s(a)$$

with solution

$$s(a) = s(0) \exp\left\{-\lambda a - \int_0^a k(a^*)\, da^*\right\} \tag{9.3}$$

and from the normalization

$$s(0) = \left[\int_0^\infty \exp\left\{-\lambda a - \int_0^a k(a^*)\, da^*\right\} da\right]^{-1}.$$

9.2 Steady age distribution for multiple phases

The extension of the model for describing the cell cycle with multiple phases is quite straight forward by considering the number of cells $n_i(a,t)$ at time t with age a in phase i. Because every phase gets input from the previous phase and the first phase of the cell cycle get two cells for every cell leaving the last phase of the cell cycle, we introduce as index set for the phases a cyclic set $I = \{1, 2, \ldots, D\}$ with number of elements D equal to the number of cell cycle phases to be described (for a cyclic set addition is defined as addition modulo the cardinal number so that $D + 1 = 1$). Then we can generalize equation 9.1 and its boundary conditions to

$$\begin{aligned}
\partial_t\, n_i(a,t) + \partial_a\, n_i(a,t) &= -k_i(a)\, n_i(a,t) \\
n_{i+1}(0,t) &= \xi_{i+1} \int_0^\infty n_i(a,t)\, k_i(a)\, da \\
n_i(a,0) &= N_{0,i}\, s_i(a),
\end{aligned} \tag{9.4}$$

with $i \in I$, $\xi_i = 2$ for $i = 1$ and $\xi_i = 1$ else and steady age distributions of the phases $s_i(a)$. Similarly to the one phase model equation 9.3 the steady age distributions $s_i(a)$ in a multi phase model are given by

$$\begin{aligned}
s_i(a) &= s_i(0) \exp\left\{-\lambda a - \int_0^a k_i(a^*)\, da^*\right\} \\
s_i(0) &= \left[\int_0^\infty \exp\left\{-\lambda a - \int_0^a k_i(a^*)\, da^*\right\} da\right]^{-1}.
\end{aligned}$$

Combining this, we get

$$\begin{aligned} n_{i+1}(0,t) &= N_{0,i+1}\, e^{\lambda t}\, s_{i+1}(0) \\ &= N_{0,i}\, e^{\lambda t}\, s_i(0)\, \xi_{i+1} \int_0^\infty e^{-\lambda a - \int_0^a k_i(a^*)\, da^*}\, k_i(a) da. \end{aligned} \tag{9.5}$$

By dividing the equation by the total number of initial cells N_0 we get an equation system for the fraction of cells in a certain phase

$$u_i = \frac{N_{0,i}}{N_0},$$

dependent on the rates $k_i(a)$ and the rate of cell growth λ. Instead of the age dependent rate $k(a)$ usually the distributions of transition times are measured. Thus, we want to use probability density functions (pdfs) instead of the age dependent rates. Fortunately it is possible to calculate the age dependent rates directly from the pdf. The transition rate $k(a)$ is defined via

$$k(a) = -\frac{dn(a,t)}{da}\frac{1}{n(a,t)}.$$

Let $\pi(a)$ be the pdf for the transition (in units of one over time) then the derivative is

$$\frac{dn(a,t)}{da} = -\pi(a) n(0, t-a)$$

by definition and the amount of cells at age a left is

$$n(a,t) = \left(1 - \int_0^a \pi(a^*)\, da^*\right)\, n(0,t-a) = (1 - \chi(\pi(a)))\; n(0,t-a),$$

with the cumulative probability distribution (cdf) $\chi(\pi(a))$. Inserting this into the definition of $k(a)$ yields

$$k(a) = -\frac{dn(a,t)}{da}\frac{1}{n(a,t)} = \frac{\pi(a)\, n(0,t-a)}{(1-\chi(a))\; n(0,t-a)} = \frac{\pi(a)}{1-\chi(\pi(a))}. \tag{9.6}$$

So we can convert a pdf via equation 9.6 into the rate. The steady age distribution for the whole cell cycle can be calculated straight forward from the multiple phase description. The pdf for the division π_{whole} is the convolution of the pdfs from the single phases π_i

$$\pi_{\text{whole}}(a) = \pi_1(a) \circ \pi_2(a) \circ \ldots \circ \pi_D(a).$$

From this it follows that the mean μ_{whole} and the variance σ^2_{whole} are the sum of the means μ_i and variances σ_i^2 of the multiple phases (which is true for all cumulants)

$$\begin{aligned} \mu_{\text{whole}} &= \sum_{i \in I} \mu_i \\ \sigma^2_{\text{whole}} &= \sum_{i \in I} \sigma_i^2. \end{aligned} \tag{9.7}$$

The measured cell cycle length distribution is often skewed to the right. Note, that the convolution reduces the skew which is not a cumulant and the skewness of the single phases (or at least from one single phase) has to be stronger than the skewness of the resulting distribution.

9.2.1 Simple case without cell death and sharp phase transition gives exponential steady age distribution

The simplest assumption for the model is a fixed cell cycle length Λ. Then the division rate is described by a Dirac delta distribution $k(a) = \delta(a - \Lambda)$ and it follows that

$$s(a) = s(0)\, e^{-\lambda a} \text{ for } a \leq \Lambda$$

and

$$\begin{aligned} n(0,t) &= N_0\, s(0)\, e^{\lambda t} = 2 \int_0^\infty n(a,t)\, \delta(a - \Lambda)\, da = 2 N_0\, e^{\lambda t}\, s(\Lambda) \\ \Leftrightarrow s(0) &= 2\, s(\Lambda) = 2\, s(0) e^{-\lambda \Lambda} \\ \Leftrightarrow \lambda &= \frac{\ln 2}{\Lambda} \\ s(0) &= \left[\int_0^\Lambda e^{-\lambda t} \right]^{-1} = \frac{\ln(4)}{\Lambda} \\ n(a,t) &= N_0\, s(a)\, e^{\lambda t} = \frac{N_0 \ln(4)}{\Lambda}\, 2^{\frac{t}{\Lambda}} 2^{\frac{-a}{\Lambda}} \text{ for } a \leq \Lambda \end{aligned} \tag{9.8}$$

The number of cells decreases exponentially with age until it reaches half the value at the age of division Λ (figure 9.1). The total amount of cells $N(t)$ doubles as expected after Λ

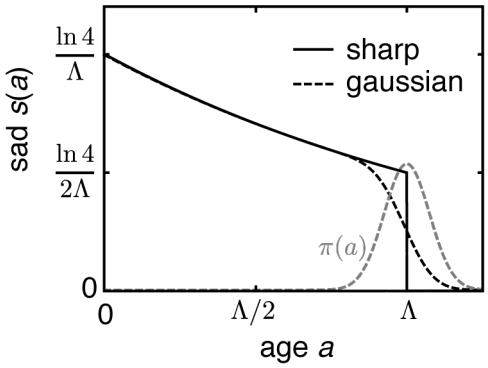

Figure 9.1: For a constant cell cycle length Λ the steady age distribution of the cells declines exponentially with age (black line). The same is true for distributed transition times $\pi(a)$ (dashed gray line) but then in an region dependent on the width of $\pi(a)$ around the mean transition time Λ the distribution deviates from the exponential decline (dashed black line).

$$N(t) = \int_0^\infty n(a,t)\, da = N_0\, 2^{\frac{t}{\Lambda}}.$$

For a Gaussian distribution of cell division times the width of the distribution has no effect on the global steady age distribution, as long as it is sufficiently narrow (figure 9.1). Just the right border at the transition is shaped by the distribution of transition times.

For multiple phases with fixed phase lengths Λ_i one would get for the number of cells at age a in the cell cycle $n_{\text{cycle}}(a,t)$ (as the ages of the single phases have to be added up to get the age in the whole cell cycle)

$$\begin{aligned} n_{\text{cycle}}(a,t) &= \begin{cases} n_1(a,t) & 0 < a \le \Lambda_1 \\ n_2(a-\Lambda_1,t) & \Lambda_1 < a \le \Lambda_2 \\ \vdots & \vdots \\ n_D(a-\sum_{i\in I\setminus\{D\}}\Lambda_i,t) & \Lambda_{D-1} < a \le \Lambda_D \end{cases} \\ \Rightarrow s_{\text{cycle}}(0) &= s_1(0) = 2s_D(\Lambda_D) = 2s_{\text{cycle}}(\sum\nolimits_i \Lambda_i). \end{aligned}$$

Thus as expected, analogous to equation 9.8, the solution is the same as for the case of one phase with fixed length

$$n_{\text{cycle}}(a,t) \quad = \quad N_0\, 2^{-\frac{a}{\Lambda}}\, 2^{\frac{t}{\Lambda}} \text{ with } \Lambda = \sum\nolimits_i \Lambda_i.$$

9.3 Apoptosis

We include cells in an apoptotic state $n_a(a,t)$ into which cells enter from all other phases with rates $l_i(a)$. This additional rate enters the steady age distribution, but not the boundary condition of the equation system

$$\begin{aligned} \partial_t\, n_i(a,t) + \partial_a\, n_i(a,t) &= -\left(k_i(a) + l_i(a)\right)\, n_i(a,t) \\ n_{i+1}(0,t) &= \xi_{i+1} \int_0^\infty n_i(a,t)\, k_i(a)\, da \\ n_i(a,0) &= N_{0,i}\, s_i(a). \end{aligned}$$

In measurements of apoptotic cells (e.g. fractionated DNA, caspase cleavage) the cells are just detectable for a limited time span. Therefore, we have to take into account, the time in which apoptotic cells are detectable. This is modeled by the rate $\kappa(a)$ (where a is the age in the apoptotic state), which describes the time until the apoptotic cells are not detectable any more. The equations for the apoptotic state read

$$\begin{aligned} \partial_t\, n_{\text{a}}(a,t) + \partial_a\, n_{\text{a}}(a,t) &= -\kappa(a)\, n_{\text{a}}(a,t) \\ n_{\text{a}}(0,t) &= \sum_{i\in I} \int_0^\infty n_i(a,t)\, l_i(a)\, da \\ n_{\text{a}}(a,0) &= N_{0,\text{a}}\, s_{\text{a}}(a). \end{aligned}$$

So the equations for the fractions of cells in a certain phase u_i and u_{a} is

$$\begin{aligned} u_{i+1}\, s_{i+1}(0) &= u_i\, s_i(0)\, \xi_{i+1} \int_0^\infty e^{-\lambda a - \int_0^a (k_i(a^*)+l_i(a^*))\, da^*}\, k_i(a) da \\ u_{\text{a}}\, s_{\text{a}}(0) &= \sum_{i\in I} u_i\, s_i(0) \int_0^\infty e^{-\lambda a - \int_0^a (k_i(a^*)+l_i(a^*))\, da^*}\, l_i(a) da \\ s_{\text{a}}(0) &= \left[\int_0^\infty \exp\left\{-\lambda a - \int_0^a \kappa(a^*)\, da^*\right\} da\right]^{-1}. \end{aligned} \tag{9.9}$$

When we include pdfs for the phases $i \in I$ both for apoptosis ρ_i and for phase transitions π_i there is a freedom to define the rates. One possibility is to use a competition model as in [55], where the apoptosis machinery is competing with the cell cycle machinery. Since we want to treat the decision to undergo apoptosis independently from the time of the decision to undergo cell cycle commitment we introduce the probability ω_i to undergo apoptosis in phase i. This yields

$$\begin{aligned} K_i(a) &= k_i(a) + l_i(a) \\ \frac{\Pi_i(a)}{1-\chi(\Pi_i)} &= \frac{(1-\omega_i)\,\pi_i(a) + \omega_i\,\rho_i(a)}{1-((1-\omega_i)\chi(\pi_i) + \omega_i\chi(\rho_i))} \\ \Rightarrow k_i(a) &= \frac{(1-\omega_i)\,\pi_i(a)}{1-((1-\omega_i)\chi(\pi_i) + \omega_i\chi(\rho_i))} \text{ and} \\ l_i(a) &= \frac{\omega_i\,\rho_i(a)}{1-((1-\omega_i)\chi(\pi_i) + \omega_i\chi(\rho_i))}, \end{aligned}$$

with $K_i(a)$ the transition rate and $\Pi_i(a)$ the pdf of apoptotic and cycling transitions.

9.4 Division times from single cell live microscopy

We used conditionally *MYCN* expressing SH-EP cells transfected with a p21 promoter driving the fluorophore mCherry with an added nuclear localization sequence for single cell live microscopy. From three day time courses for both endogenous *MYCN* expression (*MYCN*-off) and *MYCN* overexpressing (*MYCN*-on) cells the cell cycle lengths could be detected semi-automatically. The cells were tracked [117, 50] and then the trajectories inspected manually and corrected where required. The tracking of 101 *MYCN*-off cells showed a mean division time of 23.1 hours with a standard deviation of 5.4 hours whereas the measurements of 52 *MYCN*-on cells resulted in a mean of 18.0 hours with a standard deviation of 3.2 hours (figure 9.2). Thus, the coefficient of variation of the division times distribution was smaller for *MYCN*-on cells. Both distributions are skewed to the right. The skewness of the distribution for *MYCN*-on cells is slightly higher (skew *MYCN*-on: 0.98 compared to skew *MYCN*-off: 0.62).

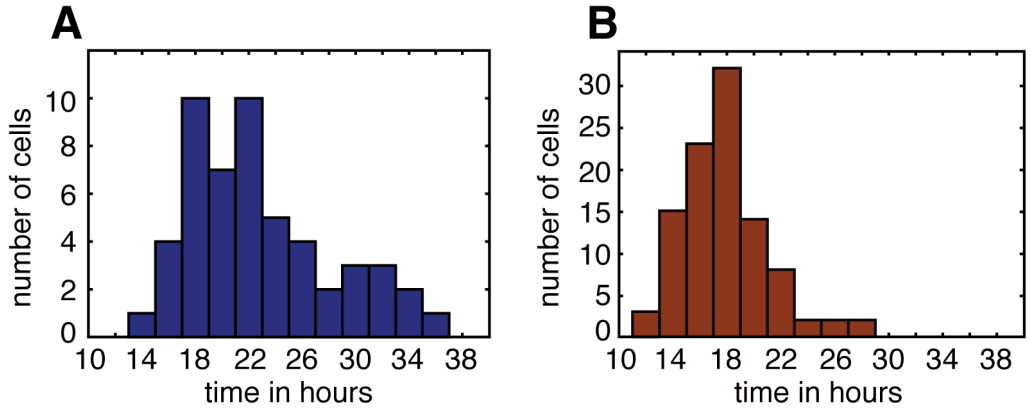

Figure 9.2: (**A**) Measured distribution of division times for the *MYCN*-off SH-EP T21N p21mCherry cells. (**B**) The measured distribution of the *MYCN*-on cells is shifted to the right with smaller width compared to the *MYCN*-off condition.

9.5 Phase durations from DNA content FACS measurements

In the presented framework we have derived a system of equations 9.9 for the steady age distributions of multiple cell cycle phases with apoptosis. This can be utilized to analyze FACS data of cell populations to derive underlying parameters like cell cycle phase durations and apoptosis probability.

DNA content of conditionally *MYCN* expressing SH-EP cells were measured by FACS (figure 9.3 A). After MYCN induction a reduction of cells in G1 phase and an increase of cells in S and G2 phase were visible. Additionally the fraction of apoptotic cells showed an increase of 55 %. The equations 9.9 give the relation between fraction of cells measured in the phases (G1, S, G2, apoptosis) and the rates for the transitions. We solved the equations numerically for the mean transition times μ_i, the growth rate λ and the apoptosis probability ω. For this we assumed Gaussian transition probabilities. To model cell cycle phase dependent apoptosis we used the idea that cells progress through the cell cycle at different velocities and that the behavior of the cell cycle dependent genes is governed by the relative progress through the cell cycle [26]. Accordingly apoptosis was implemented to occur at 80 % completion of the G1 phase ($0.8 \cdot \mu_1$). This was motivated by apoptosis measurements [44]. The time span during which apoptotic cells can be measured (given by $\kappa(a)$) was set to 10 hours. Additionally, we used the measured total cell cycle times for *MYCN*-on and *MYCN*-off condition from section 9.4 to get the mean total cell cycle times which is the sum of the mean transition times (equation 9.7). The widths of the transitions were chosen such that the resulting total variance agreed with the measured variance. However, the resulting mean phase durations were insensitive

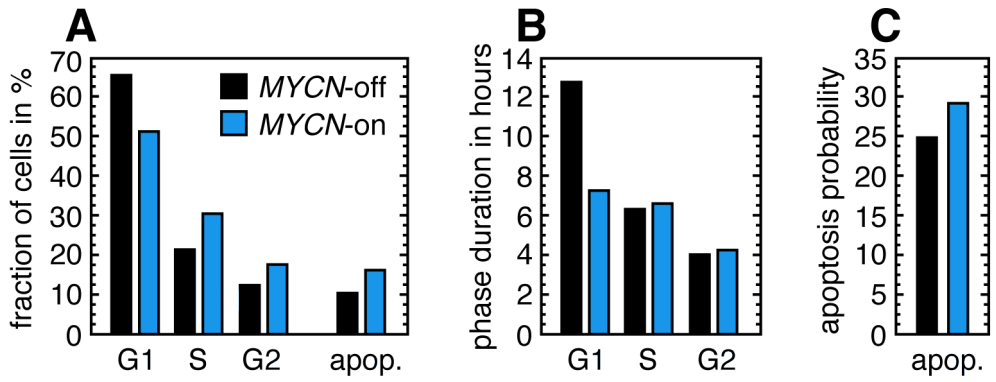

Figure 9.3: (**A**) After MYCN induction the cell fraction in G1 phase decreased whereas the fractions in S and G2 phase increased (measured by DNA content measurements using FACS). The apoptotic fraction increased by 55 %. (**B**) Calculating the phase durations with the introduced model showed that the length of the G1 phase shortened and the length of the S and G2 phases did not change. (**C**) The calculated probability to undergo apoptosis showed a minor increase with *MYCN* overexpression. The strong increase in the apoptotic fraction in the measurements might be explained by the faster cycling of the *MYCN*-on cells and the resulting more frequent passage of cell cycle control points.

to a change in the variance of the underlying pdf (at least under such variations for such the resulting total variance in the simulation was close to the measured variance). The results (figure 9.3 B & C) showed that the duration of the G1 phase decreases with MYCN whereas the duration of S and G2 phase remained constant.

To compare the growth of cells with and without *MYCN* overexpression we simulated the proliferation of a single cell for the two conditions for a time course of seven days. *MYCN* overexpressing cells grow much faster and reach six fold the number of *MYCN*-off cells after one week (figure 9.4). The apoptosis probability did not change much between *MYCN*-off and *MYCN*-on (increase of 16 %). We tested our results for the influence of the time that apoptotic cells remain in the system (determined by κ) and the age at which cells die in the G1 phase. For a change of κ just a minor change in the resulting mean phase times was observed whereas the apoptosis probability was highly dependent. However, variations in the value of κ did not change the difference in the apoptosis probability between *MYCN*-off and *MYCN*-on cells. Changes in the age at which apoptosis occurred did influence the output significantly.

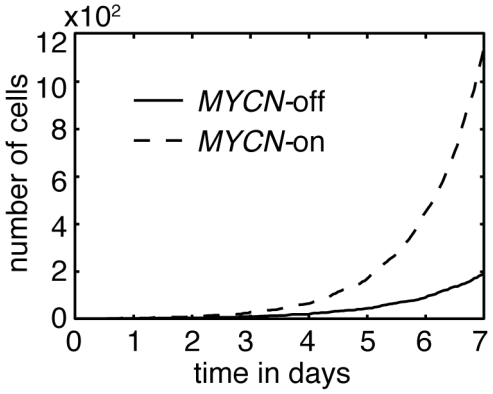

Figure 9.4: Simulated cell population size of the *MYCN*-on cells exceeds six times the size of the *MYCN*-off cell population after seven days of growth.

9.6 Desynchronisation

For several experiments it is beneficial or even necessary to synchronize cells with respect to their cell cycle position, for example to investigate effects in certain phases only. We wanted to investigate how long this cells will be synchronized until, via stochastic processes, the cell cycle positions are decorrelated. From the measured distribution of cell cycle durations we can estimate the desynchronisation time of the cells. Note that normally distributed frequencies of cell cycle progression speed would lead to an inverse Gaussian distribution of division times [85] in accordance to the usually observed right skewed distributions of cell cycle duration. Thus, we fitted two inverse normal distributions

$$\mathcal{I}(\mu, \lambda) = \left[\frac{\lambda}{2\pi x^3}\right]^{1/2} \exp \frac{-\lambda(x-\mu)^2}{2\mu^2 x}$$

to the measured distributions from section 9.4 (figure 9.5). Indeed, the two distributions are fitted reasonably well by inverse normal distributions as shown by a χ^2 analysis. Interestingly fitting a normal distribution lead to a similar result with respect to fitting performance for the *MYCN*-on distribution but performed poorly in fitting the *MYCN*-off distribution. Fitting a log normal distribution gave the opposite result: good fit for the *MYCN*-off distribution and a worse fit for the *MYCN*-on distribution (table 9.1). Thus, we used an inverse normal distribution to analyze desynchronisation.

Let $\mathcal{P}_0$ be the distribution of positions in the cell cycle for cells synchronized by arrest

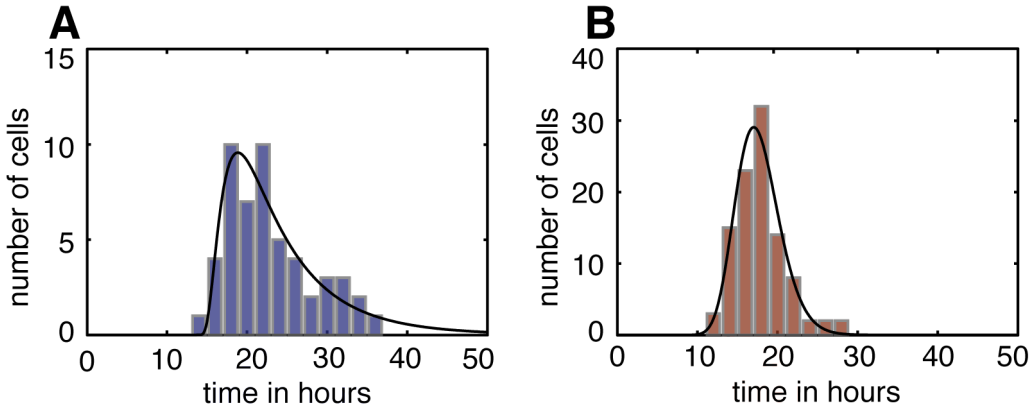

Figure 9.5: (**A**) The distribution of cell cycle durations for the *MYCN*-off cells is well fitted by an inverse normal distribution. (**B**) This is also true for the distribution of the cell cycle durations of *MYCN*-on cells with smaller width and less skewness.

distribution	χ^2_{off}	χ^2_{on}
normal	37	49
log normal	18	155
inverse normal	18	55

Table 9.1: χ^2 values for the fit of the cell cycle length distribution for the *MYCN*-off cells (χ^2_{off}) and the *MYCN*-on cells (χ^2_{on}). The fit of an inverse normal distribution resulted in the best combined χ^2 value, where all three distributions were fitted with two degrees of freedom.

(e.g. by serum starvation or a thymidine block). When the cells are released again the distribution broadens because of differences in speed of cell cycle progression. After every cell division the distribution of the cells in the cell cycle can be estimated by taking the starting distribution $\mathcal{P}_0$ and convolute it with the fitted distribution for the cell cycle durations $\mathcal{I}$ and analogous $\mathcal{P}_i = \mathcal{P}_{i-1} \circ \mathcal{I}$. So for every division the variance of the distribution of the cell cycle durations $\sigma^2(\mathcal{I})$ is added to the variance of the actual distribution $\sigma^2(\mathcal{P}_i)$ (values table 9.2). That would mean both for *MYCN*-on and *MYCN*-off cells after three divisions the value of two standard deviations is bigger than half of the mean. Already after one division for both populations the value of two standard deviations is in the order of the length of the G1 phase. The proposed framework of steady age distributions might lead to a future standard method to analyze FACS-measured cell cycle data to deduce underlying parameters.

	mean μ	variance σ^2	two standard deviation 2σ
MYCN-off	23.9 hours	47.6 hours^2	13.8 hours
MYCN-on	17.9 hours	7.6 hours^2	5.5 hours

Table 9.2: Mean and variance for the fitted distributions for *MYCN*-off and *MYCN*-on cells. The width of the distribution (two standad deviations) is in the order of the duration of the S phase. For a synchronized dividing cell population this means a rather fast desynchronization (for every division the variance of the cell cycle length distribution is added to the variance of the distribution of cells in the cell cycle).

10 Conclusions and discussion Neuroblastoma

10.1 p53-MDM2 core module

Mathematical models can help to analyze the responses of systems with multiple interactions. Especially the response of networks with feedback loops are very hard to predict. Often it is intuitionally not clear, if a given network is able to produce a certain measured response. We established a model of the p53-MDM2 core module to rationalize the dysfunction of the DNA damage response in neuroblastoma and the role MYCN plays therein.

Some measurements in the SH-EP T21N cells did not show an increase of the p53 level upon DNA damage induction, seemingly contradicting the believed mechanism of sensing DNA damage and subsequent p53 stabilizing with increase of p53 level [155]. An analysis of the mathematical model of p53-MDM2 core module showed that the steady state of the system exhibits a universal behavior upon p53 activation in phase space. Thus, the possible responses of this module could be systematically determined. This set of possible trajectories included the measured transient MDM2 induction with simultaneously constant or even decreasing level of total p53 concentration. The explanation why p53 is not induced is that the increase of stabilized active p53 is compensated by the increased p53 degradation via MDM2-mediated ubiquitination. To validate the mathematical model and to further analyze the response to DNA damage it would be very beneficial to experimentally distinguish between transcriptionally active and transcriptionally inactive p53. One possibility to detect p53 activity would be to use a p53 target gene as a measure of p53 activity or to use antibodies specific to certain posttranslational modifications of p53 [125, 57, 79].

The negative feedback of p53 via MDM2 renders the system already in the noncomplex model without mRNA regulation close to oscillatory. Including also MDM2 mRNA generates oscillatory behavior if parameters are chosen appropriately. This is in line with experimental observations of oscillatory or pulse like responses of p53 and MDM2 [73, 68, 79]. We did not observe any indication of this behavior in the neuroblastoma cells when monitoring p21 promoter activity in SH-EP T21N p21mCherry cells after doxorubicin treatment on single cell level under the

microscope. The lack of the oscillatory behavior might be attributed to differences between the cell types or by a dampening effect of the p21 promoter reporter regulation. Another explanation might be a malignant dysregulation of the p53-MDM2 core module in the neuroblastoma cells inhibiting p53 and MDM2 oscillations. Due to the fact that we could not observe any oscillations, we progressed with the presented framework and did not investigate the oscillatory regimes of the model as was done in previous studies [81, 22, 116, 42, 8, 41]. It might also be possible that there are no p53 oscillations observed in the SH-EP cells due to the deletion of $p14^{ARF}$, a negative regulator of MDM2 [147]. The role of $p14^{ARF}$ for oscillations was already mentioned in [113] in a qualitative model analysis.

The protein levels in several neuroblastoma cell lines (including *MYCN* wild-type and *MYCN*-amplified cells) differ strongly. The mathematical model shows that the differences of the protein levels can be explained by using the MYCN level in the cells as input and considering the status of p53 (mutated or not). Only the high MDM2 and p21 protein levels in the two SH-EP cell clones could not be explained just by the measured MYCN levels. An additional parameter allowing for higher p53 activity in these cells was needed to reproduce the measured data. We hypothesized that this parameter may account for the deletion of the $p14^{ARF}$ gene in the SH-EP cell line. However, both a simulation including $p14^{ARF}$ regulation and a SH-EP clone with a conditionally $p14^{ARF}$ knock in showed a resulting decrease of MDM2 level after $p14^{ARF}$ overexpression. Thus, the reason for the high MDM2 and p21 level in the SH-EP cell line remains unknown. The level of p53 for the SK-BE(2)C cells is overestimated by the model. One possible explanation for this is a lower stability of the mutated p53. In summary, it remains plausible that the main reason for differences in protein level between these neuroblastoma cell lines is mainly attributed to their differences in MYCN protein level. However, the apparent high p53 activity in the SH-EP cells remains an issue for further investigations.

We measured the response of p53, MDM2 and p21 upon DNA damage and upon treatment with the small molecule inhibitor Nutlin-3 in two clones of the SH-EP cell line. The resulting time courses differed between these two measurements. However, both can be qualitatively reproduced by the mathematical model of the p53-MDM2 core module. In both measurements the p21 response is weaker in the *MYCN*-on cells compared to the *MYCN*-off cells. This is reproduced in the model just by the impact MYCN has on the protein level of p53 and MDM2 and the p21 regulation. Despite the upregulation of p53, which potentially enhances the p21 induction it seems that the negative control of MYCN on the p53 mediated p21 activation and the increase of MDM2, which both repress cell cycle arrest, is dominant over the effect of the p53 protein increase. Thus, it is plausible that the weak G1 arrest in the *MYCN*-on SH-EP cells is due to a MYCN induced protein level imbalance in the p53-MDM2 module.

A measurement of MDM2 mRNA levels upon doxorubicin treatment showed a de-

crease after $\sim$ 15 hours after treatment, which is not captured by the corresponding model fit. In the model only a decrease of p53 could produce such a behavior (resulting also in a MDM2 decrease). However, this would contradict the observed increase in the p21 mRNA level (while PUMA mRNA level stays constant). Probably the MDM2 behavior indicates a more complex gene regulation or another regulatory interaction, such as interactions with the MDM4 protein [128, 72]. The MDM4 protein which is associated with the regulation of the p53-MDM2 response and potentially plays an important role in other embryonic tumors [110, 48, 40] is not included in the model. This regulation might account for the observed kinetics which could not be explained by the model. For all time points but the last the level of mRNA after Nutlin-3 treatment is higher than after doxorubicin treatment. At the last time point the mRNA level of p21 decreases after Nutlin-3 treatment and is lower than the measurement in the cells after doxorubicin treatment. Here further experimental investigation is necessary to see if this is Nutlin-3 specific or if this can be attributed to other effects such as apoptosis. Also to assess the differences between the two shown datasets collected in the SH-EP clones further experimental investigations are needed. Both measurements were just performed once and have to be validated.

The measured responses of p53 and MDM2 for MYCN-on and MYCN-off conditions in the IMR5-75 cells did not show any significant differences. Only the p21 response is modulated under changed MYCN level. Thus, the MYCN level change seems to be in a regime, where neither p53 nor MDM2 expression is sensitive to it. However, qRT-PCR showed that the expression of other genes involved in the G1-S transition like *CDK4* were changed significantly after MYCN knock down in the IMR5-75 cells. Consequently, it seems important to consider the MYCN impact on both the p53-MDM2 axis and the E2F1-pRB axis. This is also indicated by the finding that perturbation of both axes with simultaneous Nutlin-3 and CDK4i treatment exerted a synergistic effect on the growth of neuroblastoma cells.

10.2 E2F1-pRB regulation

A basic model for the E2F1-pRB interaction, governing the transition from G1 to S phase was established. In contrast to other studies, which also model the R-point as a bistable switch [2, 53, 106, 164], this mathematical model is a linear model including just the core interaction of E2F1, pRB protein and the promoter binding sites. Nonetheless it exhibits bistability in line with the experimental findings of [164].

To account for the most important regulatory mechanism governing the dysfunctional G1-S transition in neuroblastoma we included feedback regulation of SKP2 and CDK2, as well as the impact of MYCN and p21 in the model [98, 44]. This extension of the mathematical model allowed us to utilize the bifurcation diagram as

a readout to investigate the effect of perturbations on the system (such as different *MYCN* levels and treatment with chemotherapeutical drugs or protein inhibitors). The bifurcation curve is highly dependent on the input level of MYCN. Higher MYCN levels shift the G1-S transition to lower activation levels (e.g. growth factors, serum). Plotting the bistable regime as function of p21 and CDK4 shows that it is most effective to target both simultaneously to restore a functional G1-S transition or to even induce G1 arrest. This is in line with the observed synergistic effect, Nutlin-3 and CDK4i have on neuroblastoma cell growth [157]. The model serves as a valuable tool to predict and understand the effect of network perturbations.

To determine the model parameter it is necessary to test, if the G1-S transition in the neuroblastoma cells really show a bistable behavior or if by malignant transformation or differences in cellular parameters (e.g. amount of E2F1, genetic background) the bistable switch is altered. This could be measured by using single cell measurements [164]. Furthermore it would be very interesting to test if the modeled change of the bifurcation diagram is directly related to the measured change of G1 phase duration after conditional *MYCN* overexpression. By simulating the time to reach a certain E2F1 activity threshold level as a function of CDK4 level the model might be able to predict the length of the G1 phase under different conditions. If it is possible to validate this experimentally it could eventually be used as an input for the phenomenological cell cycle model. Thereby an integrated cell cycle model could be generated to connect molecular mechanisms to cell population measurements.

One problem of the model is the mapping of the bifurcation diagram to a cell population behavior. There are many mechanisms by which cell to cell variability in crossing the G1-S transition can arise such as the availability of growth factors, E2F1 concentration and upstream signaling [71]. However, measurements at single cell level can potentially resolve this problem.

Most of the *MYCN*-amplified cell lines show a strongly impaired G1 arrest after serum starvation (Frank Westermann, private correspondence). The pRB-E2F1 model indicates that the combination of Nutlin-3 and CDK4i can compensate for the MYCN effect on the G1-S transition. It would be interesting if the treated cells can be arrested by additional serum starvation after treatment with Nutlin-3 or CDK4i.

10.3 SAD model

By utilizing a phenomenological model of the cell cycle describing an age structured population, we provided a mathematical framework to extract underlying cell cycle parameters, which are difficult to measure directly, from combined FACS-measured cell cycle phase distributions and cell growth rate measurements. The formulation of the equations allow the implementation of biological assumptions directly related to the measurements (e.g. the estimated apoptosis probability).

The model showed that conditionally upregulated MYCN in the SH-EP cells mainly affect the length of the G1 phase. Interestingly, the apoptosis probability does not change much. However, the faster cell cycling causes the cells to pass the points of the cell cycle at which the cells are more likely to undergo apoptosis more frequently. This explains the higher fraction of apoptotic cells in the *MYCN*-on cell population (increase of 55 percent).

Recently published models proposed an intracellular competition of different processes for lymphocyte proliferation, apoptosis and differentiation [169, 31, 30]. Here, in contrast we assumed apoptosis to be mainly coupled to the cell cycle regulation [162, 99, 149] and to occur at a specific region of the cell cycle (the deduced parameter values are not strongly dependent on the exact choice of the region). This assumption has to be tested experimentally by better quantifying apoptosis in neuroblastoma cells and relating it to the cell cycle progression. This might be possible by time course FACS measurements in combination with mRNA or protein quantification methods.

By verifying the predicted phase length of the model for example by single cell fluorescent live microscopy utilizing FUCCI dyes [119] the model could be used as a standard analysis tool for cell cycle data. Besides the analysis of the FACS measurements the SAD model might also be used to model synchronized or perturbed cell populations by implementing a stochastic simulation in the framework.

The main goal of the future work should be the integration of the mathematical model of the p53-MDM2 core module and the pRB-E2F1 model with the phenotypical read out of cell growth and cell cycle phase durations. To achieve this several experiments have to be performed. The data for the p53-MDM2 model has to be validated. To fit the pRB-E2F1 model single cell measurements of the G1-S transition have to be carried out and compared to the model. It remains questionable if the G1-S transition is at all bistable in neuroblastoma cells.

Bibliography

[1] S. Adhikary and M. Eilers. Transcriptional regulation and transformation by Myc proteins. *Nat. Rev. Mol. Cell Biol.*, 6(8):635–645, Aug 2005.

[2] B. D. Aguda and Y. Tang. The kinetic origins of the restriction point in the mammalian cell cycle. *Cell Prolif.*, 32(5):321–335, Oct 1999.

[3] H. Akaike. Information theory and an extension of the maximum likelihood principle. In B. N. Petrov & F. Caski, editor, *Proceedings of the Second International Symposium on Information Theory*, pages 267–281, 1973. Budapest: Akademiai Kiado.

[4] C. Attwooll, E. Lazzerini Denchi, and K. Helin. The E2F family: specific functions and overlapping interests. *EMBO J.*, 23(24):4709–4716, Dec 2004.

[5] Stephan Beirer. *Mathematical Modelling of the Jak/Stat1 Signal Transduction Pathway.* PhD thesis, Humboldt University Berlin, 2007.

[6] E. Bell, J. Lunec, and D. A. Tweddle. Cell cycle regulation targets of MYCN identified by gene expression microarrays. *Cell Cycle*, 6(10):1249–1256, May 2007.

[7] J. Bloom and M. Pagano. Deregulated degradation of the cdk inhibitor p27 and malignant transformation. *Semin. Cancer Biol.*, 13(1):41–47, Feb 2003.

[8] S. Bottani and B. Grammaticos. Analysis of a minimal model for p53 oscillations. *J. Theor. Biol.*, 249(2):235–245, Nov 2007.

[9] M. M. Bradford. A rapid and sensitive method for the quantitation of microgram quantities of protein utilizing the principle of protein-dye binding. *Anal. Biochem.*, 72:248–254, May 1976.

[10] D. Bray, M. D. Levin, and C. J. Morton-Firth. Receptor clustering as a cellular mechanism to control sensitivity. *Nature*, 393(6680):85–88, May 1998.

[11] G. M. Brodeur, J. Pritchard, F. Berthold, N. L. Carlsen, V. Castel, R. P. Castelberry, B. De Bernardi, A. E. Evans, M. Favrot, and F. Hedborg. Revisions of the international criteria for neuroblastoma diagnosis, staging, and response to treatment. *J. Clin. Oncol.*, 11(8):1466–1477, Aug 1993.

[12] G. M. Brodeur, R. C. Seeger, M. Schwab, H. E. Varmus, and J. M. Bishop. Amplification of N-myc in untreated human neuroblastomas correlates with advanced disease stage. *Science*, 224(4653):1121–1124, Jun 1984.

[13] J. Bromberg and J. E. Darnell. The role of STATs in transcriptional control and their impact on cellular function. *Oncogene*, 19(21):2468–2473, May 2000.

[14] R. Buettner, L. B. Mora, and R. Jove. Activated STAT signaling in human tumors provides novel molecular targets for therapeutic intervention. *Clin. Cancer Res.*, 8(4):945–954, Apr 2002.

[15] A. Burgess, M. Wigan, N. Giles, W. Depinto, P. Gillespie, F. Stevens, and B. Gabrielli. Inhibition of S/G2 phase CDK4 reduces mitotic fidelity. *J. Biol. Chem.*, 281(15):9987–9995, Apr 2006.

[16] J. Carr, E. Bell, A. D. Pearson, U. R. Kees, H. Beris, J. Lunec, and D. A. Tweddle. Increased frequency of aberrations in the p53/MDM2/p14(ARF) pathway in neuroblastoma cell lines established at relapse. *Cancer Res.*, 66(4):2138–2145, Feb 2006.

[17] J. Carr-Wilkinson, R. Griffiths, R. Elston, L. D. Gamble, B. Goranov, C. P. Redfern, J. Lunec, and D. A. Tweddle. Outcome of the p53-mediated DNA damage response in neuroblastoma is determined by morphological subtype and MYCN expression. *Cell Cycle*, 10(21):3778–3787, Nov 2011.

[18] J. Carr-Wilkinson, K. O'Toole, K. M. Wood, C. C. Challen, A. G. Baker, J. R. Board, L. Evans, M. Cole, N. K. Cheung, J. Boos, G. Kohler, I. Leuschner, A. D. Pearson, J. Lunec, and D. A. Tweddle. High Frequency of p53/MDM2/p14ARF Pathway Abnormalities in Relapsed Neuroblastoma. *Clin. Cancer Res.*, 16(4):1108–1118, Feb 2010.

[19] A. C. Carrano, E. Eytan, A. Hershko, and M. Pagano. SKP2 is required for ubiquitin-mediated degradation of the CDK inhibitor p27. *Nat. Cell Biol.*, 1(4):193–199, Aug 1999.

[20] R. P. Castleberry. Neuroblastoma. *Eur. J. Cancer*, 33(9):1430–1437, Aug 1997.

[21] L. Chen, N. Iraci, S. Gherardi, L. D. Gamble, K. M. Wood, G. Perini, J. Lunec, and D. A. Tweddle. p53 is a direct transcriptional target of MYCN in neuroblastoma. *Cancer Res.*, 70(4):1377–1388, Feb 2010.

[22] A. Ciliberto, B. Novak, and J. J. Tyson. Steady states and oscillations in the p53/Mdm2 network. *Cell Cycle*, 4(3):488–493, Mar 2005.

[23] L. Connell-Crowley, J. W. Harper, and D. W. Goodrich. Cyclin D1/Cdk4 regulates retinoblastoma protein-mediated cell cycle arrest by site-specific phosphorylation. *Mol. Biol. Cell*, 8(2):287–301, Feb 1997.

[24] J. E. Darnell. STATs and gene regulation. *Science*, 277(5332):1630–1635, Sep 1997.

[25] G. M. Davey, W. R. Heath, and R. Starr. SOCS1: a potent and multifaceted regulator of cytokines and cell-mediated inflammation. *Tissue Antigens*, 67(1):1–9, Jan 2006.

[26] U. de Lichtenberg, L. J. Jensen, A. Fausbøll, T. S. Jensen, P. Bork, and S. Brunak. Comparison of computational methods for the identification of cell cycle-regulated genes. *Bioinformatics*, 21(7):1164–1171, Apr 2005.

[27] T. Decker and P. Kovarik. Serine phosphorylation of STATs. *Oncogene*, 19(21):2628–2637, May 2000.

[28] T. Decker, D. J. Lew, J. Mirkovitch, and J. E. Darnell. Cytoplasmic activation of GAF, an IFN-gamma-regulated DNA-binding factor. *EMBO J.*, 10(4):927–932, Apr 1991.

[29] M. Droescher, A. Begitt, A. Marg, M. Zacharias, and U. Vinkemeier. Cytokine-induced paracrystals prolong the activity of signal transducers and activators of transcription (STAT) and provide a model for the regulation of protein solubility by small ubiquitin-like modifier (SUMO). *J. Biol. Chem.*, 286(21):18731–18746, May 2011.

[30] K. R. Duffy and P. D. Hodgkin. Intracellular competition for fates in the immune system. *Trends Cell Biol.*, 22(9):457–464, Sep 2012.

[31] K. R. Duffy, C. J. Wellard, J. F. Markham, J. H. Zhou, R. Holmberg, E. D. Hawkins, J. Hasbold, M. R. Dowling, and P. D. Hodgkin. Activation-induced B cell fates are selected by intracellular stochastic competition. *Science*, 335(6066):338–341, Jan 2012.

[32] N. Dyson. The regulation of E2F by pRB-family proteins. *Genes Dev.*, 12(15):2245–2262, Aug 1998.

[33] T. Endo and D. Kohda. Functions of outer membrane receptors in mitochondrial protein import. *Biochim. Biophys. Acta*, 1592(1):3–14, Sep 2002.

[34] U. Eser, M. Falleur-Fettig, A. Johnson, and J. M. Skotheim. Commitment to a cellular transition precedes genome-wide transcriptional change. *Mol. Cell*, 43(4):515–527, Aug 2011.

[35] R. Fagerlund, K. Melen, L. Kinnunen, and I. Julkunen. Arginine/lysine-rich nuclear localization signals mediate interactions between dimeric STATs and importin alpha 5. *J. Biol. Chem.*, 277(33):30072–30078, Aug 2002.

[36] M. Fornerod, M. Ohno, M. Yoshida, and I. W. Mattaj. CRM1 is an export receptor for leucine-rich nuclear export signals. *Cell*, 90(6):1051–1060, Sep 1997.

[37] M. Fukuda, S. Asano, T. Nakamura, M. Adachi, M. Yoshida, M. Yanagida, and E. Nishida. CRM1 is responsible for intracellular transport mediated by the nuclear export signal. *Nature*, 390(6657):308–311, Nov 1997.

[38] S. Fulda, W. Lutz, M. Schwab, and K. M. Debatin. MycN sensitizes neuroblastoma cells for drug-induced apoptosis. *Oncogene*, 18(7):1479–1486, Feb 1999.

[39] S. Fulda, H. Sieverts, C. Friesen, I. Herr, and K. M. Debatin. The CD95 (APO-1/Fas) system mediates drug-induced apoptosis in neuroblastoma cells. *Cancer Res.*, 57(17):3823–3829, Sep 1997.

[40] D. Garcia, M. R. Warr, C. P. Martins, L. Brown Swigart, E. Passegue, and G. I. Evan. Validation of MdmX as a therapeutic target for reactivating p53 in tumors. *Genes Dev.*, 25(16):1746–1757, Aug 2011.

[41] N. Geva-Zatorsky, E. Dekel, E. Batchelor, G. Lahav, and U. Alon. Fourier analysis and systems identification of the p53 feedback loop. *Proc. Natl. Acad. Sci. U.S.A.*, 107(30):13550–13555, Jul 2010.

[42] N. Geva-Zatorsky, N. Rosenfeld, S. Itzkovitz, R. Milo, A. Sigal, E. Dekel, T. Yarnitzky, Y. Liron, P. Polak, G. Lahav, and U. Alon. Oscillations and variability in the p53 system. *Mol. Syst. Biol.*, 2:2006.0033, 2006.

[43] Daniel T. Gillespie. Exact stochastic simulation of coupled chemical reactions. *J. Phys. Chem.*, 81(25):2340–2361, 1977.

[44] S. Gogolin, V. Ehemann, G. Becker, L. M. Brueckner, D. Dreidax, I. Nolte, L. Savelyeva, and F. Westermann. Deregulation of the pRB pathway impairs drug-induced DNA damage response in neuroblastoma. *in preparation*, 2012.

[45] D. Goldschneider, E. Horvilleur, L. F. Plassa, M. Guillaud-Bataille, K. Million, E. Wittmer-Dupret, G. Danglot, H. de The, J. Benard, E. May, and S. Douc-Rasy. Expression of C-terminal deleted p53 isoforms in neuroblastoma. *Nucleic Acids Res.*, 34(19):5603–5612, 2006.

[46] C. J. Greenhalgh and D. J. Hilton. Negative regulation of cytokine signaling. *J. Leukoc. Biol.*, 70(3):348–356, Sep 2001.

[47] A. C. Greenlund, M. O. Morales, B. L. Viviano, H. Yan, J. Krolewski, and R. D. Schreiber. Stat recruitment by tyrosine-phosphorylated cytokine receptors: an ordered reversible affinity-driven process. *Immunity*, 2(6):677–687, Jun 1995.

[48] Y. Guo, S. Pajovic, and B. L. Gallie. Expression of p14ARF, MDM2, and MDM4 in human retinoblastoma. *Biochem. Biophys. Res. Commun.*, 375(1):1–5, Oct 2008.

[49] J. W. Harbour, R. X. Luo, A. Dei Santi, A. A. Postigo, and D. C. Dean. Cdk phosphorylation triggers sequential intramolecular interactions that progressively block Rb functions as cells move through G1. *Cell*, 98(6):859–869, Sep 1999.

[50] N. Harder, F. Mora-Bermudez, W. J. Godinez, A. Wunsche, R. Eils, J. Ellenberg, and K. Rohr. Automatic analysis of dividing cells in live cell movies to detect mitotic delays and correlate phenotypes in time. *Genome Res.*, 19(11):2113–2124, Nov 2009.

[51] R. L. Haspel, M. Salditt-Georgieff, and J. E. Darnell. The rapid inactivation of nuclear tyrosine phosphorylated Stat1 depends upon a protein tyrosine phosphatase. *EMBO J.*, 15(22):6262–6268, Nov 1996.

[52] W.K. Hastings. Monte carlo samping methods using markov chains and their applications. *Biometrika*, pages 97–109, 1970.

[53] V. Hatzimanikatis, K. H. Lee, and J. E. Bailey. A mathematical description of regulation of the G1-S transition of the mammalian cell cycle. *Biotechnol. Bioeng.*, 65(6):631–637, Dec 1999.

[54] Y. Haupt, R. Maya, A. Kazaz, and M. Oren. Mdm2 promotes the rapid degradation of p53. *Nature*, 387(6630):296–299, May 1997.

[55] E. D. Hawkins, M. L. Turner, M. R. Dowling, C. van Gend, and P. D. Hodgkin. A model of immune regulation as a consequence of randomized lymphocyte division and death times. *Proc. Natl. Acad. Sci. U.S.A.*, 104(12):5032–5037, Mar 2007.

[56] K. O. Henrich, M. Fischer, D. Mertens, A. Benner, R. Wiedemeyer, B. Brors, A. Oberthuer, F. Berthold, J. S. Wei, J. Khan, M. Schwab, and F. Westermann. Reduced expression of CAMTA1 correlates with adverse outcome in neuroblastoma patients. *Clin. Cancer Res.*, 12(1):131–138, Jan 2006.

[57] A. Hirao, Y. Y. Kong, S. Matsuoka, A. Wakeham, J. Ruland, H. Yoshida, D. Liu, S. J. Elledge, and T. W. Mak. DNA damage-induced activation of p53 by the checkpoint kinase Chk2. *Science*, 287(5459):1824–1827, Mar 2000.

[58] S. Hopkins-Donaldson, P. Yan, K. B. Bourloud, A. Muhlethaler, J. L. Bodmer, and N. Gross. Doxorubicin-induced death in neuroblastoma does not involve death receptors in S-type cells and is caspase-independent in N-type cells. *Oncogene*, 21(39):6132–6137, Sep 2002.

[59] S. Inoshita, Y. Terada, O. Nakashima, M. Kuwahara, S. Sasaki, and F. Marumo. Regulation of the G1/S transition phase in mesangial cells by E2F1. *Kidney Int.*, 56(4):1238–1241, Oct 1999.

[60] R. Kamada, T. Nomura, C. W. Anderson, and K. Sakaguchi. Cancer-associated p53 tetramerization domain mutants: quantitative analysis reveals a low threshold for tumor suppressor inactivation. *J. Biol. Chem.*, 286(1):252–258, Jan 2011.

[61] N. Keshelava, J. J. Zuo, P. Chen, S. N. Waidyaratne, M. C. Luna, C. J. Gomer, T. J. Triche, and C. P. Reynolds. Loss of p53 function confers high-level multidrug resistance in neuroblastoma cell lines. *Cancer Res.*, 61(16):6185–6193, Aug 2001.

[62] S. Kirkpatrick, C. D. Gelatt, and M. P. Vecchi. Optimization by simulated annealing. *Science*, 220(4598):671–680, May 1983.

[63] M. Kitagawa, H. Higashi, H. K. Jung, I. Suzuki-Takahashi, M. Ikeda, K. Tamai, J. Kato, K. Segawa, E. Yoshida, S. Nishimura, and Y. Taya. The consensus motif for phosphorylation by cyclin D1-Cdk4 is different from that for phosphorylation by cyclin A/E-Cdk2. *EMBO J.*, 15(24):7060–7069, Dec 1996.

[64] C. Kossow, D. Jose, R. Jaster, O. Wolkenhauer, and K. Rateitschak. Mathematical modelling unravels regulatory mechanisms of interferon-induced STAT1 serine-phosphorylation and MUC4 expression in pancreatic cancer cells. *IET Syst Biol*, 6(3):73–85, Jun 2012.

[65] P. Kovarik, M. Mangold, K. Ramsauer, H. Heidari, R. Steinborn, A. Zotter, D. E. Levy, M. Muller, and T. Decker. Specificity of signaling by STAT1 depends on SH2 and C-terminal domains that regulate Ser727 phosphorylation, differentially affecting specific target gene expression. *EMBO J.*, 20(1-2):91–100, Jan 2001.

[66] O. H. Kramer, D. Baus, S. K. Knauer, S. Stein, E. Jager, R. H. Stauber, M. Grez, E. Pfitzner, and T. Heinzel. Acetylation of Stat1 modulates NF-kappaB activity. *Genes Dev.*, 20(4):473–485, Feb 2006.

[67] J. P. Kruse and W. Gu. SnapShot: p53 posttranslational modifications. *Cell*, 133(5):930–930, May 2008.

[68] G. Lahav, N. Rosenfeld, A. Sigal, N. Geva-Zatorsky, A. J. Levine, M. B. Elowitz, and U. Alon. Dynamics of the p53-Mdm2 feedback loop in individual cells. *Nat. Genet.*, 36(2):147–150, Feb 2004.

[69] S. E. Lang, S. B. McMahon, M. D. Cole, and P. Hearing. E2F transcriptional activation requires TRRAP and GCN5 cofactors. *J. Biol. Chem.*, 276(35):32627–32634, Aug 2001.

[70] J. F. Lau and C. M. Horvath. Mechanisms of Type I interferon cell signaling and STAT-mediated transcriptional responses. *Mt. Sinai J. Med.*, 69(3):156–168, May 2002.

[71] T. J. Lee, G. Yao, D. C. Bennett, J. R. Nevins, and L. You. Stochastic E2F activation and reconciliation of phenomenological cell-cycle models. *PLoS Biol.*, 8(9), 2010.

[72] K. Lenos and A. G. Jochemsen. Functions of MDMX in the modulation of the p53-response. *J. Biomed. Biotechnol.*, 2011:876173, 2011.

[73] R. Lev Bar-Or, R. Maya, L. A. Segel, U. Alon, A. J. Levine, and M. Oren. Generation of oscillations by the p53-Mdm2 feedback loop: a theoretical and experimental study. *Proc. Natl. Acad. Sci. U.S.A.*, 97(21):11250–11255, Oct 2000.

[74] K. Levenberg. A method for the solution of certain problems in least squares. *Quart. Applied Math.*, 2:164–168, 1944.

[75] D. E. Levy and J. E. Darnell. Stats: transcriptional control and biological impact. *Nat. Rev. Mol. Cell Biol.*, 3(9):651–662, Sep 2002.

[76] B. F. Lillemeier, M. Koster, and I. M. Kerr. STAT1 from the cell membrane to the DNA. *EMBO J.*, 20(10):2508–2517, May 2001.

[77] B. Liu, J. Liao, X. Rao, S. A. Kushner, C. D. Chung, D. D. Chang, and K. Shuai. Inhibition of Stat1-mediated gene activation by PIAS1. *Proc. Natl. Acad. Sci. U.S.A.*, 95(18):10626–10631, Sep 1998.

[78] G. Liu and X. Chen. Regulation of the p53 transcriptional activity. *J. Cell. Biochem.*, 97(3):448–458, Feb 2006.

[79] A. Loewer, E. Batchelor, G. Gaglia, and G. Lahav. Basal dynamics of p53 reveal transcriptionally attenuated pulses in cycling cells. *Cell*, 142(1):89–100, Jul 2010.

[80] W. Lutz, M. Stohr, J. Schurmann, A. Wenzel, A. Lohr, and M. Schwab. Conditional expression of N-myc in human neuroblastoma cells increases expression of alpha-prothymosin and ornithine decarboxylase and accelerates progression into S-phase early after mitogenic stimulation of quiescent cells. *Oncogene*, 13(4):803–812, Aug 1996.

[81] L. Ma, J. Wagner, J. J. Rice, W. Hu, A. J. Levine, and G. A. Stolovitzky. A plausible model for the digital response of p53 to DNA damage. *Proc. Natl. Acad. Sci. U.S.A.*, 102(40):14266–14271, Oct 2005.

[82] T. Maiwald, A. Schneider, H. Busch, S. Sahle, N. Gretz, T. S. Weiss, U. Kummer, and U. Klingmuller. Combining theoretical analysis and experimental data generation reveals IRF9 as a crucial factor for accelerating interferon -induced early antiviral signalling. *FEBS J.*, 277(22):4741–4754, Nov 2010.

[83] A. Marg, T. Meyer, M. Vigneron, and U. Vinkemeier. Microinjected antibodies interfere with protein nucleocytoplasmic shuttling by distinct molecular mechanisms. *Cytometry A*, 73A(12):1128–1140, Dec 2008.

[84] A. Marg, Y. Shan, T. Meyer, T. Meissner, M. Brandenburg, and U. Vinkemeier. Nucleocytoplasmic shuttling by nucleoporins Nup153 and Nup214 and CRM1-dependent nuclear export control the subcellular distribution of latent Stat1. *J. Cell Biol.*, 165(6):823–833, Jun 2004.

[85] J. F. Markham, C. J. Wellard, E. D. Hawkins, K. R. Duffy, and P. D. Hodgkin. A minimum of two distinct heritable factors are required to explain correlation structures in proliferating lymphocytes. *J R Soc Interface*, 7(48):1049–1059, Jul 2010.

[86] Donald W. Marquardt. An algorithm for least-squares estimation of nonlinear parameters. *SIAM Journal on Applied Mathematics*, 11(2):431–441, 1963.

[87] K. K. Matthay, J. G. Villablanca, R. C. Seeger, D. O. Stram, R. E. Harris, N. K. Ramsay, P. Swift, H. Shimada, C. T. Black, G. M. Brodeur, R. B. Gerbing, and C. P. Reynolds. Treatment of high-risk neuroblastoma with intensive chemotherapy, radiotherapy, autologous bone marrow transplantation, and 13-cis-retinoic acid. Children's Cancer Group. *N. Engl. J. Med.*, 341(16):1165–1173, Oct 1999.

[88] K. M. McBride, C. McDonald, and N. C. Reich. Nuclear export signal located within theDNA-binding domain of the STAT1transcription factor. *EMBO J.*, 19(22):6196–6206, Nov 2000.

[89] A. G. McKendrick. Applications of mathematics to medical problems. *Proceedings of the Edinburgh Mathematical Society*, 40:98–130, 1926.

[90] D. Menendez, A. Inga, and M. A. Resnick. The expanding universe of p53 targets. *Nat. Rev. Cancer*, 9(10):724–737, Oct 2009.

[91] C. Mertens, M. Zhong, R. Krishnaraj, W. Zou, X. Chen, and J. E. Darnell. Dephosphorylation of phosphotyrosine on STAT1 dimers requires extensive spatial reorientation of the monomers facilitated by the N-terminal domain. *Genes Dev.*, 20(24):3372–3381, Dec 2006.

[92] Nicholas Metropolis, Arianna W. Rosenbluth, Marshall N. Rosenbluth, Augusta H. Teller, and Edward Teller. Equation of state calculations by fast computing machines. *Journal of Chemical Physics*, 21:1087–1092, 1953.

[93] Nicholas Metropolis and S. Ulam. The Monte Carlo method. *j-J-AM-STAT-ASSOC*, 44(247):335–341, September 1949.

[94] T. Meyer, A. Begitt, I. Lodige, M. van Rossum, and U. Vinkemeier. Constitutive and IFN-gamma-induced nuclear import of STAT1 proceed through independent pathways. *EMBO J.*, 21(3):344–354, Feb 2002.

[95] T. Meyer, A. Marg, P. Lemke, B. Wiesner, and U. Vinkemeier. DNA binding controls inactivation and nuclear accumulation of the transcription factor Stat1. *Genes Dev.*, 17(16):1992–2005, Aug 2003.

[96] V. Minard, O. Hartmann, M. C. Peyroulet, J. Michon, C. Coze, A. S. Defachelle, O. Lejars, Y. Perel, C. Bergeron, P. Boutard, G. Leverger, J. L. Stephan, A. Thyss, P. Chastagner, G. Couillault, C. Devalck, P. Lutz, F. Mechinaud, F. Millot, D. Plantaz, X. Rialland, and H. Rubie. Adverse outcome of infants with metastatic neuroblastoma, MYCN amplification and/or bone lesions: results of the French society of pediatric oncology. *Br. J. Cancer*, 83(8):973–979, Oct 2000.

[97] W. Mo, L. Zhang, G. Yang, J. Zhai, Z. Hu, Y. Chen, X. Chen, L. Hui, R. Huang, and G. Hu. Nuclear beta-arrestin1 functions as a scaffold for the dephosphorylation of STAT1 and moderates the antiviral activity of IFN-gamma. *Mol. Cell*, 31(5):695–707, Sep 2008.

[98] D. Muth, S. Ghazaryan, I. Eckerle, E. Beckett, C. Pohler, J. Batzler, C. Beisel, S. Gogolin, M. Fischer, K. O. Henrich, V. Ehemann, P. Gillespie, M. Schwab, and F. Westermann. Transcriptional repression of SKP2 is impaired in MYCN-amplified neuroblastoma. *Cancer Res.*, 70(9):3791–3802, May 2010.

[99] Z. Nahle, J. Polakoff, R. V. Davuluri, M. E. McCurrach, M. D. Jacobson, M. Narita, M. Q. Zhang, Y. Lazebnik, D. Bar-Sagi, and S. W. Lowe. Direct coupling of the cell cycle and cell death machinery by E2F. *Nat. Cell Biol.*, 4(11):859–864, Nov 2002.

[100] K. Nakano and K. H. Vousden. PUMA, a novel proapoptotic gene, is induced by p53. *Mol. Cell*, 7(3):683–694, Mar 2001.

[101] V. Nandakumar, L. Kelbauskas, R. Johnson, and D. Meldrum. Quantitative characterization of preneoplastic progression using single-cell computed tomography and three-dimensional karyometry. *Cytometry A*, 79(1):25–34, Jan 2011.

[102] J. Nardozzi, N. Wenta, N. Yasuhara, U. Vinkemeier, and G. Cingolani. Molecular basis for the recognition of phosphorylated STAT1 by importin alpha5. *J. Mol. Biol.*, 402(1):83–100, Sep 2010.

[103] J. R. Nevins. Transcriptional regulation. A closer look at E2F. *Nature*, 358(6385):375–376, Jul 1992.

[104] J. R. Nevins. The Rb/E2F pathway and cancer. *Hum. Mol. Genet.*, 10(7):699–703, Apr 2001.

[105] I. Nicoletti, G. Migliorati, M. C. Pagliacci, F. Grignani, and C. Riccardi. A rapid and simple method for measuring thymocyte apoptosis by propidium iodide staining and flow cytometry. *J. Immunol. Methods*, 139(2):271–279, Jun 1991.

[106] B. Novak and J. J. Tyson. A model for restriction point control of the mammalian cell cycle. *J. Theor. Biol.*, 230(4):563–579, Oct 2004.

[107] J. J. O'Shea, M. Gadina, and R. D. Schreiber. Cytokine signaling in 2002: new surprises in the Jak/Stat pathway. *Cell*, 109 Suppl:S121–131, Apr 2002.

[108] A. B. Pardee. G1 events and regulation of cell proliferation. *Science*, 246(4930):603–608, Nov 1989.

[109] P. H. Peskun. Optimum Monte-Carlo Sampling Using Markov Chains. *Biometrika*, 60(3):607–612, December 1973.

[110] K. I. Pishas, F. Al-Ejeh, I. Zinonos, R. Kumar, A. Evdokiou, M. P. Brown, D. F. Callen, and P. M. Neilsen. Nutlin-3a is a potential therapeutic for ewing sarcoma. *Clin. Cancer Res.*, 17(3):494–504, Feb 2011.

[111] J. Pritchard and J. A. Hickman. Why does stage 4s neuroblastoma regress spontaneously? *Lancet*, 344(8926):869–870, Sep 1994.

[112] E. V. Prochownik and Y. Li. The ever expanding role for c-Myc in promoting genomic instability. *Cell Cycle*, 6(9):1024–1029, May 2007.

[113] C. J. Proctor and D. A. Gray. Explaining oscillations and variability in the p53-Mdm2 system. *BMC Syst Biol*, 2:75, 2008.

[114] M. Quigley, X. Huang, and Y. Yang. STAT1 signaling in CD8 T cells is required for their clonal expansion and memory formation following viral infection in vivo. *J. Immunol.*, 180(4):2158–2164, Feb 2008.

[115] S. Rajagopalan, F. Huang, and A. R. Fersht. Single-Molecule characterization of oligomerization kinetics and equilibria of the tumor suppressor p53. *Nucleic Acids Res.*, 39(6):2294–2303, Mar 2011.

[116] S. Ramalingam, P. Honkanen, L. Young, T. Shimura, J. Austin, P. S. Steeg, and S. Nishizuka. Quantitative assessment of the p53-Mdm2 feedback loop using protein lysate microarrays. *Cancer Res.*, 67(13):6247–6252, Jul 2007.

[117] K. Rohr, W. J. Godinez, N. Harder, S. Worz, J. Mattes, W. Tvarusko, and R. Eils. Tracking and quantitative analysis of dynamic movements of cells and particles. *Cold Spring Harb Protoc*, 2010(6):pdb.top80, Jun 2010.

[118] S. M. Rubin, A. L. Gall, N. Zheng, and N. P. Pavletich. Structure of the Rb C-terminal domain bound to E2F1-DP1: a mechanism for phosphorylation-induced E2F release. *Cell*, 123(6):1093–1106, Dec 2005.

[119] A. Sakaue-Sawano, H. Kurokawa, T. Morimura, A. Hanyu, H. Hama, H. Osawa, S. Kashiwagi, K. Fukami, T. Miyata, H. Miyoshi, T. Imamura, M. Ogawa, H. Masai, and A. Miyawaki. Visualizing spatiotemporal dynamics of multicellular cell-cycle progression. *Cell*, 132(3):487–498, Feb 2008.

[120] C. Schindler, K. Shuai, V. R. Prezioso, and J. E. Darnell. Interferon-dependent tyrosine phosphorylation of a latent cytoplasmic transcription factor. *Science*, 257(5071):809–813, Aug 1992.

[121] B. Schmierer, A. L. Tournier, P. A. Bates, and C. S. Hill. Mathematical modeling identifies Smad nucleocytoplasmic shuttling as a dynamic signal-interpreting system. *Proc. Natl. Acad. Sci. U.S.A.*, 105(18):6608–6613, May 2008.

[122] A. Schramm, J. Koster, T. Marschall, M. Martin, M. Heilmann, K. Fielitz, G. Buchel, M. Barann, D. Esser, P. Rosenstiel, S. Rahmann, A. Eggert, and J. H. Schulte. Next-generation RNA sequencing reveals differential expression of MYCN target genes and suggests the mTOR pathway as a promising therapy target in MYCN-amplified neuroblastoma. *Int. J. Cancer*, Aug 2012.

[123] M. Schwab, K. Alitalo, K. H. Klempnauer, H. E. Varmus, J. M. Bishop, F. Gilbert, G. Brodeur, M. Goldstein, and J. Trent. Amplified DNA with limited homology to myc cellular oncogene is shared by human neuroblastoma cell lines and a neuroblastoma tumour. *Nature*, 305(5931):245–248, 1983.

[124] T. Sekimoto, N. Imamoto, K. Nakajima, T. Hirano, and Y. Yoneda. Extracellular signal-dependent nuclear import of Stat1 is mediated by nuclear pore-targeting complex formation with NPI-1, but not Rch1. *EMBO J.*, 16(23):7067–7077, Dec 1997.

[125] S. Y. Shieh, M. Ikeda, Y. Taya, and C. Prives. DNA damage-induced phosphorylation of p53 alleviates inhibition by MDM2. *Cell*, 91(3):325–334, Oct 1997.

[126] K. Shuai, C. M. Horvath, L. H. Huang, S. A. Qureshi, D. Cowburn, and J. E. Darnell. Interferon activation of the transcription factor Stat91 involves dimerization through SH2-phosphotyrosyl peptide interactions. *Cell*, 76(5):821–828, Mar 1994.

[127] K. Shuai and B. Liu. Regulation of JAK-STAT signalling in the immune system. *Nat. Rev. Immunol.*, 3(11):900–911, Nov 2003.

[128] A. Shvarts, W. T. Steegenga, N. Riteco, T. van Laar, P. Dekker, M. Bazuine, R. C. van Ham, W. van der Houven van Oordt, G. Hateboer, A. J. van der Eb, and A. G. Jochemsen. MDMX: a novel p53-binding protein with some functional properties of MDM2. *EMBO J.*, 15(19):5349–5357, Oct 1996.

[129] A. Slack, Z. Chen, R. Tonelli, M. Pule, L. Hunt, A. Pession, and J. M. Shohet. The p53 regulatory gene MDM2 is a direct transcriptional target of MYCN in neuroblastoma. *Proc. Natl. Acad. Sci. U.S.A.*, 102(3):731–736, Jan 2005.

[130] R. P. Soebiyanto, S. N. Sreenath, C. K. Qu, K. A. Loparo, and K. D. Bunting. Complex systems biology approach to understanding coordination of JAK-STAT signaling. *BioSystems*, 90(3):830–842, 2007.

[131] G. R. Stark and J. E. Darnell. The JAK-STAT pathway at twenty. *Immunity*, 36(4):503–514, Apr 2012.

[132] J. E. Stenger, G. A. Mayr, K. Mann, and P. Tegtmeyer. Formation of stable p53 homotetramers and multiples of tetramers. *Mol. Carcinog.*, 5(2):102–106, 1992.

[133] J. D. Stone, J. R. Cochran, and L. J. Stern. T-cell activation by soluble MHC oligomers can be described by a two-parameter binding model. *Biophys. J.*, 81(5):2547–2557, Nov 2001.

[134] R. Suryadinata, M. Sadowski, R. Steel, and B. Sarcevic. Cyclin-dependent kinase-mediated phosphorylation of RBP1 and pRb promotes their dissociation to mediate release of the SAP30mSin3HDAC transcriptional repressor complex. *J. Biol. Chem.*, 286(7):5108–5118, Feb 2011.

[135] I. Swameye, T. G. Muller, J. Timmer, O. Sandra, and U. Klingmuller. Identification of nucleocytoplasmic cycling as a remote sensor in cellular signaling by databased modeling. *Proc. Natl. Acad. Sci. U.S.A.*, 100(3):1028–1033, Feb 2003.

[136] T. Takaki, K. Fukasawa, I. Suzuki-Takahashi, and H. Hirai. Cdk-mediated phosphorylation of pRB regulates HDAC binding in vitro. *Biochem. Biophys. Res. Commun.*, 316(1):252–255, Mar 2004.

[137] T. Tanaka, M. A. Soriano, and M. J. Grusby. SLIM is a nuclear ubiquitin E3 ligase that negatively regulates STAT signaling. *Immunity*, 22(6):729–736, Jun 2005.

[138] S. Taubert, C. Gorrini, S. R. Frank, T. Parisi, M. Fuchs, H. M. Chan, D. M. Livingston, and B. Amati. E2F-dependent histone acetylation and recruitment of the Tip60 acetyltransferase complex to chromatin in late G1. *Mol. Cell. Biol.*, 24(10):4546–4556, May 2004.

[139] J. ten Hoeve, M. de Jesus Ibarra-Sanchez, Y. Fu, W. Zhu, M. Tremblay, M. David, and K. Shuai. Identification of a nuclear Stat1 protein tyrosine phosphatase. *Mol. Cell. Biol.*, 22(16):5662–5668, Aug 2002.

[140] T. Tenev, S. A. Bohmer, R. Kaufmann, S. Frese, T. Bittorf, T. Beckers, and F. D. Bohmer. Perinuclear localization of the protein-tyrosine phosphatase SHP-1 and inhibition of epidermal growth factor-stimulated STAT1/3 activation in A431 cells. *Eur. J. Cell Biol.*, 79(4):261–271, Apr 2000.

[141] J. J. Tumilowicz, W. W. Nichols, J. J. Cholon, and A. E. Greene. Definition of a continuous human cell line derived from neuroblastoma. *Cancer Res.*, 30(8):2110–2118, Aug 1970.

[142] D. A. Tweddle, A. D. Pearson, M. Haber, M. D. Norris, C. Xue, C. Flemming, and J. Lunec. The p53 pathway and its inactivation in neuroblastoma. *Cancer Lett.*, 197(1-2):93–98, Jul 2003.

[143] D. Ungureanu, S. Vanhatupa, J. Gronholm, J. J. Palvimo, and O. Silvennoinen. SUMO-1 conjugation selectively modulates STAT1-mediated gene responses. *Blood*, 106(1):224–226, Jul 2005.

[144] T. Van Maerken, L. Ferdinande, J. Taildeman, I. Lambertz, N. Yigit, L. Vercruysse, A. Rihani, M. Michaelis, J. Cinatl, C. A. Cuvelier, J. C. Marine, A. De Paepe, M. Bracke, F. Speleman, and J. Vandesompele. Antitumor activity of the selective MDM2 antagonist nutlin-3 against chemoresistant neuroblastoma with wild-type p53. *J. Natl. Cancer Inst.*, 101(22):1562–1574, Nov 2009.

[145] T. Van Maerken, A. Rihani, D. Dreidax, S. De Clercq, N. Yigit, J. C. Marine, F. Westermann, A. De Paepe, J. Vandesompele, and F. Speleman. Functional analysis of the p53 pathway in neuroblastoma cells using the small-molecule MDM2 antagonist nutlin-3. *Mol. Cancer Ther.*, 10(6):983–993, Jun 2011.

[146] T. Van Maerken, F. Speleman, J. Vermeulen, I. Lambertz, S. De Clercq, E. De Smet, N. Yigit, V. Coppens, J. Philippe, A. De Paepe, J. C. Marine, and J. Vandesompele. Small-molecule MDM2 antagonists as a new therapy concept for neuroblastoma. *Cancer Res.*, 66(19):9646–9655, Oct 2006.

[147] T. Van Maerken, J. Vandesompele, A. Rihani, A. De Paepe, and F. Speleman. Escape from p53-mediated tumor surveillance in neuroblastoma: switching off the p14(ARF)-MDM2-p53 axis. *Cell Death Differ.*, 16(12):1563–1572, Dec 2009.

[148] S. Vanhatupa, D. Ungureanu, M. Paakkunainen, and O. Silvennoinen. MAPK-induced Ser727 phosphorylation promotes SUMOylation of STAT1. *Biochem. J.*, 409(1):179–185, Jan 2008.

[149] K. Vermeulen, Z. N. Berneman, and D. R. Van Bockstaele. Cell cycle and apoptosis. *Cell Prolif.*, 36(3):165–175, Jun 2003.

[150] U. Vinkemeier. Getting the message across, STAT! Design principles of a molecular signaling circuit. *J. Cell Biol.*, 167(2):197–201, Oct 2004.

[151] U. Vinkemeier, S. L. Cohen, I. Moarefi, B. T. Chait, J. Kuriyan, and J. E. Darnell. DNA binding of in vitro activated Stat1 alpha, Stat1 beta and trun-

cated Stat1: interaction between NH2-terminal domains stabilizes binding of two dimers to tandem DNA sites. *EMBO J.*, 15(20):5616–5626, Oct 1996.

[152] B. Vogelstein, D. Lane, and A. J. Levine. Surfing the p53 network. *Nature*, 408(6810):307–310, Nov 2000.

[153] H. von Foerster. Some Remarks on Changing Populations. In J. F. Stohlman, editor, *The Kinetics of Cellular Proliferation*, pages 382–407. Grune and Stratton, New York, 1959.

[154] R. A. Weinberg. The retinoblastoma protein and cell cycle control. *Cell*, 81(3):323–330, May 1995.

[155] Robert A. Weinberg. *The Biology of Cancer HB*. Garland Science, 1 edition, June 2006.

[156] N. Wenta, H. Strauss, S. Meyer, and U. Vinkemeier. Tyrosine phosphorylation regulates the partitioning of STAT1 between different dimer conformations. *Proc. Natl. Acad. Sci. U.S.A.*, 105(27):9238–9243, Jul 2008.

[157] F. Westermann, D. Dreidax, S. Gogolin, F. Lamprecht, S. Bannert, D. Muth, and M. Zapatka. Functional synergy between cdk4 and mdm2 in mycn/c-myc-driven malignant progression of human neuroblastomas. *in preparation.*

[158] F. Westermann, K. O. Henrich, J. S. Wei, W. Lutz, M. Fischer, R. Konig, R. Wiedemeyer, V. Ehemann, B. Brors, K. Ernestus, I. Leuschner, A. Benner, J. Khan, and M. Schwab. High Skp2 expression characterizes high-risk neuroblastomas independent of MYCN status. *Clin. Cancer Res.*, 13(16):4695–4703, Aug 2007.

[159] F. Westermann, D. Muth, A. Benner, T. Bauer, K. O. Henrich, A. Oberthuer, B. Brors, T. Beissbarth, J. Vandesompele, F. Pattyn, B. Hero, R. Konig, M. Fischer, and M. Schwab. Distinct transcriptional MYCN/c-MYC activities are associated with spontaneous regression or malignant progression in neuroblastomas. *Genome Biol.*, 9(10):R150, 2008.

[160] F. Westermann and M. Schwab. Genetic parameters of neuroblastomas. *Cancer Lett.*, 184(2):127–147, Oct 2002.

[161] J. V. Wong, P. Dong, J. R. Nevins, B. Mathey-Prevot, and L. You. Network calisthenics: control of E2F dynamics in cell cycle entry. *Cell Cycle*, 10(18):3086–3094, Sep 2011.

[162] L. Xue, Y. Sun, L. Chiang, B. He, C. Kang, H. Nolla, and A. Winoto. Coupling of the cell cycle and apoptotic machineries in developing T cells. *J. Biol. Chem.*, 285(10):7556–7565, Mar 2010.

[163] E. Yang, M. A. Henriksen, O. Schaefer, N. Zakharova, and J. E. Darnell. Dissociation time from DNA determines transcriptional function in a STAT1 linker mutant. *J. Biol. Chem.*, 277(16):13455–13462, Apr 2002.

[164] G. Yao, T. J. Lee, S. Mori, J. R. Nevins, and L. You. A bistable Rb-E2F switch underlies the restriction point. *Nat. Cell Biol.*, 10(4):476–482, Apr 2008.

[165] J. Yu, L. Zhang, P. M. Hwang, K. W. Kinzler, and B. Vogelstein. PUMA induces the rapid apoptosis of colorectal cancer cells. *Mol. Cell*, 7(3):673–682, Mar 2001.

[166] A. Zetterberg and O. Larsson. Kinetic analysis of regulatory events in G1 leading to proliferation or quiescence of Swiss 3T3 cells. *Proc. Natl. Acad. Sci. U.S.A.*, 82(16):5365–5369, Aug 1985.

[167] C. Zhang and S. H. Kim. The effect of dynamic receptor clustering on the sensitivity of biochemical signaling. *Pac Symp Biocomput*, pages 353–364, 2000.

[168] Z. Zi, K. H. Cho, M. H. Sung, X. Xia, J. Zheng, and Z. Sun. In silico identification of the key components and steps in IFN-gamma induced JAK-STAT signaling pathway. *FEBS Lett.*, 579(5):1101–1108, Feb 2005.

[169] A. Zilman, V. V. Ganusov, and A. S. Perelson. Stochastic models of lymphocyte proliferation and death. *PLoS ONE*, 5(9), 2010.

A Appendix

A.1 JAK/STAT1 model equations parameter values

$$
\begin{aligned}
\partial_t [R] &= k_2 [R^*] - k_1 [R] - k_3 [R] \\
\partial_t [R^*] &= k_1 [R] + (k_{-4} + k_5) ([R^* S] + [R^* SS] + [R^* S^{\mathrm{p}} S]) \\
&\quad -k_2 [R^*] - k_3 [R^*] - k_4 [R^*] \left([S_{\mathrm{cyt}}] + \left[S S^{\mathrm{NN}}_{\mathrm{cyt}}\right] + \left[S^{\mathrm{p}} S^{\mathrm{NN}}_{\mathrm{cyt}}\right]\right) \\
\partial_t [R^* S] &= k_4 [R^*] [S_{\mathrm{cyt}}] - k_{-4} [R^* S] - k_5 [R^* S] \\
\partial_t [R^* SS] &= k_4 [R^*] \left[S S^{\mathrm{NN}}_{\mathrm{cyt}}\right] - k_{-4} [R^* SS] - k_5 [R^* SS] \\
\partial_t [R^* S^{\mathrm{p}} S] &= k_4 [R^*] \left[S^{\mathrm{p}} S^{\mathrm{NN}}_{\mathrm{cyt}}\right] - k_{-4} [R^* S^{\mathrm{p}} S] - k_5 [R^* S^{\mathrm{p}} S] \\
\partial_t [S_{\mathrm{cyt}}] &= k_{-4} [R^* S] + k_7 \left[S^{\mathrm{p}}_{\mathrm{cyt}}\right] + (k_{12a} + k_{12b}) [S_{\mathrm{nuc}}] + 2\ k_{14} \left[S S^{\mathrm{NN}}_{\mathrm{cyt}}\right] + k_{14} \left[S^{\mathrm{p}} S^{\mathrm{NN}}_{\mathrm{cyt}}\right] \\
&\quad -k_4 [R^*] [S_{\mathrm{cyt}}] - k_{13} [S_{\mathrm{cyt}}] - 2\ k_{14} [S_{\mathrm{cyt}}]^2 - k_{14} [S_{\mathrm{cyt}}] \left[S^{\mathrm{p}}_{\mathrm{cyt}}\right] \\
\partial_t \left[S^{\mathrm{p}}_{\mathrm{cyt}}\right] &= k_5 [R^* S] + 2\ k_{-6} \left[S^{\mathrm{pp}} S^{\mathrm{SH2}}_{\mathrm{cyt}}\right] + 2\ k_{-14} \left[S^{\mathrm{pp}} S^{\mathrm{NN}}_{\mathrm{cyt}}\right] + k_{-14} \left[S^{\mathrm{p}} S^{\mathrm{NN}}_{\mathrm{cyt}}\right] \\
&\quad -2\ k_6 \left[S^{\mathrm{p}}_{\mathrm{cyt}}\right]^2 - k_7 \left[S^{\mathrm{p}}_{\mathrm{cyt}}\right] - 2\ k_{14} \left[S^{\mathrm{p}}_{\mathrm{cyt}}\right]^2 - k_{14} [S_{\mathrm{cyt}}] \left[S^{\mathrm{p}}_{\mathrm{cyt}}\right] \\
\partial_t \left[S^{\mathrm{pp}} S^{\mathrm{SH2}}_{\mathrm{cyt}}\right] &= k_6 \left[S^{\mathrm{p}}_{\mathrm{cyt}}\right]^2 - k_{-6} \left[S^{\mathrm{pp}} S^{\mathrm{SH2}}_{\mathrm{cyt}}\right] - k_8 \left[S^{\mathrm{pp}} S^{\mathrm{SH2}}_{\mathrm{cyt}}\right] \\
\partial_t \left[S S^{\mathrm{NN}}_{\mathrm{cyt}}\right] &= k_{-4} [R^* SS] + k_7 \left[S^{\mathrm{p}} S^{\mathrm{NN}}_{\mathrm{cyt}}\right] + (k_{12a} + k_{12b}) \left[S S^{\mathrm{NN}}_{\mathrm{nuc}}\right] + k_{14} [S_{\mathrm{cyt}}]^2 \\
&\quad -k_4 [R^*] \left[S S^{\mathrm{NN}}_{\mathrm{cyt}}\right] - k_{13} \left[S S^{\mathrm{NN}}_{\mathrm{cyt}}\right] - k_{-14} \left[S S^{\mathrm{NN}}_{\mathrm{cyt}}\right] \\
\partial_t \left[S^{\mathrm{p}} S^{\mathrm{NN}}_{\mathrm{cyt}}\right] &= k_{-4} [R^* S^{\mathrm{p}} S] + k_5 [R^* SS] + k_7 \left[S^{\mathrm{pp}} S^{\mathrm{NN}}_{\mathrm{cyt}}\right] + k_{14} [S_{\mathrm{cyt}}] \left[S^{\mathrm{p}}_{\mathrm{cyt}}\right] \\
&\quad -k_4 [R^*] \left[S^{\mathrm{p}} S^{\mathrm{NN}}_{\mathrm{cyt}}\right] - k_7 \left[S^{\mathrm{p}} S^{\mathrm{NN}}_{\mathrm{cyt}}\right] - k_{-14} \left[S^{\mathrm{p}} S^{\mathrm{NN}}_{\mathrm{cyt}}\right] \\
\partial_t \left[S^{\mathrm{pp}} S^{\mathrm{NN}}_{\mathrm{cyt}}\right] &= k_5 [R^* S^{\mathrm{p}} S] + k_{14} \left[S^{\mathrm{p}}_{\mathrm{cyt}}\right]^2 - k_7 \left[S^{\mathrm{pp}} S^{\mathrm{NN}}_{\mathrm{cyt}}\right] - k_{-14} \left[S^{\mathrm{pp}} S^{\mathrm{NN}}_{\mathrm{cyt}}\right] \\
\partial_t \left[S^{\mathrm{pp}} S^{\mathrm{SH2}}_{\mathrm{nuc}}\right] &= k_6 [S^{\mathrm{p}}_{\mathrm{nuc}}]^2 + \rho\ k_8 \left[S^{\mathrm{pp}} S^{\mathrm{SH2}}_{\mathrm{cyt}}\right] + k_{-9} [D_{\mathrm{S}}] + k_{-10} [D_{\mathrm{U}}] \\
&\quad -k_{-6} \left[S^{\mathrm{pp}} S^{\mathrm{SH2}}_{\mathrm{nuc}}\right] - k_9 (gas - [D_{\mathrm{S}}]) \left[S^{\mathrm{pp}} S^{\mathrm{SH2}}_{\mathrm{nuc}}\right] - k_{10} \left[S^{\mathrm{pp}} S^{\mathrm{SH2}}_{\mathrm{nuc}}\right] \\
\partial_t [D_{\mathrm{S}}] &= k_9 (gas - [D_{\mathrm{S}}]) \left[S^{\mathrm{pp}} S^{\mathrm{SH2}}_{\mathrm{nuc}}\right] - k_{-9} [D_{\mathrm{S}}] \\
\partial_t [D_{\mathrm{U}}] &= k_{10} \left[S^{\mathrm{pp}} S^{\mathrm{SH2}}_{\mathrm{nuc}}\right] - k_{-10} [D_{\mathrm{U}}] \\
\partial_t [S^{\mathrm{p}}_{\mathrm{nuc}}] &= 2\ k_{-6} \left[S^{\mathrm{pp}} S^{\mathrm{SH2}}_{\mathrm{nuc}}\right] + 2\ k_{-14} \left[S^{\mathrm{pp}} S^{\mathrm{NN}}_{\mathrm{nuc}}\right] + k_{-14} \left[S^{\mathrm{p}} S^{\mathrm{NN}}_{\mathrm{nuc}}\right] \\
&\quad -2\ k_6 [S^{\mathrm{p}}_{\mathrm{nuc}}]^2 - k_{11} [S^{\mathrm{p}}_{\mathrm{nuc}}] - 2\ k_{14} [S^{\mathrm{p}}_{\mathrm{nuc}}]^2 - k_{14} [S_{\mathrm{nuc}}] [S^{\mathrm{p}}_{\mathrm{nuc}}] \\
\partial_t [S_{\mathrm{nuc}}] &= k_{11} [S^{\mathrm{p}}_{\mathrm{nuc}}] + \rho\ k_{13} [S_{\mathrm{nuc}}] + 2\ k_{14} \left[S S^{\mathrm{NN}}_{\mathrm{nuc}}\right] + k_{14} \left[S^{\mathrm{p}} S^{\mathrm{NN}}_{\mathrm{nuc}}\right] \\
&\quad -\rho\ (k_{12a} + k_{12b}) [S_{\mathrm{nuc}}] - 2\ k_{14} [S_{\mathrm{nuc}}]^2 - k_{14} [S_{\mathrm{nuc}}] [S^{\mathrm{p}}_{\mathrm{nuc}}] \\
\partial_t \left[S S^{\mathrm{NN}}_{\mathrm{nuc}}\right] &= k_{11} \left[S^{\mathrm{p}} S^{\mathrm{NN}}_{\mathrm{nuc}}\right] + \rho\ k_{13} \left[S S^{\mathrm{NN}}_{\mathrm{cyt}}\right] + k_{14} [S_{\mathrm{nuc}}]^2 \\
&\quad -\rho\ (k_{12a} + k_{12b}) \left[S S^{\mathrm{NN}}_{\mathrm{nuc}}\right] - k_{-14} \left[S S^{\mathrm{NN}}_{\mathrm{nuc}}\right] \\
\partial_t \left[S^{\mathrm{p}} S^{\mathrm{NN}}_{\mathrm{nuc}}\right] &= k_{11} \left[S^{\mathrm{pp}} S^{\mathrm{NN}}_{\mathrm{nuc}}\right] + k_{14} [S_{\mathrm{nuc}}] [S^{\mathrm{p}}_{\mathrm{nuc}}] \\
&\quad -k_{11} \left[S^{\mathrm{p}} S^{\mathrm{NN}}_{\mathrm{nuc}}\right] - k_{-14} \left[S^{\mathrm{p}} S^{\mathrm{NN}}_{\mathrm{nuc}}\right] \\
\partial_t \left[S^{\mathrm{pp}} S^{\mathrm{NN}}_{\mathrm{nuc}}\right] &= k_{14} [S^{\mathrm{p}}_{\mathrm{nuc}}]^2 - k_{11} \left[S^{\mathrm{pp}} S^{\mathrm{NN}}_{\mathrm{nuc}}\right] - k_{-14} \left[S^{\mathrm{pp}} S^{\mathrm{NN}}_{\mathrm{nuc}}\right].
\end{aligned}
$$

We considered cytoplasmic (subscript cyt) and nuclear (subscript nuc) species of monomeric STAT1 proteins (S) and of STAT1 homodimers (SS) . The superscript p indicates a tyrosine phosphorylation (two superscripts indicating that both Stats are phosphorylated). The dimer binding is either by N-terminal interactions (superscript NN) or by phospho-tyrosine/SH2 domain interactions (superscript SH2). The receptors can be inactive (R) or activated (R^*), where the activated receptors can bind unphosphorylated STAT1 monomers (R^*S) and N-terminal STAT1 homodimers (R^*SS). The nuclear phospho-tyrosine/SH2 dimers can bind DNA specifically (D_S) by interaction with GAS-sites and unspecifically (D_U).

Reaction	**Para.**	**Value [95% confidence]**
Concentration of IFNγ receptors	R_0	5.3 nM $\approx 10^4$ receptors
Concentration of GAS sites	gas	5 nM $\approx 3 \cdot 10^3$ sites
Nucleo-cytoplasmic volume ratio	ρ	3 $(V_\mathrm{cyto}/V_\mathrm{nuc})$
Activation IFN receptor/JAK complex	k_1	0.056 $[0.049; 0.069]$ min^{-1}
Deactivation IFN receptor/JAK complex	k_2	1.9 $[0; 17] \cdot 10^{-3}$ min^{-1}
Receptor degradation	k_3	0.017 $[0.015; 0.018]$ min^{-1}
Binding STAT1 to receptor	k_4	0.02 min^{-1}nM^{-1}
Dissociation STAT1-receptor complex	k_{-4}	0.7 min^{-1}
STAT1 phosphorylation & dissociation	k_5	29 $[> 2]$ min^{-1}
Formation phospho-tyrosine/SH2 dimer	k_6	0.01 min^{-1}nM^{-1}
Dissociation SH2 dimer	k_{-6}	0.5 min^{-1}
Dephosphorylation in the cytoplasm	k_7	0.023 $[0.021; 0.025]$ min^{-1}
Nuclear import phospho-STAT1	k_8	1 min^{-1}
Binding STAT1 to GAS-site	k_9	0.06 min^{-1}nM^{-1}
Dissociation STAT1 from GAS-site	k_{-9}	0.05 min^{-1}
Unspecific binding STAT1 to DNA	k_{10}	2 min^{-1}
Dissociation STAT1 from DNA	k_{-10}	5 min^{-1}
Dephosphorylation in the nucleus	k_{11}	0.29 $[0.24; 0.37]$ min^{-1}
Energy independent nuclear export latent STAT1	k_{12a}	0.2 min^{-1}
CRM1 dependent nuclear export latent STAT1	k_{12b}	0.3 min^{-1}
Energy independent nuclear import latent STAT1	k_{13}	0.2 min^{-1}
Formation N-terminal dimer	k_{14}	0.02 min^{-1}nM^{-1}
Dissociation N-terminal dimer	k_{-14}	0.8 min^{-1}

Table A.1: The measured parameters and fitted values with 95% confidence intervals (given in brackets) used for the simulations.

A.2 Nuclear residence time of phospho-STAT1 from deterministic solution

From the deterministic solution we get the concentration flow of STAT1 from one state into another. For example the phospho-STAT1 concentration flow into the nucleus $\mathcal{F}_1$ is determined by the concentration of phospho-STAT1 SH2 dimers in the cytoplasm $S^{\mathrm{pp}} S^{\mathrm{SH2}}_{\mathrm{cyt}}$

$$\mathcal{F}_1 = \rho \; k_8 \; S^{\mathrm{pp}} S^{\mathrm{SH2}}_{\mathrm{nuc}}.$$

The concentration flow of nuclear dephosphorylation $\mathcal{F}_2$ is determined by the concentration of nuclear phopho-STAT1 monomers and N-terminal dimers

$$\mathcal{F}_2 = k_2 \left(S^{\mathrm{p}}_{\mathrm{nuc}} + S^{\mathrm{p}} S^{\mathrm{NN}}_{\mathrm{nuc}} + S^{\mathrm{pp}} S^{\mathrm{NN}}_{\mathrm{nuc}} \right).$$

From this we get the expected time of import T_1 and the expected time of dephosphorylation T_2 as

$$T_i = \langle \mathcal{F}_i \rangle = \frac{1}{\mathcal{N}} \int \mathcal{F}_i \cdot t \; dt.$$

For a standard stimulus we get $T_1 = 79.1$ min and $T_2 = 91.4$ min. If the dephosphorylation is independent from the import

$$\langle \mathcal{F}_2 - \mathcal{F}_2 \rangle = \langle \mathcal{F}_1 \rangle - \langle \mathcal{F}_2 \rangle$$

holds and the time spent in between import and dephosphorylation T_{12} would follow straight forward

$$T_{12} = T_2 - T_1.$$

This would give $T_{12} = 12.3$ min for our model. Due to the non-linearity of the dimer formation the dimerization is dependent on the STAT1 concentration and thereby on the import time. Because the time of dephosphorylation is dependent on the

	(i) deterministic	(ii) Fourier	(iii) stochastic
mean time in minutes	12.3	12.5	12.3
5 percentile in minutes	-	0.7	1.1
95 percentile in minutes	-	33	47.9

Table A.2: The mean time, the STAT1 molecules stayed activated in the nucleus (from import until dephosphorylation) deduced (i) from the deterministic solution by difference of the means (ii) by Fourier transform of the deterministic solution (iii) from stochastic simulation agree very well. The width of the distribution of the times measured by the 5 and 95 percentiles calculated by Fourier transform give the correct order of magnitude but are not very accurate (error $\sim 30\%$).

dimerization it is not independent of the import time and the deduced $T_{12} = 12.3$ min is biased by this correlation. However, a comparison with the stochastic simulation shows (main text, section 4.2; table A.2), that the deviation is smaller than 1 second. With the deterministic solution it is also possible to not only estimate the mean time of the proteins staying phosphorylated in the nucleus but also the distribution of times. This is given by the flow through the phosphorylated states in the nucleus $\mathcal{F}_{12}$. We use, that the flow of phospho-STAT1 into the nucleus $\mathcal{F}_1$ convoluted with the flow through the phosphorylated states in the nucleus $\mathcal{F}_{12}$ must yield the flow of dephosphorylation $\mathcal{F}_2 = \mathcal{F}_1 \circ \mathcal{F}_{12}$. By using a Fourier transformation, we can solve this equation for $\mathcal{F}_{12}$ and transform back. Due to numerical errors this just gives an approximation to the distribution simulated by the stochastic algorithm (figure A.1). The mean times agree quite well, but the width of the distribution deduced by the Fourier transformation is too small.

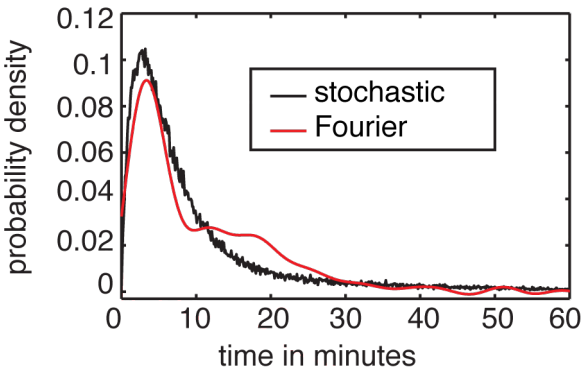

Figure A.1: Probability density for the residence time of phospho-STAT1 in the nucleus (until dephosphorylation) from the stochastic simulation (red line) and the deterministic simulation via fourier transform (black line).

A.3 Comparison of STAT1-WT and STAT1-NES transcriptional response of six genes

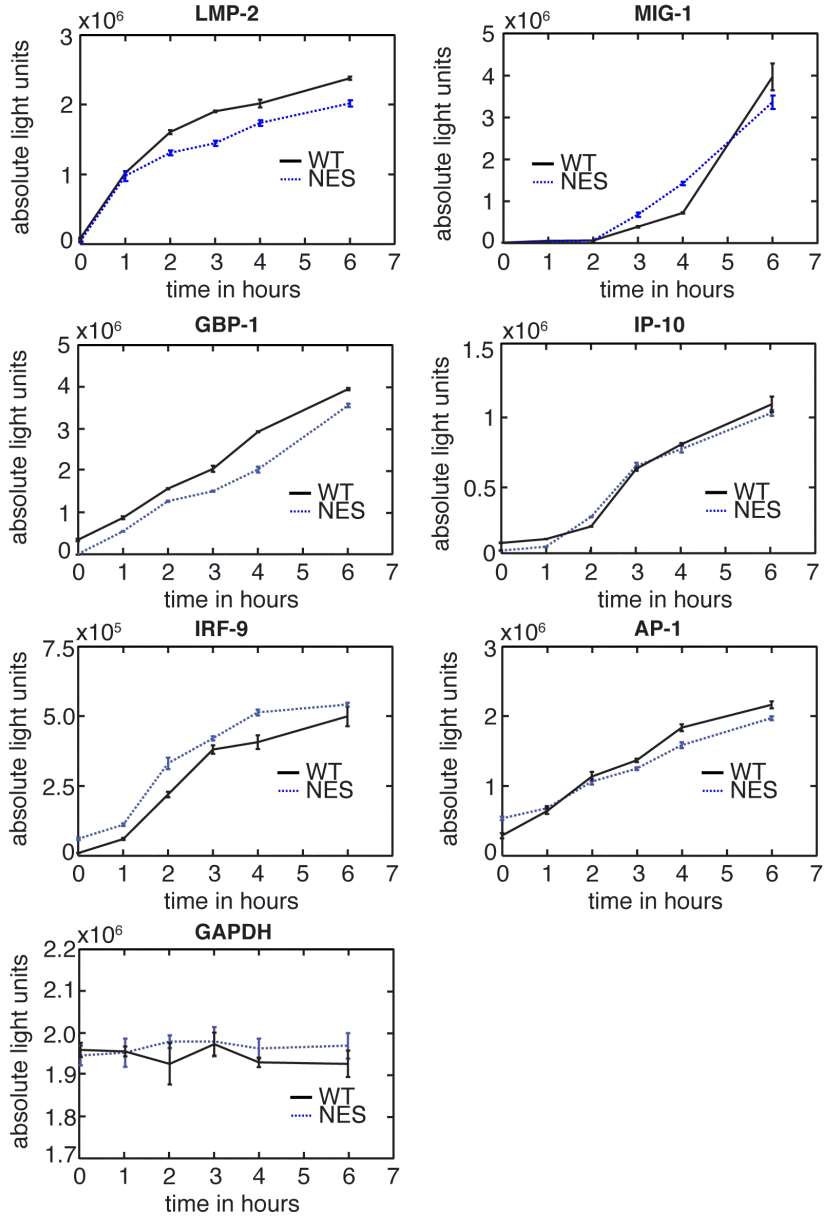

Figure A.2: Comparison of STAT1-WT and STAT1-NES transcriptional response of six STAT1 target genes.

A.4 Western blot experiments of doxorubicin treatment of conditionally MYCN knock down in IMR5-75 C2 cells

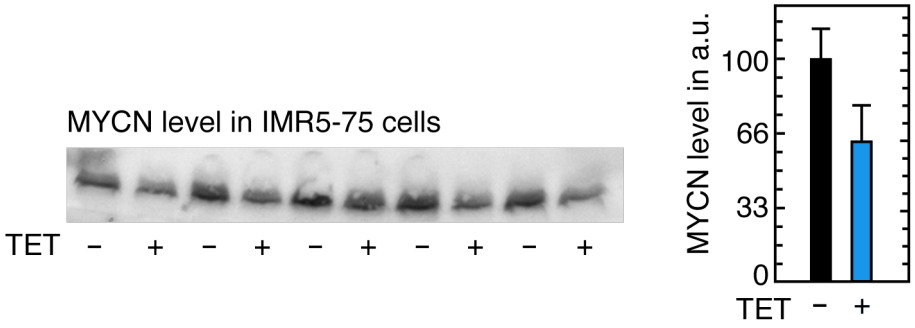

Figure A.3: MYCN knockdown efficiency of the IMR5-75 C2 cells harboring conditionally expressing MYCN siRNA under control of tetracycline measured by Western blot and quantified with ImageJ. The resulting knock down efficiency is $\sim 40\%$.

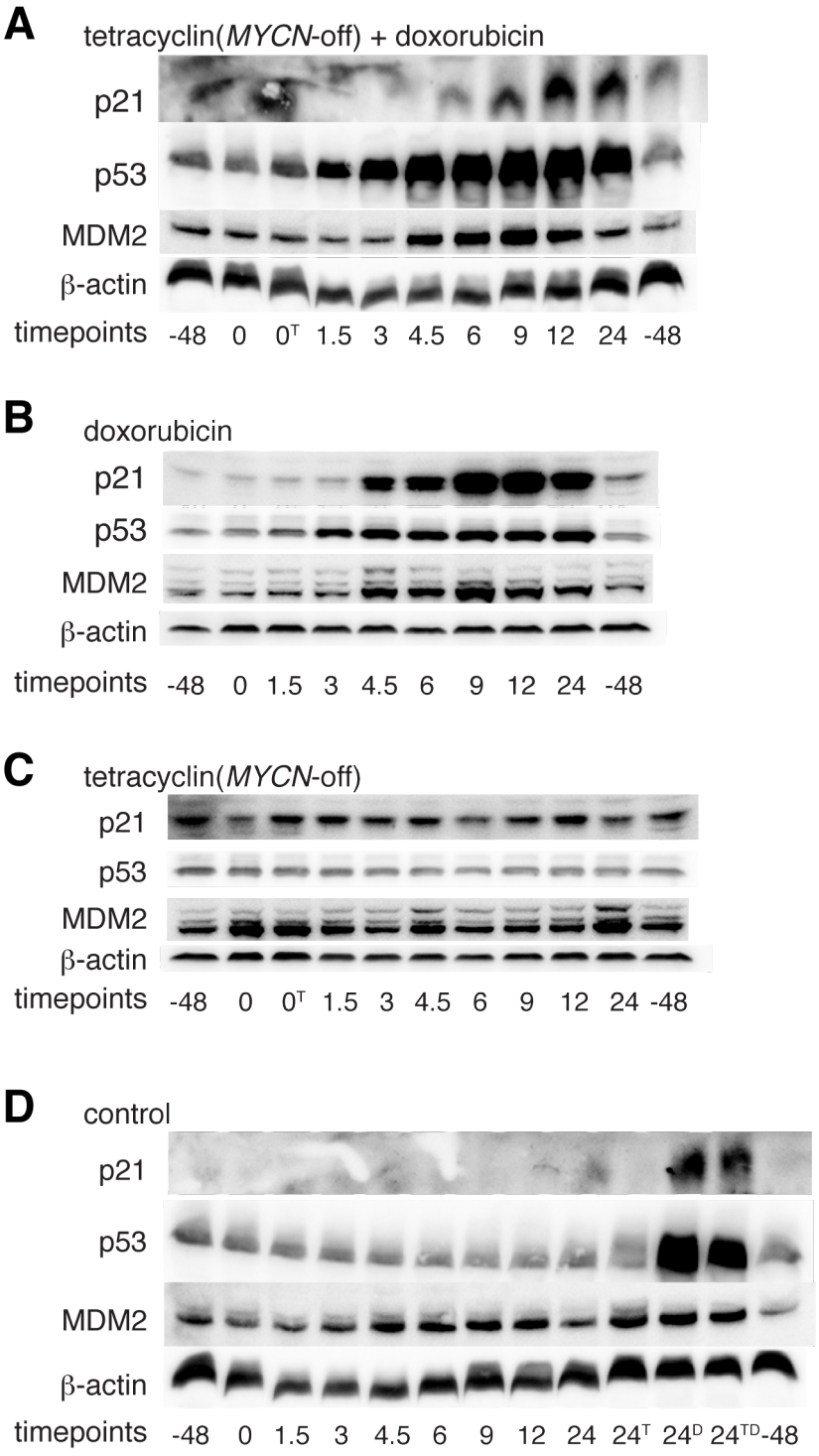

Figure A.4: Western blots for the protein quantification in the conditionally MYCN knockdown IMR5-75 cells under different conditions: (**A**) MYCN-off and doxorubicin (**B**) MYCN-on and doxorubicin (**C**) MYCN-off control (**D**) MYCN-on control.

A.5 p21mCherry plasmid

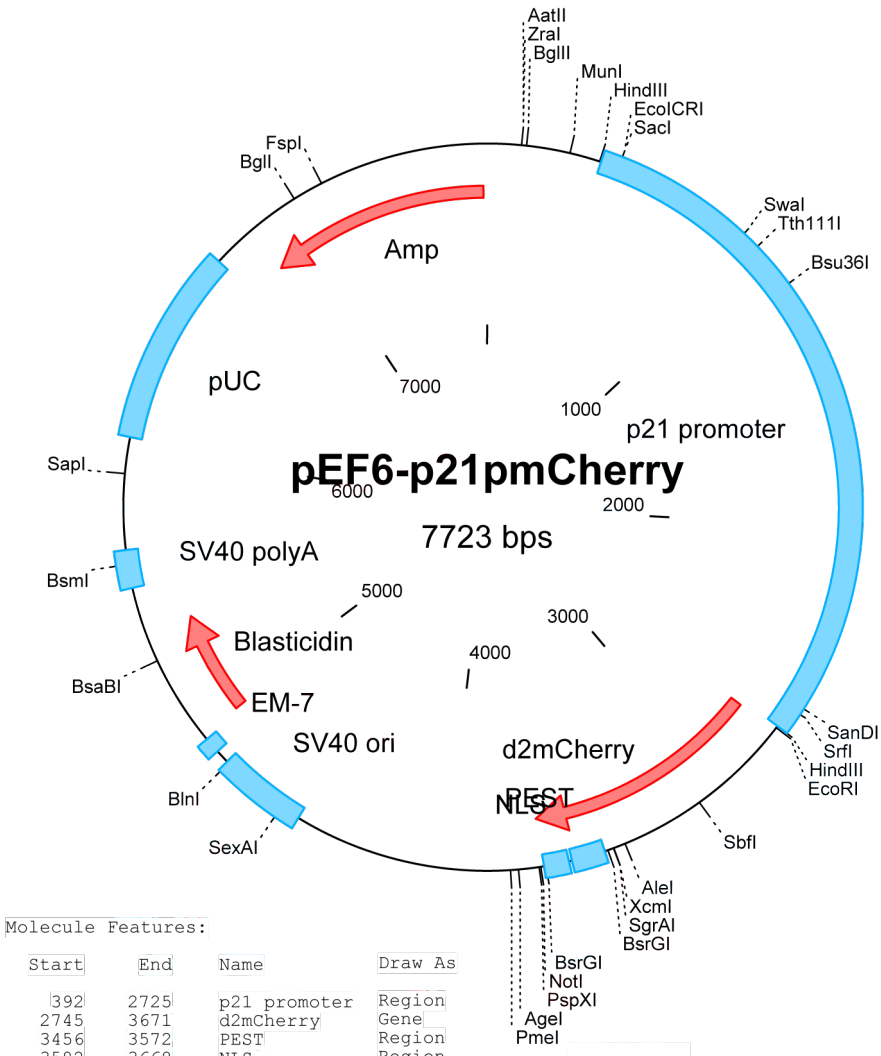

Molecule Features:

Start	End		Name	Draw As
392	2725		p21 promoter	Region
2745	3671		d2mCherry	Gene
3456	3572		PEST	Region
3582	3668		NLS	Region
4532	4840		SV40 ori	Region
4887	4942		EM-7	Region
4961	5359		Blasticidin	Gene
5517	5647		SV40 polyA	Region
6031	6704		pUC	Region
7709	6849	C	Amp	Gene

Enzymes (31 sites)

AatII	117,	ZraI	117,	BglII	134,	MunI	283
HindIII	387,	EcoICRI	453,	SacI	453,	SwaI	927
Tth111I	988,	Bsu36I	1146,	SanDI	2628,	SrfI	2650
HindIII	2725,	EcoRI	2732,	SbfI	3095,	AleI	3383
XcmI	3424,	SgrAI	3425,	BsrGI	3445,	BsrGI	3661
NotI	3679,	PspXI	3685,	AgeI	3755,	PmeI	3782
SexAI	4600,	BlnI	4833,	BsaBI	5256,	BsmI	5598
SapI	5906,	BglI	7036,	FspI	7142,		

Figure A.5: Map of the plasmid containing the p21 promoter driving mCherry, NLS and PEST.

A.6 equations p53 mRNA module

$$
\begin{aligned}
\partial_t\, x_1(t) &= k_{\mathrm{vx1}} - k_{\mathrm{dx1}}\, x_1(t) + k_{nx}\, n(t) \\
\partial_t\, x_2(t) &= k_{\mathrm{vx2}}\, x_1(t) - k_{\mathrm{dx2}}\, x_2(t) - \frac{k_{\mathrm{dxy}}}{u}\frac{x_2(t)\, y_2(t)}{k_{\mathrm{kx2}} + y_2(t)} - (k_{\mathrm{on}} + k_{\mathrm{dam}})\, x_2(t) + k_{\mathrm{off}}\, x_3(t) \\
\partial_t\, x_3(t) &= (k_{\mathrm{on}} + k_{\mathrm{dam}})\, x_2(t) - k_{\mathrm{off}}\, x_3(t) \\
\partial_t\, y_1(t) &= k_{\mathrm{vy1}} + k_{\mathrm{vyx}}\frac{x_3(t)^4}{(k_{\mathrm{ky1}} + x_3(t))^4} - k_{\mathrm{dy1}}\, y_1(t) + k_{\mathrm{ny}}\, n(t) \\
\partial_t\, y_2(t) &= k_{\mathrm{vy2}}\, y_1(t) - k_{dy2}\, y_2(t) \\
\partial_t\, z_1(t) &= k_{\mathrm{vz1}} + k_{\mathrm{vzx}}\frac{x_3(t)^4}{(k_{\mathrm{kz1}} + x_3(t))^4}\frac{1}{n(t)/k_{\mathrm{kz1n}} + 1} - k_{\mathrm{dz1}}\, z_1(t) \\
\partial_t z_2(t) &= k_{\mathrm{vz2}}\, z_1(t) - k_{\mathrm{dzy}}\, z_2(t)\frac{y_2(t)}{(z_2(t) + k_{\mathrm{kz2}})} - k_{\mathrm{dz2}}\, z_2(t) \\
\partial_t w(t) &= v_{\mathrm{w}} + v_{\mathrm{xw}}\left[\frac{x_3(t)}{K_{\mathrm{xw}} + x_3(t)}\right]^4 - \delta_{\mathrm{w}}\, w(t),
\end{aligned}
$$

with concentrations:

$x_1(t)$ p53 mRNA	$x_2(t)$ p53 protein	$x_3(t)$ active p53 protein
$y_1(t)$ MDM2 mRNA	$y_2(t)$ MDM2 protein	$z_1(t)$ p21 mRNA
$z_2(t)$ p21 protein	$w(t)$ PUMA mRNA	$n(t)$ MYCN protein
u Nutlin-3		

Fitted values with units of concentration in a.u. and time in hours:

$k_{\mathrm{vx1}} = 0.0030211, k_{\mathrm{dx1}} = 0.012513, k_{\mathrm{nx}} = 0.0000027, k_{\mathrm{vx2}} = 0.001367, k_{\mathrm{dxy}} = 0.045035, k_{\mathrm{kx2}} = 2.9075e-06, k_{\mathrm{on}} = 0.0017047, k_{\mathrm{off}} = 0.015316, k_{\mathrm{dx3}} = 0.0021122, k_{\mathrm{vy1}} = 1.8902e-06, k_{\mathrm{vyx}} = 0.0016559, k_{\mathrm{ky1}} = 0.0041499, k_{\mathrm{dy1}} = 0.0085461, k_{\mathrm{ny}} = 0.42642, k_{\mathrm{vy2}} = -4.2553e-08, k_{\mathrm{dy2}} = 0.00062203, k_{\mathrm{vz1}} = 0.00089221, k_{\mathrm{vzx}} = 1.4091e-07, k_{\mathrm{kz1}} = 3.185, k_{\mathrm{kz1n}} = 0.007337, k_{\mathrm{dz1}} = 0.00055685, k_{\mathrm{vz2}} = 0.0044282, k_{\mathrm{dzy}} = 0.48128, k_{\mathrm{kz2}} = 0.23796, k_{\mathrm{dz2}} = 9.0057e-05, k_{\mathrm{n}} = 0.22345, k_{\mathrm{u}} = 21.802, k_{\mathrm{vw}} = 0.0017019, k_{\mathrm{vwx}} = 0.03973, k_{\mathrm{kw}} = 0.029752, k_{\mathrm{dw}} = 0.44152, k_{\mathrm{dx2}} = 0.00030335$

A.7 Input file for XPPaut for the equations of the E2F-pRB module

```
dPE/dT=KE1*P*E-LE1*PE-KR1*PE*R-KR2*PE*RP+LR1*PER+LR2*PERP+A2*C2*PERP
dPA/dT=KP*PII*C2-LP*PA-DP*PA-DP2*S*PA-KC*PA*C2+LC*CPA+DC*CPA
dPII/dT=VP-KP*PII*C2+LP*PA-DP*PII-KC*PII*C2+LC*CPI+DC*CPI
dC2/dT=VC0+VC*PE-DC*C2-KC*(PA+PII)*C2+LC*(CPI+CPA)-kp1*(p21tot-c2p)*C2+lp1*c2p
dc2p/dT=-DC*c2p+kp1*(p21tot-c2p)*C2-lp1*c2p
dCPI/dT=-DC*CPI+KC*PII*C2-LC*CPI-KP*CPI*C2+LP*CPA
dCPA/dT=-DC*CPA+KC*PA*C2-LC*CPA+KP*CPI*C2-LP*CPA
dR/dT=-A1*C4*R+B1*RP+VR-DR*R-KR1*(PE+E)*R+LR1*(PER+ER)
dRP/dT=A1*C4*R-B1*RP-A2*C2*RP+B2*RPP-DR*RP-KR2*(PE+E)*RP+LR2*(PERP+ERP)
dP/dT=-KE1*P*(E+ER)-KE2*P*ERP+LE1*(PE+PER)+LE2*PERP
dPER/dT=KE1*P*ER-LE1*PER+KR1*PE*R-LR1*PER-A1*C4*PER+B1*PERP
dE/dT=VE+VE2*PE-KE1*P*E+LE1*PE-KR1*E*R-KR2*E*RP+LR1*ER+LR2*ERP-DE*E+A2*C2*ERP
dER/dT=KR1*E*R-LR1*ER-KE1*P*ER+LE1*PER-A1*C4*ER+B1*ERP
dERP/dT=KR2*E*RP-LR2*ERP-KE2*P*ERP+LE2*PERP+A1*C4*ER-B1*ERP-A2*C2*ERP
dS/dT=VS*PE+VS0-DS*S
PERP=1-(P+PE+PER)
RPP=10-(R+RP+ER+ERP+PER+PERP)
C4=1/KC4*(c+myc)*serum
param
serum=0.01,myc=0,p21tot=0,VP=1,KP=1,LP=10,DP=0.01,DP2=0.5,KC=1,LC=1,VC0=10,VC=1,DC=1,
A1=1,B1=1,A2=1,B2=0.09,VR=0,DR=0,KE1=1,LE1=0.01,KE2=1,LE2=0.01,KR1=1,KR2=1,LR1=0.025,LR2=0.025,
VE=0.1, VE2=2,DE=4,VS=1,VS0=0.01,DS=0.1,KC4=1,c=1,kp1=1,lp1= 1
init PA=0,PII=0,C2=0,CPI=0,CPA=0,R=10,RP=0,P=1,PE=0,PER=0,E=0,ER=0,ERP=0,c2p=0
@ total=100,dt=.1,xhi=100,METH=qualrk
done
```

Abbreviations

AIC	Akaike information criterion
a.u.	arbitrary units
bHLHZ	basic-helix-loop-helix-zipper
cdf	cumulative distribution function
cDNA	complementary DNA
cyto	cytoplasmic
DAPI	4,6-diamino-2-phenylindol
DTT	dithiothreitol
FACS	fluorescence-activated cell sorting
FCS	fetal calf serum
FRAP	fluorescence recovery after photobleaching
GAS	IFN-gamma-activated sites
GFP	green fluorescent protein
HRP	horse reddish peroxidase
IFN-γ	interferon gamma
LMB	leptomycin B
LSN	mutated NLS
MCMC	Markov chain Monte Carlo
NES	nuclear export sequence
NLS	nuclear localization sequence
wNLS	weak NLS
sNLS	strong NLS
nuc	nuclear
PAA	polyacrylamide
PBS	phosphate buffered saline
PCR	polymerase chain reaction
pdf	probability density function
PEST	rich in proline, glutamic acid, serine, and threonine sequence
phospho	phosphorylated
qRT-PCR	quantitative real-time RT-PCR
R-point	restriction point
RT-PCR	reverse transcription reaction followed by PCR
SAD	steady age distribution
SDS-PAGE	sodiumdodecylsulfat polyacrylamide gel electrophoreses
SH2	src homology 2 domain
siRNA	small interfering RNA
tot	total
unspec.	unspecific
Tyr	tyrosine
WT	wild type

Danksagung

Prof. Dr. Thomas Höfer möchte ich danken, dass er mir die Möglichkeit gegeben hat, in seiner Arbeitsgruppe meine Promotion anzufertigen. Die fruchtbaren wissenschaftlichen Diskussionen, die vielen Hilfestellungen und die tolle Art, mit der er seine Arbeitsgruppe führt, haben mir in den Jahren meiner Promotion den Rücken gestärkt und es mir einfach gemacht, mich wohlzufühlen.

Dafür dass Priv. Doz. Dr. Frank Westermann mich in die Geheimnisse der Neuroblastoma Forschung eingeführt hat, für die herzliche Aufnahme in seine Arbeitsgruppe und für die vielen hilfreichen Diskussionen bedanke ich mich bei ihm.

Priv. Doz. Dr. Karsten Rippe möchte ich an dieser Stelle für die Übernahme des Erstgutachtens danken und Prof. Dr. Ursula Kummer danke ich für die Übernahme des Prüfungsvorsitzes.

Bei Prof. multi. Dr. Thomas Meyer möchte ich mich für die hervorragende Kollaboration, seinen unerschütterlichen Optimismus und die vielen wissenschaftlichen Diskussionen am Telefon bedanken.

Der B030 Truppe möchte ich herzlich danken, dass sie mich so freundlich aufgenommen haben, dass sie mir die Möglichkeit gegeben haben bei ihnen meine Experimente durchzuführen und dass sie mich in ihre Kaffeerunde integriert haben. Für die vielen Hilfestellungen und erbaulichen Gespräche möchte ich Christina, Sina und Steffen danken. Mein besonderer Dank gilt Daniel, mit dem die Zeit im Labor immer mit viel Lachen und lebhaften wissenschaftlichen, sowie nicht-wissenschaftlichen Diskussionen gefüllt war.

Bei der ganzen Höfer Arbeitsgruppe möchte ich mich für ihre Unterstützung und die gemeinsam verbrachte Zeit bedanken. Anna, Erika, Micha und Sandip danke ich sehr für das Korrekturlesen meiner Kapitel. Elena Cristiano möchte ich für ihre gute Masterarbeit, sowie die lustige und belebende Zeit in unserer Gruppe danken. Stephen Krämer danke ich für die großartige Zusammenarbeit und den intesiven Einsatz in seinem Projekt. Ganz besonders möchte ich mich auch bei Anna, unserer guten Seele im Büro, für die schöne Zeit bedanken.

Micha, in dem ich einen tollen Freund gefunden habe, danke ich von Herzen für die zahlreichen Diskussionen und das Teilen von Hochs und Tiefs bei vielen Kaffees und Bieren.

Ganz besonders inniger Dank gilt meiner Familie, die immer zu mir hält und für mich da ist. Er gilt meinen Eltern Birgitt und Gunter, meinen Brüdern Björn und Kevin, meinem Onkel Heiko und meinen Omas Hedwig und Hannelore. Auch besonders möchte ich meinen Schwiegereltern Godwina und Wolfram, sowie Angelika und Heinrich danken, die mich liebevoll in ihre Familie aufgenommen und immer unterstützt haben.

Am allermeisten möchte ich mich bei meiner lieben Janna bedanken, die mit ihrer wundervollen Art, ihrem grenzenlosen Verständniss und ihrer Liebe mein Leben bereichert.